Synthèse et étude structurale de nanozeolites à petits micropores pour la capture du CO2

Maxime Debost

Normandie Université

THÈSE

Pour obtenir le diplôme de doctorat

Spécialité CHIMIE

Préparée au sein de l'Université de Caen Normandie

Synthèse et étude structurale de nanozeolites à petits micropores pour la capture du CO2.

Présentée et soutenue par
Maxime DEBOST

Thèse soutenue publiquement le 18/11/2019 devant le jury composé de		
M. BENOIT LOUIS	Directeur de recherche au CNRS, Université de Strasbourg	Rapporteur du jury
M. PASCAL ROUSSEL	Directeur de recherche au CNRS, ECOLE NATIONALE SUPERIEURE de CHIMIE	Rapporteur du jury
M. JEAN-PIERRE GILSON	Professeur des universités, ENSICAEN	Président du jury
M. NIKOLAI NESTERENKO	Senior scientist, Total Petrochemicals Research Feluy	Membre du jury
Mme SVETLANA MINTOVA	Directeur de recherche au CNRS, Université Caen Normandie	Directeur de thèse
M. PHILIPPE BOULLAY	Directeur de recherche au CNRS, ENSICAEN	Co-directeur de thèse

Thèse dirigée par SVETLANA MINTOVA et PHILIPPE BOULLAY, Laboratoire catalyse et spectrochimie (Caen)

UNIVERSITÉ CAEN NORMANDIE

ED 508 NC Normande de Chimie

LCS Laboratoire Catalyse & Spectrochimie

Normandie Université

THESE

Pour obtenir le diplôme de doctorat

Spécialité Chimie (TH CHIM)

Préparée au sein de l'ENSICAEN et de l'UNICAEN

Synthèse et étude structurale de nanozeolites à petits micropores pour la capture du CO_2

Présentée et soutenue par

Maxime DEBOST

Thèse soutenance publiquement le 18/11/2019 Devant le jury composé de		
M. Benoît LOUIS	Directeur de recherche CNRS, ICPEES Strasbourg, FR	Rapporteur
M. Pascal ROUSSEL	Directeur de recherche CNRS, UCCS Lille, FR	Rapporteur
M. Jean-Pierre GILSON	Professeur, LCS, ENSICAEN Caen, FR	Examinateur
M. Nikolai NESTERENKO	Manager développement / Total TRTF, BE	Examinateur
Mme. Svetlana MINTOVA	Directrice de recherche CNRS, Université de Caen-Normandie, LCS, FR	Directeur de thèse
M. Philippe BOULLAY	Directeur de recherche CNRS, Université de Caen-Normandie, CRISMAT, FR	Co-directeur de thèse

Thèse co-dirigée par Svetlana MINTOVA et Philippe BOULLAY, laboratoire Catalyse et Spectrochimie (LCS) et laboratoire de cristallographie et sciences des matériaux (CRISMAT)

“Imagination is more important than knowledge. For knowledge is limited, whereas imagination embraces the entire world, stimulating progress, giving birth to evolution”

Albert Einstein

Remerciements

Cette partie est dédiée à toutes les personnes qui ont participées d'une façon ou d'une autre à rendre cette aventure possible.

Cette thèse a été réalisée au Laboratoire de Spectrochimie et Catalyse (LCS) et au Laboratoire de Cristallographie et Sciences des Matériaux (CRISMAT) de Caen dirigés respectivement par les directeurs de recherche Christian Fernandez et Wilfrid Prellier que je souhaite remercier pour leur accueil.

Ensuite, je tiens à remercier tout particulièrement mes deux encadrants de thèse, Philippe et Svetlana, qui m'ont guidé et beaucoup appris pendant ces 3 années. Philippe, tes explications et tes remarques n'ont fait que me pousser à m'améliorer. J'ai pu compter sur toi à tout moment et tu t'es montré disponible dès que j'ai eu besoin de toi. Ta passion pour la microscopie et le travail bien fait a été particulièrement inspirant. Svetlana, merci d'avoir fait de moi un meilleur scientifique et m'avoir monté comment mieux réfléchir, d'avoir partagé ton savoir. Ton enthousiasme face à mes idées et ton esprit d'innovation ont été profondément inspirantes. Merci à vous deux de m'avoir offert les opportunités de communiquer sur mon travail à travers le monde.

Je voudrais adresser toute ma gratitude à Nicolas Barrier, sans qui mes résultats n'auraient pas eu la même saveur. Merci pour tes enseignements et ta bonne humeur. Je remercie également Valentin Valtech, Delphine Minoux et Cindy Aquino pour la qualité exceptionnelle de leurs remarques scientifiques.

Je suis sincèrement reconnaissant envers les membres de mon jury Louis Benoît, Pascal Roussel, Jean-Pierre Gilson, Nikolay Nesterenko, pour avoir accepté de lire, commenter et d'évaluer et mon travail.

Les premières personnes que je me dois de remercier pour leur amitié pendant toutes ces années sont Julien, Kamila, Luz, Eddy, Stas. Les souvenirs que je garde des moments passés en votre compagnie resteront pour moi les meilleurs moments de mon doctorat. Je ne peux pas oublier de remercier les personnes qui ont rendu les semaines de travail plus belles: Peng, Patryk, Elizabeth, Sandra, Stijn, Dusan, Clément A., Viktoria, Kristoffer, Top, Guillaume.

Je pense fort à mes amis Florent, Léa, clémentine et Marion, Vincent, Chloé et surtout Antoine. Un clin d'œil tout particulier à ceux que l'on ne peut pas stopper ;)

Mercie aux équipes du laboratoire qui nous aide au quotidien: Pascal, Yoann, Marie, Benjamin, Philippe, Sophie, Blandine, Valérie, Florent and Nathalie.

Je tiens à remercier mes parents et ma famille pour m'avoir conseillé et m'avoir soutenu. A tous ceux qui était là dès le début de mon voyage et à ceux que j'ai rencontrés en cour de route mais que j'aime tout autant, merci pour votre amour et les belles valeurs que vous m'avez transmissent, je ne serais pas l'homme accompli que je suis sans vous !

Et finalement, Josepha, mon amour, mon amie, mon soutien, mon infirmière, ma chérie, qui a montré une patience infinie et qui a toujours été là pour moi. Notre gestion de cette période a encore montré que l'on peut survoler toutes les épreuves. Je t'aime !

TABLE DES MATIÈRES

LISTE DES ABREVIATIONS

1D	One-dimensional
2D	Two-dimensional
3D	Three dimensional
BPH	Beryllophosphate-H
CHA	Chabazite
CH_4	Methane
CO_2	Carbone Dioxide
ED	Electron Diffraction
EDI	Edingtonite
EDS	Energy dispersive spectroscopy
EMT	Elf Mulhouse Two
FAU	Faujazite
FTIR	Fourier Transform Infra-Red
FWHM	Full width half maximum
HRTEM	High resolution transmission electron microscopy
ICP	Inductively coupled plasma
IZA	international zeolite association
LSX	Low silica X zeolite
LTA	Linde Type A
MOF	Metal-organic framework
MTM	Methane to Methanol
MTO	Methanol to Olephins
N_2	Nitrogen
OSDA	Organic structure directing agent
PEDT	precession electron diffraction tomography
PXRD	Powder X-ray diffraction
SCR	Selective catalytic reduction
SEM	Scanning Electron Microscope
Silicate-1	Pure silica MFI-type zeolite
SSZ-13	Synthesized by Stacey Zones n°13
TEM	Transmission Electron Microscope
TEAOH	Tetraethylammonium hydroxide
TMAOH	Tetramethylammonium hydroxide
TMAdaOH	Tetramethyladamantylammonium hydroxide
USB	Unit Secondary Building
USY	Ultra stable Y zeolite

AVANT-PROPOS

Le dioxyde de carbone (CO_2) est un gaz à effet de serre présent comme produit de combustion principal des combustibles fossiles, ainsi que comme composant du gaz naturel, du biogaz et des gaz de décharge. Outre les considérations environnementales, il existe un intérêt économique à retirer le CO_2 de ces flux de gaz pour obtenir un carburant à haute teneur énergétique et prévenir les problèmes de corrosion dans le système de transport de gaz. Pour répondre à cette problématique, notre contribution consiste à synthétiser des matériaux microporeux offrant cette possibilité de capter de façon sélective le CO_2 présent dans un mélange de gaz. Pour ce travail, les matériaux de type zéolithes apparaissent de bons candidats au vu des travaux déjà disponibles dans la littérature. L'originalité sera ici de trouver les conditions permettant d'obtenir des zéolithes de taille nanométrique par une synthèse directe à la fois respectueuse de l'environnement et nécessitant de faibles coûts de mise en œuvre. Plusieurs stratégies ont été mise au point pour proposer des matériaux avec des capacités d'adsorption du CO_2 de plus en plus efficace tout en restant sélectifs.

La première partie de ce manuscrit (chapitre 1) présente le contexte de l'étude en s'intéressant notamment à la description des zéolithes et des tamis moléculaires, à l'intérêt porté à la séparation de gaz et aux objectifs chiffrés du projet. Les approches et outils scientifiques utilisés pour mener à bien ce travail seront introduits à la suite de cet état de l'art (chapitre 2).

La deuxième partie présentera les principaux résultats obtenus lors de ces trois années de thèse. Un volet important implique la synthèse directe de zéolithes à petits pores telles que la CHA et la RHO en l'absence non seulement d'agents structurants organiques (OSDA) mais également de germes ou de recristallisation à partir d'autres zéolithes. Les différentes synthèses et premières caractérisations permettant d'obtenir un composé présentant toutes les caractéristiques désirées sont détaillées pour le cas de la CHA (chapitre 3). L'étude de la structure et de l'adsorption de CO_2 par la CHA sera quant à elle traitée dans le chapitre 4. Le chapitre 5 abordera la synthèse, l'étude structurale et les résultats des tests d'adsorption sélective du CO_2 pour la zéolithe RHO. La présentation de ces résultats sera effectuée de façon synthétique suivant une mise en forme en relation avec soit des brevets en cours de dépôt (chapitre 3), soit des articles en cours de rédaction (chapitres 4 et 5).

Les résultats des recherches menées dans le cadre de cette thèse ont permis d'obtenir des matériaux présentant de bonnes caractéristiques physico-chimiques pour des applications

potentielles dans la capture sélective du CO_2. Les principales caractéristiques des zéolithes CHA et RHO synthétisées lors de ce travail et leur comportement vis-à-vis de l'absorption de CO_2 seront résumés. Des résultats annexes seront brièvement mentionnés dans le but d'ouvrir des perspectives quant à la suite à donner à ce travail.

CHAPITRE 1: INTRODUCTION

I. L'adsorption de CO_2

A. Emissions de CO_2 et gaz à effet de serre

De nos jours, la recherche de sources d'énergie renouvelables et de matières premières pour les produits chimiques visant la réduction des émissions de gaz à effet de serre est un enjeu sociétal. Le gaz naturel est largement considéré comme un carburant alternatif aux autres hydrocarbures et source carboné puisqu'il produit moins de CO_2 généré par W.h produit. Le biogaz comme source d'énergie renouvelable polyvalente, peut être considéré comme une énergie durable et remplacer le gaz naturel. Le biogaz peut être produit à partir de substances organiques tels que le fumier, les boues d'épuration et les déchets organiques[1].

La composition du biogaz brut varie d'une source à l'autre, mais les principaux composants sont le méthane et le dioxyde de carbone. Le dioxyde de carbone est aussi une impureté commune dans le gaz naturel (Tableau 1)[1,2]. Le dioxyde de carbone doit être retiré du biogaz ou du gaz naturel car il abaisse la valeur calorifique du gaz et il peut également causer de la corrosion dans les tuyaux[3]. De plus, le transport de gaz est rentable pour les industriels lorsque le gaz est pur. Plus généralement, le méthane est une molécule particulièrement intéressante puisqu'elle est une matière première dans l'industrie pétrochimique.

Tableau 1 : Composition (en mol%) typique du gaz naturel et du biogaz transporté dans les pipelines.

Composant	Méthane	C_2-C_4	CO_2	N_2	H_2O	H_2S	C_5 et plus
Gaz naturel	88	9	1.6	0.2	0.1	0	Résidus
Biogaz	65	-	35	0.2	0.1	0-0.4	-

Le gaz naturel est un hydrocarbure polyvalent et son utilisation croissante est liée aux avantages écologiques[4] qu'il propose par rapport aux autres matières premières fossiles. Le gaz naturel représente 22% de l'énergie mondial et il produit près du quart de la production d'électricité, faisant de la ressource un enjeu crucial.

B. Techniques de capture de CO_2 par sorption

Ici, nous évoquerons les méthodes industrielles existantes permettant de séparer le CO_2 du CH_4. Des études approfondies ont été menées pour développer des techniques rentables de captage et de séparation du CO_2[5]. Parmi les technologies de captage du CO_2, l'absorption des solvants, l'adsorption solide, la séparation par membrane et la distillation cryogénique sont les technologies les plus efficaces actuellement. On note que la plupart de ces méthodes sont basées sur les phénomènes « d'adsorption ». Tout type de processus à base de sorption (adsorption ou absorption) nécessite un "sorbant" et un "sorbate". Le sorbant est l'objet qui sert d'hôte au sorbate.

1. Epuration cryogénique

La technique de séparation cryogénique met à profit les différents points d'ébullition des composés gazeux du biogaz: le CO_2 a son point d'ébullition à -78°C à pression atmosphérique alors que celui du méthane se situe à -160°C à conditions équivalentes. La technique consiste donc à refroidir progressivement du gaz brut sous pression. Chacun des constituants se condensera en une phase liquide à différents températures et pourront ainsi être séparés.[6]

Le problème de la méthode vient du coût considérable en énergie mais également de la nécessité d'ajouter une étape de prétraitement pour retirer l'eau, le N_2 et le H_2S. Si l'azote doit être également retiré, le biogaz peut être refroidi d'autant, le point d'ébullition du N_2 étant –195 °C. Cette technique est particulièrement adaptée aux gaz de décharge car elle traite efficacement les siloxanes et l'azote.

2. Absorptions chimiques utilisant des amines aqueuses

Un solvant possédant des affinités physicochimique avec le CO_2 est utilisé pour absorber le gaz (Alcanolamines : MEA, DEA, MDEA …).

La MEA est l'amine aqueuse utilisée traditionnellement pour des raisons économique et d'efficacité. Néanmoins, le procédé d'absorption à la MEA présente un certain nombre d'inconvénients : la dégradation de la MEA et les pertes de solvant. La MEA peut se dégrader rapidement si la température dans le désorbeur excède 130 °C, c'est pourquoi la température y est maintenue à environ 120 °C. Par ailleurs, un certain nombre de composés contenus dans les fumées tels que l'oxygène, les NOx et les SOx peuvent réagir avec la

MEA et former des « sels stables en température ». Il est nécessaire d'apporter du solvant « neuf » au procédé pour compenser les pertes par dégradation.

3. Séparation par utilisation de membranes

Le procédé membranaire est basé sur la diffusion sélective d'un ou plusieurs gaz à travers une membrane composé d'un adsorbant et d'une matrice. Ici, la séparation du CO_2 du méthane est due à la différence de perméabilité des membranes de chaque composé du mélange. Chaque molécule diffusera différemment dans les pores des absorbants constituants la membrane. Ainsi, la force motrice de la séparation membranaire provient de la différence de pressions partielles des composants entre les deux côtés de la membrane. Il faut donc appliquer une compression du mélange gazeux afin de fournir la différence de pression. Par exemple, le dioxyde de carbone peut traverser plus vite la membrane que le méthane, ainsi la concentration de CO_2 sera plus importante d'un côté de la membrane que de l'autre. Ce procédé est particulièrement bien adapté aux purifications post-combustion et permet d'augmenter la pureté d'un gaz.

4. Procédés basés sur les phénomènes d'adsorption

Basé sur le mode choisi pour régénérer l'adsorbant, la capture de gaz peut être effectué par les procédés d'adsorption par variation de température (TSA) ou par variation de pression / vide (PSA / VSA).

PSA

Dans les procédés PSA, le gaz cible est capturé à des pressions élevées puis l'adsorbant est régénéré par une diminution de pression. L'adsorption modulée par le vide (VSA) est similaire au PSA, dans laquelle la régénération est effectuée à des pressions réduites et l'adsorption se produit à des pressions proches de la pression atmosphérique. Les procédés de variation de pression ou de vide ont l'avantage, sur le procédé TSA, d'avoir une phase de recyclage plus rapide (quelques minutes voir secondes) en lits fixes.

TSA

L'absorption par variation de température implique que le gaz absorbé doit réagir fortement aux changements de température et spécialement dans la tranche de 300 à 423 K. Ainsi, les absorbants de type chimisorbants avec des chaleurs d'adsorption comprises entre 40 et 70 kJ/mol de CO_2 conviennent bien. Le plus gros inconvénient des cycles d'adsorption dit « thermo-swing » est le temps de cycle importants nécessaire à la désorption de l'adsorbat

(de l'ordre de plusieurs heures). Cela restreint les systèmes TSA aux applications à petite échelle.

C. Les caractéristiques des adsorbants

Il est important d'identifier les caractéristiques des adsorbants que l'on cherche à utiliser. Le type d'adsorbant employé dépend grandement des conditions d'utilisation imposé par le procédé: sera-t-il utilisé dans des procédés TSA, VSA, PSA ou membranaire ? Travaille–t-on en phase gaz ou liquide ? Quel est la sélectivité du matériau ? Quel est la quantité de matière qu'il peut contenir ? Ainsi, lors du choix d'un adsorbant, tous ces aspects doivent être pris en compte.

Capacité d'adsorption de CO_2

Lorsque l'on parle d'adsorption de CO_2, l'adsorbant agit comme un piège pour le CO_2. La capacité d'adsorption est donc extrêmement importante, puisque l'adsorbant devra être régénéré moins fréquemment. Les adsorbants réduisent le coût de la capture de CO_2. Une faible adsorption peut être envisagée uniquement si le matériau est exceptionnellement sélectif et peut servir à retirer les derniers ppm de CO_2 en fin de processus.

Il est important de distinguer la capacité de travail de la capacité maximal (ou saturation). En effet, la «capacité de travail» du matériau correspond aux capacités d'adsorber et de désorber dans les conditions d'utilisation exactes du processus.

Par exemple, dans beaucoup de procédés, le gaz est comprimé jusqu'à plusieurs dizaines de bars avant d'atteindre l'étape de séparation. L'adsorbant doit adsorber le CO_2 à ces pressions élevées et se désorber par diminution de pression (PSA). Dans ce cas, la capacité maximale de CO_2 de l'adsorbant n'est pas importante, mais plutôt la différence de la capacité d'absorption entre les deux pressions appliquées.

Sélectivité

Le second paramètre important est la sélectivité. Un matériau qui absorbe sans distinction tous les gaz, ne présentent pas d'intérêt pour des applications industrielles.

Comme décrit précédemment, les sources de gaz naturel ou biogaz contiennent presque toujours la présence d'autres gaz. L'adsorption de ces autres gaz (N_2, CH_4, H_2O, H_2S) compromettra l'absorption de CO_2, il faut donc trouver les matériaux les plus discriminants possible et travailler dans les conditions les plus sélectives possible (pression, température, post traitement du gaz, propriétés texturales matériau …).

Régénération

La troisième règle à retenir est la capacité cyclique d'un adsorbant c'est-à-dire la capacité du matériau à résister aux processus d'adsorption / désorption. Idéalement, la capacité en CO_2 de l'adsorbant devrait rester la même tout au long de sa vie. Si l'adsorbant n'est pas parfaitement stable dans les conditions de fonctionnement, il risque de perdre de sa capacité en CO_2 après plusieurs cycles.

La force d'interaction qui s'est créé pendant l'absorption du CO_2 doit être la plus faible possible pour que la régénérabilité de l'adsorbant se fasse en utilisant le moins d'énergie possible et rendre le procédé encore plus viable économiquement.

Coût du matériau

Comme pour tous les procédés industriels le coût est un critère primordial. Dans l'élaboration du coût associés aux processus PSA et VSA pour l'absorption du CO_2,[7] l'absorbant occupe une place importante. Dès lors, les zéolithes et le charbon actif se détachent nettement comparés au MOF malgré leurs caractéristiques bien supérieures en termes de surface spécifique et de sélectivité.

La prochaine section examine la littérature publiée sur les zéolithes cristallines sous forme d'adsorbants de CO_2[8,9] et spécialement les zéolithes à petits pores[10]. Au préalable, nous allons traiter de l'état de l'art autour des méthodes de synthèse de ces matériaux et leur application à la séparation de gaz.

II. Etat de l'art : Zéolithes à petit micropores

A. Les zéolithes

Les zéolithes sont des aluminosilicates cristallins microporeux ayant une structure tridimensionnelle constituée de tétraèdres [SiO_4] liés les uns aux autres par un atome d'oxygène. La substitution d'atomes de Si^{4+} par des atomes d'Al^{3+} crée une charge négative. Cette charge sera contrebalancée par un cation extra-réseau qui donne aux zéolithes les caractéristiques d'échangeur ionique. Aujourd'hui, plus de 240 topologies de structures zéolithiques différentes ont été approuvées par la commission de structure de l'Association Internationale de Zéolithes (IZA). La structure est identifiée par un code à trois lettres quelle que soit sa composition chimique. La structure finale des zéolithes est constituée d'un assemblage d'unités de structures primaires, pouvant également former des unités de

structures secondaires (ex : cubes, pavés, octaèdres etc.). La microporosité structurelle régulière et ordonnée de ces matériaux leurs confère des propriétés intéressantes et uniques dans le domaine des matériaux poreux. La définition de «zéolithe» a évolué depuis la dernière décennie, incluant également des compositions sans aluminosilicate, préalablement appelés zeotypes, où la structure est formée par des tétraèdres TO_4 avec T = P, Ga, B, etc.

B. Les catégories de zéolithes

Les structures formées par les tétraèdres TO_4 s'additionnent pour former des unités de structures secondaires (USS ou SBU en anglais). Les unités formant des cycles sont notés en fonction du nombre de tétraèdres suivie des lettres MR pour « n-membered ring » (exemples : 6 atomes est noté 6MR, 8 atomes est noté 8MR).

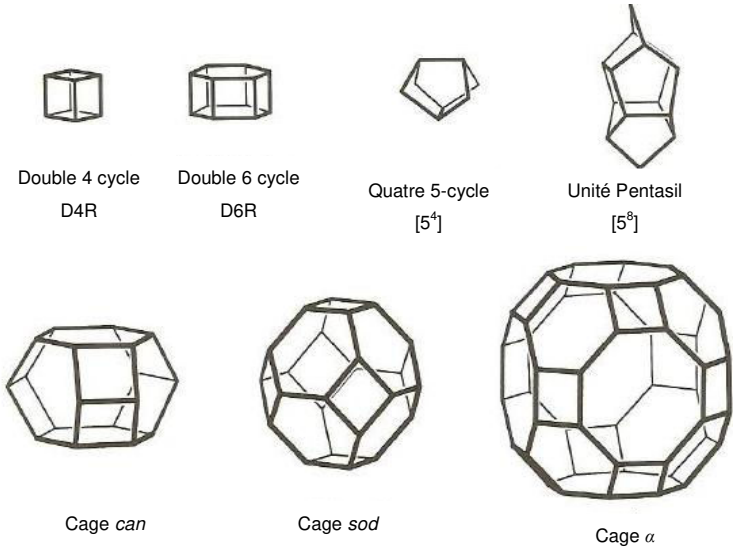

Figure 1: Exemples d'unités de structures secondaires (USS) formant des structures zéolithiques. Ces représentations mettent en évidence les liaisons T-T présentes dans les USS.

De même, l'on ajoute la lettre D pour « double » lorsque deux anneaux se superposent (exemples : double-6-cycles s'écrit D6R). La Figure 1 montre l'assemblage des cages comme unité de structure tel que la cage « *sod* » à ne pas confondre avec la zéolithe du même nom.

La structure cristalline poreuse des zéolithes et zeotypes (ex : silico-aluminophosphates) les plus utilisées dans l'industrie, sont présentées Figure 2. La notation des zéolithes, la description des cages et canaux de leur structure poreuse ainsi que leurs principales applications industrielles y sont également mentionnées.

Les zéolithes se divisent en 3 catégories définies par le nombre d'atomes : les zéolithes à petit pores (moins de 4.5 Å de diamètre), les zéolithes à pores intermédiaires (4.5-7 Å de diamètre) et les zéolithes à larges pores (plus de 7 Å de diamètre).

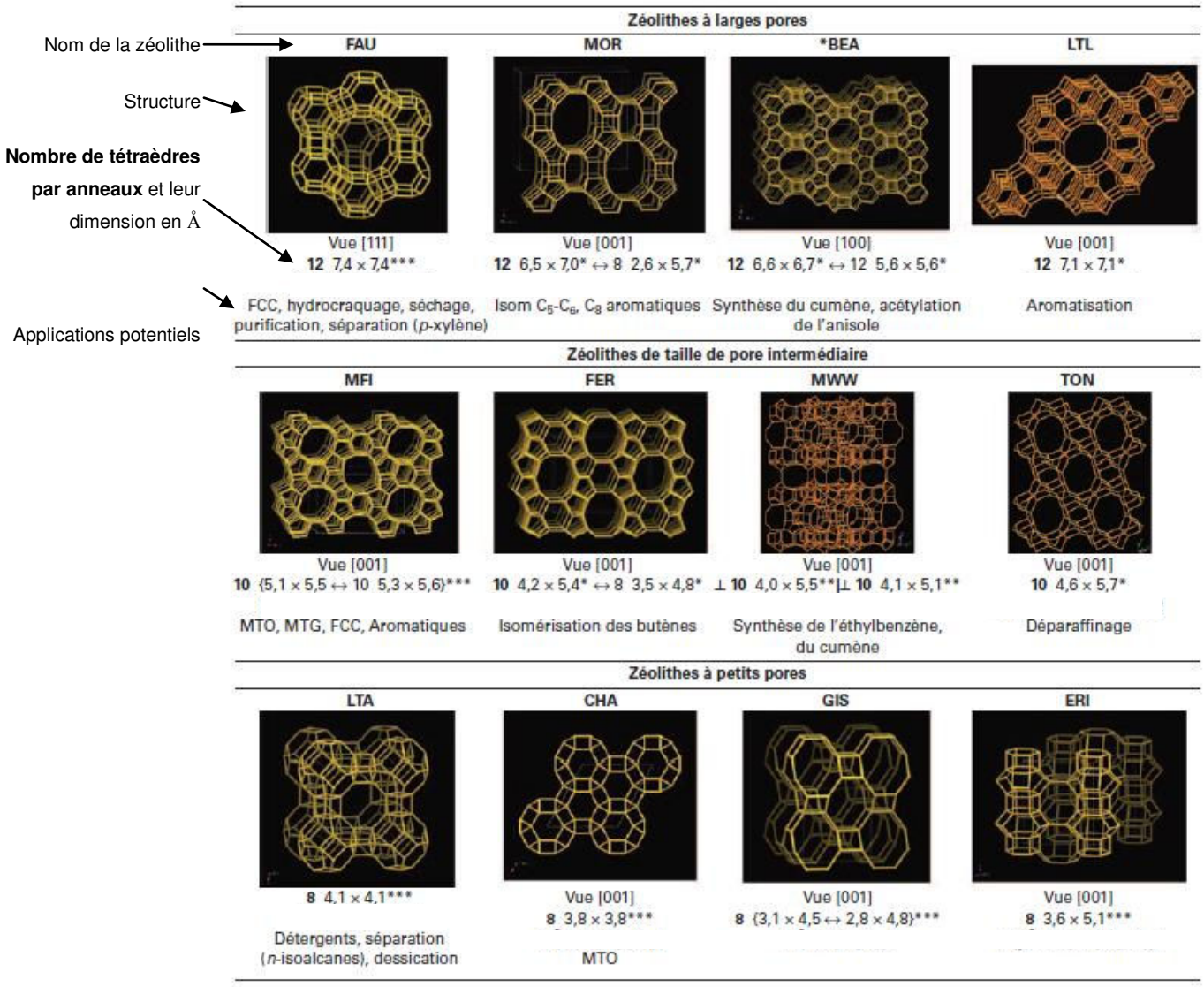

Figure 2: Structure poreuse des 3 familles de zéolithes et un exemple d'application industrielle[11].

Malgré la grande variété de structures, seulement quelques-unes ont un intérêt industriel et sont produites à grande échelle : AEL, AFY, ***BEA, CHA**, EDI**, FAU, FER**, GIS, **LTA**, LTL, MER, **MFI, MOR**, MTT, MWW, TON, et RHO[12].

C. Les zéolithes synthétiques

Les zéolithes synthétiques ont joué un rôle important dans le traitement de ressources fossiles ou renouvelables[13,14] . Ces matériaux ont révolutionnés les domaines de la catalyse et la séparation de gaz grâce à leurs sites actifs situés à l'intérieur d'un réseau de

micropores, présentant des activités élevées et une sélectivité exceptionnelle. Le succès des zéolithes en catalyse provient du fait que leurs cages et canaux peuvent être considérés comme des nanoréacteurs induisant une sélectivité des produits transformés déterminée par les sites actifs mais également par l'effet de confinement (sélectivité de forme).

Au début des années 1960, leur introduction a conduit à des innovations dans le raffinage du pétrole avec des réactions chimiques tel que le craquage catalytique (FCC) ou l'hydrocraquage. Parmi les procédés de séparation de molécules, on peut citer le traitement des aromatiques (ex: p-xylènes)[13] ou la séparation de gaz (ex: CH_4/CO_2).

En règle générale, les zéolithes sont synthétisées par cristallisation hydrothermale d'un mélange amorphe contenant une source de silice, un agent structurant organique (appelé OSDA pour « organic structure directing agent » aussi appelé « template ») et optionnellement, un agent minéralisant et une source d'aluminium. On peut résumer les étapes de synthèse des zéolithes par:

1) Le mélange des réactifs (Si, OSDA, Al…).

2) L'homogénéisation par forte agitation mécanique et addition d'une étape de mûrissement (début de la nucléation) (Figure 3a).

3) La synthèse hydrothermale: début du chauffage de la solution dans une bouteille PPE ou une autoclave.

4) La synthèse hydrothermale: formation des premiers cristaux de zéolithe (Figure 3b).

5) La synthèse hydrothermale: la croissance cristallines de zéolithes (Figure 3b).

6) La filtration et rinçage de la zéolithe.

7) La calcination pour éliminer les éventuels agents structurants organiques (OSDA).

En catalyse, l'un des inconvénients majeur des zéolithes provient de la limitation diffusionnelle dans les canaux des zéolithes, empêchant ainsi la pleine utilisation de leur potentiel[15]. La diminution de la taille des cristaux jusqu'à des dimensions nanométriques réduit considérablement le problème de résistance au transport. En séparation de gaz et notamment CO_2/CH_4, la taille des cristaux change les performances des matériaux sur un aspect : la cinétique d'ab/désorption. En effet, il faut distinguer les phénomènes de diffusion interne, externe et l'adsorption sur les sites actifs. Dans le phénomène de diffusion externe, la surface (lié à la taille de particules) entre en compte dans l'équation de diffusion externe.

D. La synthèses de zéolithes nanométriques

Jusqu'à présent, parmi les 240 structures de zéolithes/zeotypes qui ont été découvertes, seulement 18 d'entre elles ont été synthétisées sous forme de cristaux de taille nanométrique (ABW, *BEA, EDI, EMT, FAU, GIS, LTA, LTJ, LTL, MEL, MER, MFI, MOR, SOD, AEI, AFI, AFO, CHA)[16].

Plusieurs variables doivent être contrôlées lors de la synthèse de la zéolithe. L'un des plus importants étant le rapport Si / Al du gel, suivi des sources des composés choisis, des cations métalliques, des quantités de OSDA et d'eau. Ces deux derniers paramètres jouent un rôle essentiel sur la morphologie et la taille des particules obtenues. Quelques paramètres insoupçonnables tels que l'ordre de mélange, la vitesse d'agitation, la température du gel amorphe, la durée du vieillissement, sont des points cruciaux à garder à l'esprit pour obtenir une zéolithe de taille nanométrique.

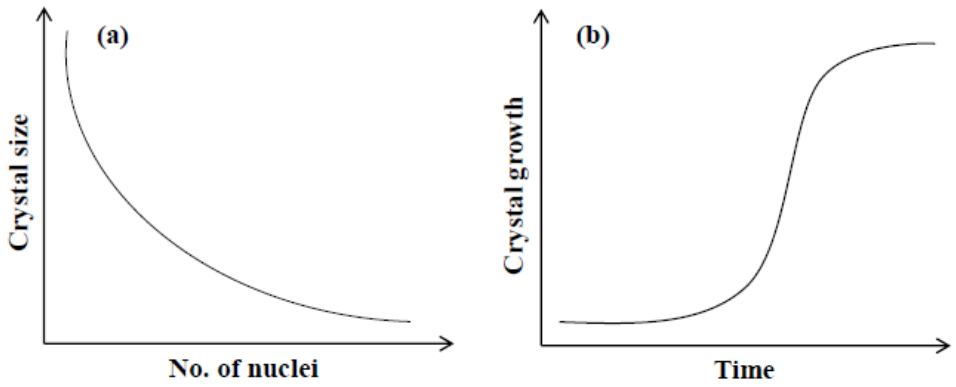

Figure 3: (a) Corrélation entre le nombre de nuclei et la taille des cristaux. (b) Courbe de cristallisation en fonction du temps de synthèse[17].

La synthèse de nanozéolithes est toujours exécutée dans le système fermé. La réaction entre les composants du gel initial conduit à la nucléation des particules et à la croissance des cristaux. La nucléation et la croissance cristalline sont deux processus très complexes, qui peuvent se produire simultanément. Par conséquent, la corrélation entre ces deux phénomènes est cruciale pour la conception de la taille du cristal. La Figure 3a montre que l'augmentation du nombre de nucléus viables entraîne la formation de plus petits cristaux. La manière dont la croissance des cristaux de zéolithe est décrite est généralement basée sur la courbe de cristallisation classique en fonction du temps de traitement hydrothermal (Figure 3b). Par conséquent, afin d'obtenir des cristaux plus petits, les conditions de synthèse doivent être ajustées de manière à favoriser la nucléation par rapport à la croissance cristalline. Un exemple de paramètre modifiable est le rapport température / temps de

synthèse qui doit être le plus bas possible. Le contrôle de l'homogénéité du précurseur initial ainsi que de l'uniformité du processus de nucléation est crucial pour synthétiser des cristaux de zéolithe de taille réduite et homogène.

La réduction de la gamme de température et la forte alcalinité de la méthode de synthèse conduisent à la réduction des tailles de cristaux jusqu'à des dimensions inferieur à 10 nm. Le nombre de zéolithes synthétisées avec ces dimensions est très restreint, mais elles ont presque toutes été obtenues par une voie qui favorise considérablement la formation de ces nanocristaux : la voie de synthèse sans agent structurant organique (OSDA).

E. La synthèse de zéolithes sans agents structurants organiques

Dans la littérature, les méthodes de synthèse par « assistance par germe » et par « transformation par recristallisation » se cachent souvent sous la notion « template-free » ou « synthesis without OSDA ». Dans cette partie, nous marquerons la différence entre les synthèses par assistance (recristallisations ou germes) et les synthèses directes où les précurseurs sont une source de silice, une source d'aluminium et des hydroxydes alcalins (NaOH, KOH, RbOH …). Nous ferons cette distinction puisque la synthèse par assistance de germes, même si très efficace et offrant de plus grande variété de zéolithes, nécessite l'utilisation d'une zéolithe (ou un aluminosilicate) synthétisée avec des OSDA (exemple : La SSZ-13 est d'abord synthétisé puis utilisée comme germe pour la synthèse de CHA)[18].

1. Assistance par germes

Ces dernières années, la synthèse par assistance par germes (« seed assistance » en anglais) s'est révélée être une excellente stratégie pour synthétiser des zéolithes telle que a Silicate-1 (MFI)[19], CHA[18], MAZ[20], MOR[21,22], RUB-37 (CDO), ZSM-11 (MEL), ECR-18 (PAU)[22], ZSM-12 (MTW)[22], RUB-50 (LEV), OFF[23] et BEA[24,25]. Les nucléides de zéolithe qui sont ajoutés dans les gels d'aluminosilicate de départ par la voie sans OSDA proviennent principalement de cristaux de zéolithe sous forme de germes. Cette stratégie évite complètement la combustion d'OSDA coûteux ainsi que la production de gaz nocifs. Elle est donc respectueuse de l'environnement et permet des économies d'énergie. Néanmoins, la synthèse par assistance de germe n'est pas directe: beaucoup de stratégies nécessitent une étape de synthèse avec OSDA, spécialement pour la synthèse de CHA.

2. Transformation par recristallisation de zéolithe

De même, la transformation par recristallisation de zéolithes offre de plus grandes opportunités et ouvre la gamme des zéolithes disponibles. Mais comme pour la synthèse par assistance de germes, le processus n'est pas globalement sans OSDA. Le matériau de base nécessite souvent d'être synthétisé ex-situ avec des OSDA (ex : FAU est synthétisée en présence de TMAOH, puis recristallisé en CHA avec KOH).

3. Sans agent structurant organique et sans assistance

En 2012, Ng et al.[26] ont publié la méthode de synthèse de zéolithe de type EMT dans des conditions douces (36 h à 30 °C), mais en utilisant Na^+ comme agent structurant inorganique dans les proportions molaires suivantes : 11 NaOH: 70 H_2O (avec SAR (liq) = 2,5)[27]. Le réseau poreux formé par les unités de structures secondaires *sod* and *d6R* sont interconnectés en 3 dimensions formant une porosité 3D. Mintova et ses collaborateurs sont parvenus à faire cristalliser la zéolithe EMT dans des milieux non organiques à basse température. L'augmentation de la température avec un temps de synthèse mal raisonné peut conduire à la formation d'impureté telle que SOD. En effet, à 65°C, 2h de traitement supplémentaires transforment l'EMT en SOD qui est plus dense, et donc plus stable. Il a été montré que parmi, les conditions considérées, à savoir la basse température et la teneur en eau, c'est la quantité d'eau qui est la plus cruciale pour la formation d'EMT.

La zéolithe FAU avec une forte quantité d'Al peut être formée dans des conditions similaires[28]. La nouveauté de la stratégie de synthèse employée tient dans le fait que les cristaux sont obtenus avec une taille nanométrique. Les nanocristaux sont utilisés dans des domaines aussi divers que la catalyse[29], la capture de polluants, l'assainissement de l'environnement et surtout la médecine sous forme d'antibactérien ou vecteur de gaz[30].

Maldonado et collaborateurs[31] ont prêtés particulièrement attention à la synthèse de zéolithes en condition alcaline avec du Na^+. Ils ont identifié les étapes multiples de formation des zéolithes obtenues telles que FAU, LTA, EMT, GIS, SOD, ANA, CAN, and JBW. Inspirer des travaux des pionniers Breck et Flanigen, ils ont formulé des tendances empiriques en utilisant des diagrammes ternaires SiO_2-Al_2O_3-Na_2O. A notre connaissance, il s'agit de la première analyse quantitative de tels diagrammes pour la synthèse de zéolithes. Cette étude est particulièrement intéressante pour identifier les paramètres permettant d'adapter la composition cristalline finale (Si/Al, taille de cristaux …) sans renier la pureté de la phase. Ils ont étudié l'impact de six paramètres: trois compositions (Si − Al – Na et leurs fractions molaires), la teneur en eau, la température et le temps. D'après leurs conclusions, les

transformations de la phase zéolithe sont conformes à la règle d'étapes d'Ostwald: ces zéolithes au sodium peuvent subir jusqu'à trois voir quatre transformations de phases distinctes. La règle d'Ostwald-Lussac[32] stipule que le premier cristal à se former est formé d'une structure métastable qui subit une série de transformations intercristallines constituée de structures plus stables thermodynamiquement.

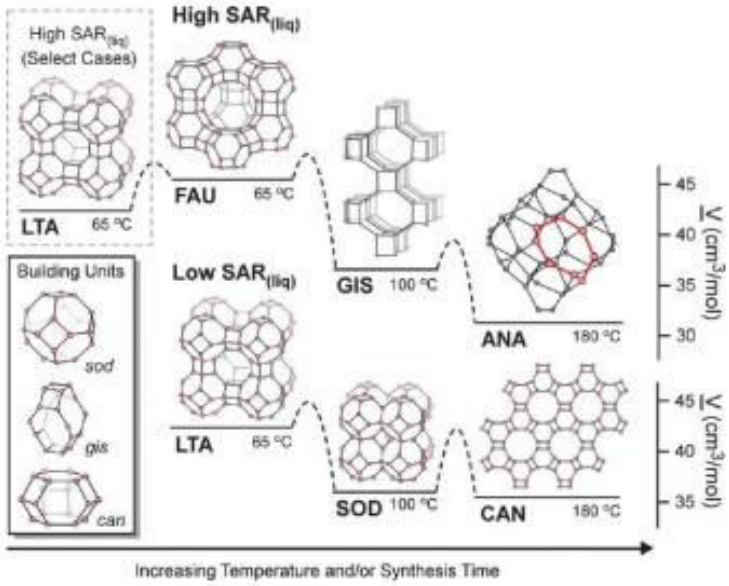

Figure 4: Étapes de la transformation de la phase zéolithique Na avec une température et un temps de synthèse croissants. L'enthalpie relative de formation, ΔHf - ΔHo, pour les structures de zéolithe est supposée être proportionnelle à son volume molaire, V. (copié de Navrotsky et collaborateurs [32])

Les transformations intercristallines dans la synthèse de zéolithes sont couramment observées dans les solutions de croissance sans agent structurant organiques (OSDA) où les métaux alcalins sont utilisés comme agents structurant inorganiques. La Figure 4, montre un exemple ou la règle d'Ostwald s'applique pour les zéolithes synthétisées en présence de Na^+ impliquant la transition entre la Faujasite (FAU), la Gismondine (SIG) puis l'Analcine (ANA) avec une température de synthèse croissante. Bien que les zéolithes FAU, EMT, LTA, SOD ont une structure constituées d'une unité de structure secondaire (USS) commune, la cage *sod*, les zéolithes FAU, CAN, GIS et ANA ont des unités de structure secondaire (USS) très différentes. Une explication possible de ces transformation peut venir d'une relation d'épitaxie entre les structures zéolithiques dans laquelle l'interface cristalline de la zéolithe formée se nucléera préférentiellement en surface de la zéolithe préexistante.

Il existe d'autres zéolithes synthétisées sans OSDA utilisant Li^+, Na^+, K^+, Rb^+ ou Cs^+ comme agent structurant. La plupart d'entre elles sont présentées dans la revue publié en 2014 par Oleksiak and Rimer[33]. Ils y résument les conditions de synthèse de plusieurs centaines de

références de synthèses de zéolithes sans OSDA. Des mélanges de cations ont été proposés également pour former les zéolithes LTL[34], FER[35], LTT (ERI/OFF) ou RHO.[36,37]

Parmi ces synthèses, on peut faire la liste des expériences ayant mené à des zéolithes nanométriques en absence d'un agent structurant organique. Le Tableau 2 liste les conditions de synthèses de zéolithes sans OSDA et possédant des dimensions de cristallite de taille nanométriques.

Tableau 2: Synthèse de zéolithes nanométriques sans OSDA avec les températures de synthèse et les dimensions des unités de structures secondaires.

Références	Zéolithes	Cations	Température	Taille anneaux (T-atome)
28	Na-Y (FAU)	Na	90 °C	6-4
28	Na-X (FAU)	Na	60 °C	6-4
38,39	LTA	Na	25 °C	8-6-4
39	SOD	Na	25 °C	6-4
31	GIS	Na	180 °C (21d)	8-4
40	MOR	Na	-	12-8-5-4
26,27	EMT	Na	30 °C	6-4
41	LTL	K	175 °C	12-8-6-4
42	EDI	K	100 °C	8-4
43	LTJ	K	100 °C	8-6-4
44	ABW	Cs	180°C (22bars)	8-6-4
45	ANA	Cs	180 °C	8-6-4
Ce travail	RHO	Na, Cs	90 °C	8-6-4
Ce travail	RHO	Na, K, Cs	90 °C	8-6-4
Ce travail	CHA	Na, K, Cs	90 °C	8-6-4
Ce travail	BPH	Na, K, Cs	25 °C	12-8-6-4
Ce travail	EDI	Na, K, Cs	90 °C	8-4
Ce travail	ANA	Na, K, Cs	90 °C	8-6-4

Iwama et collaborateurs[46] ont mis en évidence que l'ajout, même tardif, de KOH, change l'orientation de la structure formée par la zéolithe finale. Ils ont essentiellement étudié le mécanisme cristallisation de la FAU-X et le rôle des ions inorganiques a été discuté. Leur conclusion est que le taux de potassium limite considérablement la formation sélective de LSX (Type de FAU « low silica X »). Les ions potassium empêchent la cristallisation de la zéolithe LTA en phase liquide au cours de la première étape de la cristallisation (Figure 5). Cette précipitation empêche de la nucléation de la zéolithe A et favorise la nucléation de LSX dans la phase d'hydrogel. La localisation de l'ion potassium proche du centre des D6R, suggère que l'ion potassium a une importance fondamentale dans l'assemblage des tétraèdres dans le processus de construction de FAU.

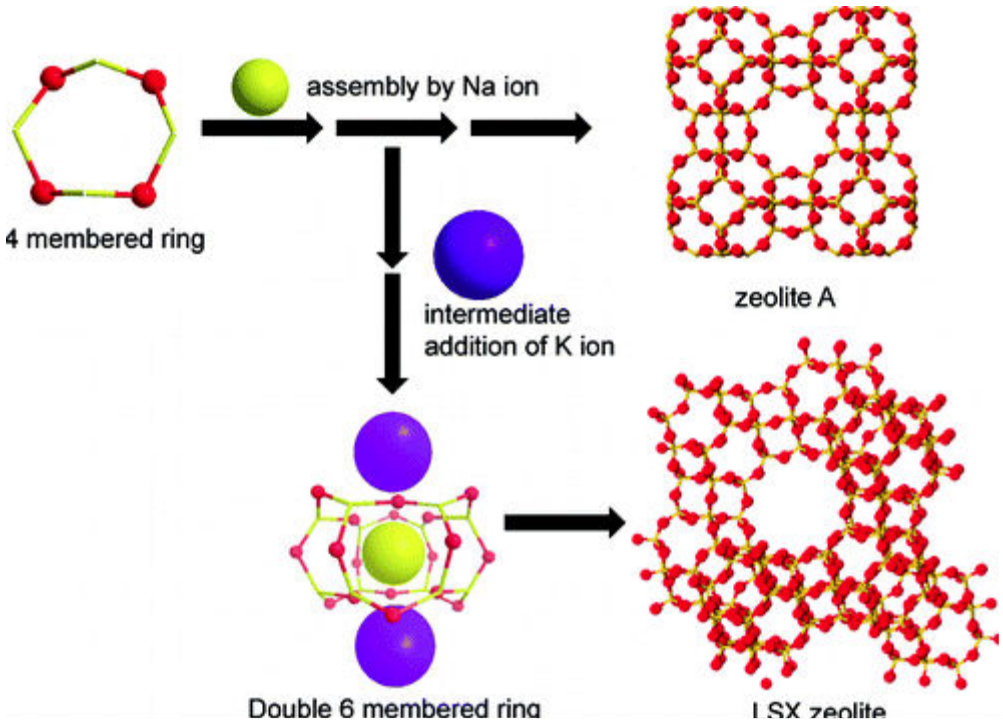

Figure 5: Schématisation du processus de synthèse de LSX (acronyme de l'anglais « low silica X »: type de FAU) avec un ajout tardif de KOH. (Recopié de [46])

Cette observation va considérablement nous inspirer pour orienter la nucléation vers les zéolithes désirées, la CHA et la RHO.

F. Synthèse de zéolithes à petit micropores

Dans cette partie, nous nous intéresserons exclusivement aux zéolithes dites « à petits pores », c'est-à-dire les zéolithes avec pour plus grande microporosité des 8-MR.

Au cours de la dernière décennie, les zéolithes à petits pores ont d'avantage été au centre des attentions que les tamis moléculaires à moyen et large pores. La raison vient de la

commercialisation de catalyseurs développés pour l'élimination des émissions de NOx et la conversion du méthanol en oléfines légères (C_2-C_3). Le véritable enjeu de ces structures vient des accès limités des molécules aux cages de la structure cristalline. Ainsi, l'entrée et la sortie des pores n'est possible que pour les petites molécules, offrant une sélectivité de forme et de taille aux réactions chimiques que l'on souhaite étudier. Au total, il existe quarante-quatre structures différentes de zéolithes à petits pores. Les dix plus communes sont représentées dans la Figure 6 avec la schématisation de leur cage.

Cette partie s'orientera donc sur la synthèse des zéolithes à petits pores en évoquant quelques applications d'intérêt industriel. Une attention particulière sera portée aux zéolithes CHA et RHO qui sont au cœur de ces travaux de thèse.

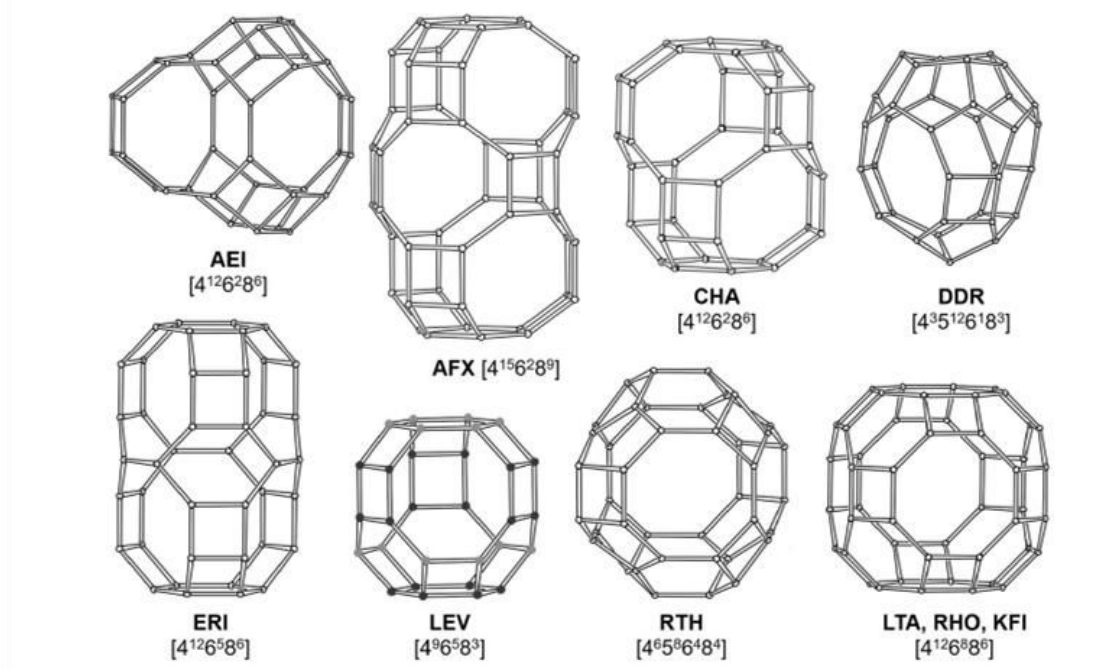

Figure 6: Exemple des cages des 10 zéolithes à petits micropores pores les plus étudiées. Le nombre de T atomes des pores et leur quantité par cage (en exposant) sont indiqué entre crochets.[47]

1. *Synthèse de RHO*

La cage *lta* ou (α) est commune aux 3 structures, LTA, KFI et RHO. Les cages étant reliées par les unités de structure secondaires *D8R* dans le cas de RHO. La substitution d'une partie des cations Na^+ par des cations Cs^+ dans la synthèse de LTA a été proposée par Robson en 1973[36]. Le rapport Na/Cs doit être précis pour éviter la formation de FAU (rapport trop faible) ou de ANA (rapport trop grand). Il est clair que le Cs dirige la formation des unités *d8r* et qu'il

aide à la formation des cages α. La voie de synthèse a été étudiée par de nombreux groupes permettant d'obtenir des structures RHO avec des rapports Si/Al compris entre 2.5 et 3.5.[48]

Burkett et Davis ont été les premiers à essayer d'utiliser les éthers couronnes 18-crown-6 et 15-crown-5 en présence de $CsNO_3$ lors d'une étude visant à synthétiser des structures de type EMT et FAU. Chatelain et collaborateurs[49] ont par la suite étudié cette synthèse et ont noté la formation de RHO en présence d'éther couronne avec un ratio Si/Al d'environ 4, supérieur aux valeurs obtenues jusque-là.

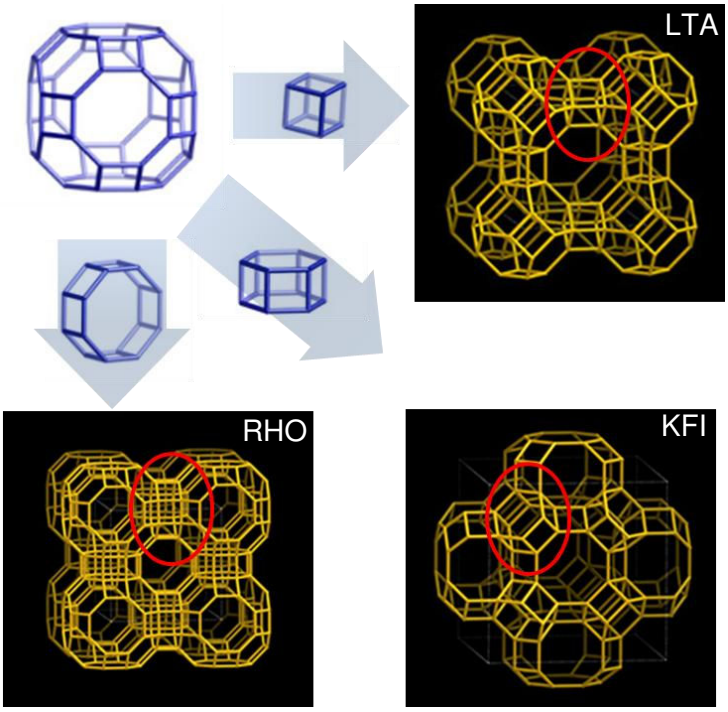

Figure 7: Disposions des USS formant les connexions entre les cages *Ita* conduisant aux structures RHO, KFI et LTA.

En 2017, Ke et collaborateurs[50] ont rapporté une synthèse particulière qui produit des zéolithes RHO avec des rapports Si/Al allant jusqu'à 8. La stratégie de synthèse consiste à utiliser un mélange équilibré de l'éther couronne 18-crown-6 avec du césium et du sodium. Ce complexe est formé de deux éthers complexant un atome de Cs. Cette voie de synthèse est la seule décrite qui permette de s'approcher de cristaux de taille nanométriques.

Le ratio Si/Al est très important pour l'analyse structurale de RHO. En effet, avec des ratios faibles (< 5), la structure oscille entre les groupes d'espace Im-3m (#229) et I-43m (#217).[51] Toutes les synthèses de RHO sans OSDA exhibent cette flexibilité et subissent le changement de phase avec une variation de température. Lors de ce changement,

impliquant une déformation de la fenêtre 8MR, la capacité de sorption du CO_2 peut être affectée.

2. Synthèse de CHA

La Chabazite est une zéolithe naturelle. La structure cristalline de la CHA a été résolue pour la première fois en1958 par Dent et Smith.[52,53] Il existe plusieurs types de matériaux dont la structure est analogue à la CHA (Figure 8a). Le seul contraste entre eux provient de la composition chimique: les aluminosilicates SSZ-13 et CHA ont un rapport Si/Al respectivement supérieur et inférieur à 5. Les zeotypes AlPO-5 et SAPO-34 ont également la structure type CHA et sont respectivement un aluminophosphate et un silicoaluminophosphate. Leur structure tridimensionnelle est constituée de cages de *cha* reliées entre elles par des prismes hexagonaux (D6R). La cage a un diamètre de 8 nm et une hauteur de 10 nm, accessible par des fenêtres de 0,38 nm de diamètre.

La Figure 8b montre le réseau formant la structure de la zéolithe CHA ainsi que les 4 sites extra-réseaux**:** à l'intérieur du centre d'un D6R (SI); à l'intérieur de la supercavité au-dessus d'un D6R (SII); à l'intérieur de la supercavité à côté d'un 4MR (SIII); au centre d'un 8MR (SIII ').

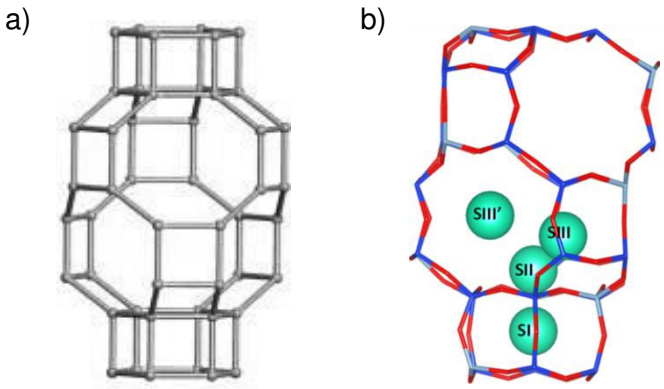

Figure 8: (a) Structure type CHA, (b) Unité de structure de type CHA avec localisation des sites extra réseaux.

La CHA est sans doute la zéolithe 8MR la plus intéressante du point de vue des applications industrielles de part sa structure bien spécifique.[47]

Utilisation d'agent structurant organique (OSDA)

Deux méthodes de synthèse de CHA sont particulièrement connues. La plus utilisée est la synthèse de la SSZ-13 (CHA), qui a été réalisée par S.I. Zones en utilisant la molécules

d'hydroxyde de N,N,N-triméthyladamantammonium (TMAdaOH).[54] Cette méthode, bien que très efficace, présente l'inconvénient majeur de devoir ajouter une étape de calcination du composé organique coûteux et non recyclable.

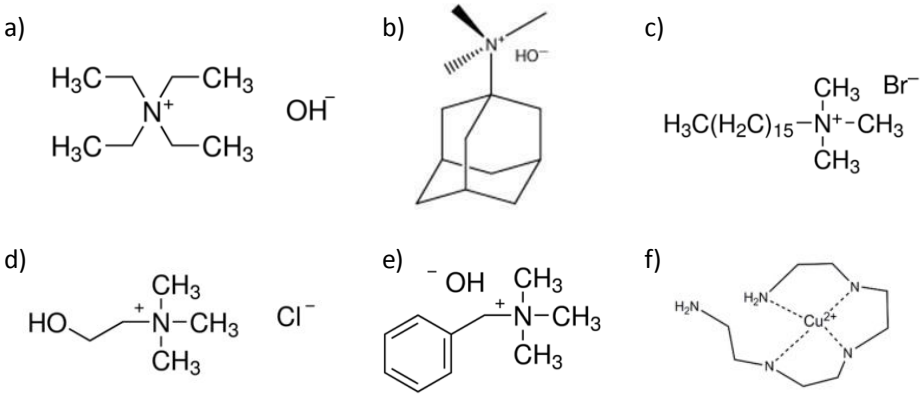

Figure 9: Liste des OSDA mentionnés pour la synthèse de CHA : a) TEAOH (Tetraethylammonium hydroxyde), b) TMAdaOH (Tetramethyladamantylammonium hydroxyde), c) CTAB (hexadecyltrimethyl ammonium hydroxyde), d) Choline chlorure, e) BTMB (Benzyltrimethylammonium bromure), f) Cu^{2+}TEPA (Cu-tetraethylenepentamine).

Depuis, de nouvelles molécules été proposé dans la littérature telle que la N,N,N-diméthyléthylcyclohexylammonium[55] ou le complexe Cu^{2+}-TEPA...[56–58] La liste des molécules utilisées comme structurant organique (OSDA) est représentée dans la Figure 9.

Transformation par conversion interzéolitique

M. Bourgogne et collaborateurs[59] ont fait une avancée majeure en 1985 pour proposer une méthode de transformation de FAU en CHA dans des conditions alcalines. Cette transformation a été largement étudiée pour la recristallisation de la H-FAU en présence de KOH afin d'obtenir un rapport Si/Al compris entre 2 et 11. Il est intéressant de noter que T. M. Davis[60] et Van Tendeloo[61] ont également utilisé respectivement H-LEV et Na-FAU comme matière de départ avec cette méthode de transformation. Le principal défaut de la méthode est que la synthèse est très longue: pouvant aller jusqu'à 15 jours.

L'obtention d'aluminosilicate CHA avec des tailles nanométriques est peu répandue. Quelques articles proposent des voies de synthèses viables pour obtenir ces matériaux. Cependant, dans ces articles, les nanocristaux ont amélioré les performances du catalyseur pour des réactions chimiques telles que la réaction de Knoedenagen[62] et la conversion de méthanol en oléfines (MTO).[63]

La première méthode a été proposée en 2016 par C. Arnaud[62]. La réduction de la taille de particule de CHA est effectuée par broyage à billes, appelé « ball milling ».[64,65] Cette voie de synthèse préliminaire permet la recrystallisation et réduction de la taille de CHA. Les autres

méthodes existantes pour la synthèse mono-étape de CHA nanométrique doivent combiner quelques méthodes développées précédemment. Z. Li et collaborateurs ont proposé une synthèse de CHA produisant des cristaux de taille nanométriques, en utilisant du bromure de triméthyl-1-adamantanammonium et un surfactant moléculaire, l'hexadécyl-triméthyl-ammonium[63]. On peut citer l'exemple de M.Zhou[66] qui a utilisé des composés fluorés, couplés à des OSDA. T.Takata et collaborateurs[67] ont combiné la recristallisation de la FAU à des germes de SSZ-13 et le TMAdaOH pour la synthèse de CHA nanométrique.

Plus globalement, la littérature nous renseigne sur 3 autres méthodes de synthèses de CHA beaucoup plus récente.

Assistance de germes

H. Imai et ses collègues[18] ont proposé d'autres méthodes de synthèse de CHA en utilisant une approche « par germe ». Cette méthode consiste en la synthèse de zéolithes de CHA sans agent structurant organique mais en ajoutant de grandes quantités de germes de SSZ-13 préparées de manière classique (20% en poids). Cette méthode présente un intérêt conséquent qui est d'abaisser le temps de synthèse de plusieurs jours dans le cas des synthèses mentionnées précédemment. De plus, le rendement est considérablement amélioré (jusqu'à 72%). En revanche, les particules formées sont des agrégats de plus 2µm et le rapport Si/Al minimal obtenu est de 2.5, rendant ce matériau plutôt intéressant pour des applications en MTO (méthanol à oléfines) et SCR (réduction catalytique sélective) que pour la séparation de gaz.

Synthèse en voie fluorure

B. Liu et collaborateurs[68] ont été les premiers à proposer une méthode de synthèse de CHA sans OSDA et sans germes à l'aide de NH_4F. Cette méthode limite les défauts de la zéolithe mais produit des cristaux particulièrement gros (plus de 15 µm). Par conséquent, l'efficacité est considérablement réduite pour les applications d'adsorptions de gaz ou catalytiques.

Résumé

Le Tableau 3 liste les voies de synthèse qui ont conduit aux zéolithes CHA. Comme mentionné, la recette standard pour la synthèse de CHA sans OSDA avec de fortes teneurs en aluminium est basée sur la transformation d'une zéolithe FAU, LTA ou de «fly ash» à 95°C. Les autres méthodes de synthèses mènent à la formation de CHA avec des rapports Si/Al plus grand, et donc plus à intéressant pour application en catalyse chimique: réactions SCR (réaction catalytique sélective) ou MTO (méthanol en oléfines).

Tableau 3: Résumé des différentes méthodes de synthèse de Chabazite incluant les conditions de synthèses et les applications à l'échelle du laboratoire des matériaux obtenus. MTM : Méthane à méthanol / MTO : Méthanol à oléfines / SCR : Réduction catalytique sélective

Réf.	Matériaux de départ	Agent Chélatant	OSDA	Si/Al (w/w)	Conditions de synthèse	Taille nano (Y/N)	Applications
[59]	NH_4-FAU (CBV 300, Zeolyst, 2.6)	KOH	-	2.1	95°C – 15d	N	Gaz séparation MTM
[69]	NH_4-FAU (CBV 300, Zeolyst, desalum 2.6 => 6)	KOH	-	6	95°C – 15d	N	MTO
Ce travail	NH_4-FAU (CBV 720, Zeolyst, 13)	KOH	-	2.3	95°C – 4d	Y	-
[63]	H-FAU + SSZ-13 (germes)	NaOH / NaCl	BTMAOH/ TMAdaOH / TEAOH	25	160°C	Y	SCR
[67]	FAU + SSZ-13 (germes)	KOH	TMAdaOH	13-6	135°C	N	-
[70]	Na-Gis	NaOH	$TMAda^+ I^-$	7.5	135°C -1d	N	CO_2 adsorption
69	H-LEV (9)	NaOH	-	2.8-5.0	90-180°C	N	-
16	LTA	NaOH	TMAdaOH	4.7-8.9	130-180°C	N	SCR
[56]	USY (CBV-720, 10.5) + SSZ-13 (germes)	NaOH	Cu-TEPA + TEA	10.3	160°C -9d	N	SCR
[72]	« Ash fly » (Si/Al=2)	KOH	-	1.9-2.2	650°C-1.5h puis 95°C- 4d	N	- Gaz séparation - Cs adsorption
18	SSZ-13 (germes)	KOH / CsOH	-	2.5-6.1	170°C – 1d	N	MTO
[68]	-	NH_4F	-	2.5-3.5	140-180°C	N	-
Ce travail	-	NaOH + KOH + CsOH	-	1.5-2.5	90-140°C	Y	Gaz séparation

III. Effet Trapdoor

La sélectivité à l'équilibre d'un gaz par rapport à un autre provient des différences d'interaction électrostatique entre l'adsorbant et le sorbate. Afin d'examiner les différents types d'interactions adsorbant-sorbate liées à cette étude, il convient de prendre en compte certaines propriétés du CO_2, du N_2 et du CH_4 (Tableau 4). Pour cette étude, seul le diamètre cinétique (dimension de la molécule) sera considéré.[73]

Tableau 4: Données cinétiques et potentiels des molécules hôtes pouvant pénétrer dans les cages des zéolithes.

	Diamètre cinétique (Å)	Moment dipolaire (10^{-30} C m)	Moment quadripolaire (10^{-40} C m^2)	Polarisabilité (10^{-25} cm^3)
CO_2	3.3 Å	0	-13·4 ± 0·4	0
CH_4	3.8 Å	0	0	26.0
N_2	3.64 Å	0	-4·72 ± 0·26	17.4
CO	3.69 Å	0.36	-8·58 ± 0·35	19.5
H_2O	3.43 Å	6.19	-	-

L'effet de tamisage moléculaire découle généralement de la taille de l'ouverture des canaux de la zéolithe et de la cinétique due au diamètre des molécules à séparer. Les petites molécules entrent alors que les molécules trop volumineuses ne pénètrent pas dans les pores (ou cages). Les zéolithes à petit pores sont idéales pour induire une sélectivité de forme et séparer le CO_2 du N_2 et du CH_4.

A. La séparation gaz sur la LTA

La séparation de gaz sur la LTA est probablement le plus étudié des procédés de séparation par les zéolithes. En 2010, Miguel Palomino et collaborateurs sont les premiers à étudier la LTA sur une large gamme de rapport Si/Al pour séparer le CO_2 et le CH_4 et ainsi identifier l'impact de ce paramètre essentiel sur la sélectivité de ces gaz.[50]

Ils ont analysés les capacités d'absorption, la quantité de la séparation et l'énergie d'absorption sur des LTA pour Si/Al=1, 2, 3.5, 5 et pure Si. Ils ont ainsi démontré que l'énergie d'adsorption du CO_2 augmente lorsque la teneur en Al dans la zéolithe LTA

augmente. Par conséquent, la capacité de régénération de l'adsorbant diminue à mesure que le contenu en Al augmente. Au contraire, la teneur en Al a peu d'effet sur la chaleur isostérique de l'adsorption de CH_4 sur des échantillons de LTA. La sélectivité CO_2/CH_4 dépend fortement de la pression opératoire et du nombre de cations compensant la charge de la structure (soit la quantité d'Al). La sélectivité diminue exponentiellement avec l'augmentation de la pression d'adsorption. En revanche, cette diminution exponentielle s'atténue avec la diminution du taux d'Al, au point que la LTA purement silicique donne une sélectivité presque constante proche de 3,5. Ils ont également observé que la régénération est rapide et complète avec des zéolithes LTA riches en Si.

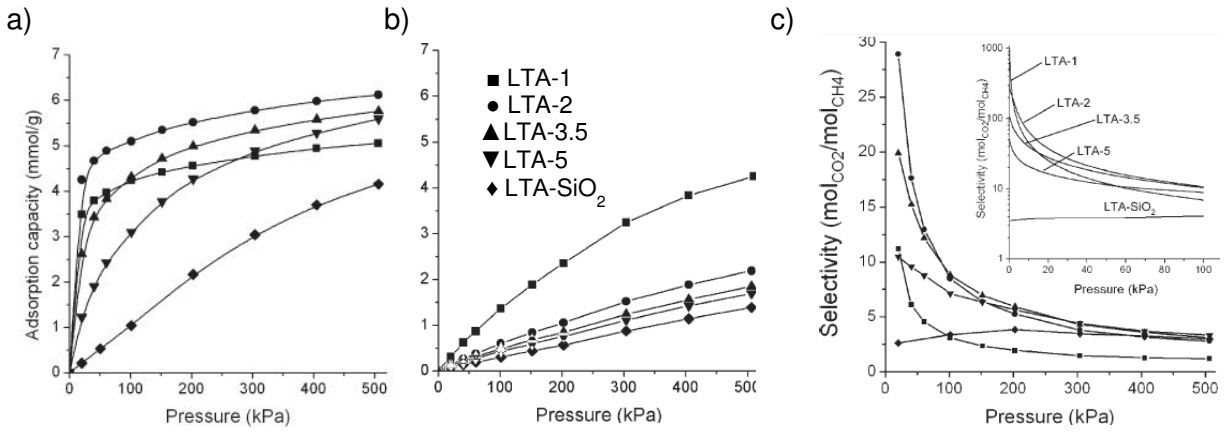

Figure 10: (a) Isothermes d'adsorption de CO_2 (b) et CH_4 sur LTA à différent ratio Si/Al à 30°C et à différentes pressions. (c) Sélectivité CO_2/CH_4 sur LTA.

La Figure 10a montre la capacité d'absorption en fonction de la pression de CO_2 dans le système. Le constat est que la capacité d'absorption maximal est obtenue à forte pression pour un rapport Si/Al = 2>3.5>5>1>∞. En revanche, l'absorption de CH_4 est proportionnelle à la quantité d'atomes d'aluminium: la zéolithe absorbant le plus de CH_4 est celle avec un Si/Al = 1 et celle qui en absorbe le moins est la plus silicique. La sélectivité CO_2/CH_4 dépend donc fortement de la pression et du nombre de cations compensant la charge de la structure (égale à la quantité d'atomes d'Aluminium). La sélectivité diminue exponentiellement avec l'augmentation de la pression d'adsorption.

Globalement, la sélectivité de la LTA est comparable aux autres zéolithes telles que la RHO et CHA: à 100 kPa, la meilleure sélectivité ne déplace pas 10. La grande différence entre la LTA et les autres zéolithes étudiées vient de l'inaccessibilité de la cage *sod* vis-à-vis du CO_2.

Pour améliorer la sélectivité, il a été récemment proposé de substituer des atomes de Na^+ par du K^+ .[74,75] Ils ont observé que les cations K^+ remplacent le Na^+ dans les sites 8MR et bloquent l'adsorption de N_2 ou de CH_4. Une diminution progressive de l'adsorption de CO_2 est observée avec l'augmentation du rapport $K^+/(Na^+{+}K^+)$ au point de ne plus pouvoir absorber de CO_2 lorsque tout le Na est substitué. La valeur optimale proposée est $K^+/(Na^+{+}K^+)=0.25$. Pour cette valeur, les sélectivités CO_2/N_2 et CO_2/CH_4 ont été considérablement améliorées pour l'échantillon (Na_9K_3)-LTA comparé à Na_{12}-LTA ou α (CO_2/CH_4) passe de ~3.4 à 1040 et l'α (CO_2/N_2) passe de ~6 à 420. Les expériences PXRD in situ ont permis la localisation du K^+ à l'entrée de la fenêtre à 8MR, les rendant responsables de l'amélioration de la sélectivité.

Dans cette partie nous avons vue que la capacité d'absorption pour une structure donnée, dépend de deux paramètres: le rapport Si/Al et la nature des cations compensateurs. Nous nous attendons à ce que la zéolithe Chabazite développe le même comportement.

B. L'effet Trapdoor sur la Chabazite

La grande différence entre la LTA et la Chabazite vient de la forme et l'accessibilité de la cage. En 2012 Shang et collaborateurs[76,77] ont proposé un mécanisme différent générant une haute sélectivité pour les molécules particulières telle que CO/N_2 ou CO_2/CH_4 sur la zéolithe Chabazite. Par la suite de très nombreux articles seront publiés sur ce qu'ils ont appelé « l'effet Trapdoor »[76,78–81].

Le phénomène a pour origine la topologie de la chabazite dont les cages sont accessibles par le biais de fenêtre à 8 tétraèdres (8MR). Ces 8MR sont suffisamment grands pour que le CH_4, N_2 et CO_2 puissent entrer dans la supercage. Cependant, son accès est bloqué par la présence de cations Cs^+, Rb^+ ou K^+ (Figure 11). Ces cations occupent la position énergétiquement la plus favorable se trouvant dans le centre de la fenêtre 8MR. Seuls les 3 cations mentionnés vont se localiser dans la fenêtre, alors que les cations Na^+, H^+, Cu^+, Ag^+, Ca^{2+} trouvent d'autres localisations (SII ou SIII), laissant libre l'accès aux cages.[82]

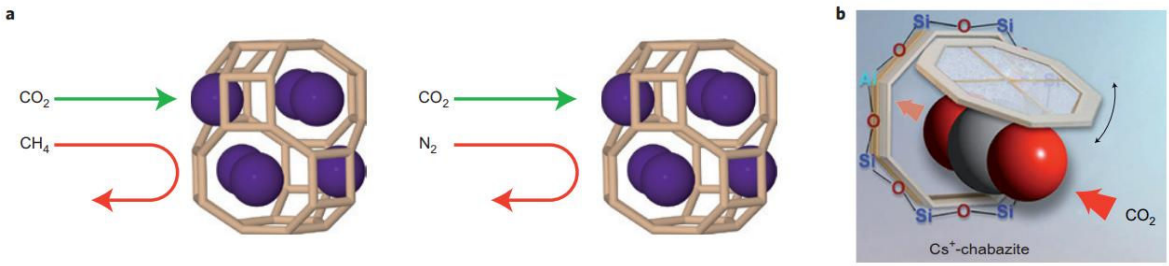

Figure 11: (a) Schématisation de la sélectivité vis à vis du N_2 et (b) modélisation du mécanisme d'ouverture de la fenêtre 8MR par le potassium au contact du CO_2, conduisant à l'effet Trapdoor [79]

La structure de CHA avec différents cations compensateurs a fait l'objet d'études très poussées en diffraction de neutrons, RX et MAS-RMN (Figure 8a). Les cations n'ont pas la même localisation selon leur taille et leurs charges mais également selon la quantité d'atomes d'aluminium dans la charpente.[82]

L'analyse structurale de la CHA contenant du CO_2 a été étudié par de nombreux groupes et notament sur les CHA purement siliciques et échangées avec du Li, du Na et du K.[76,83–85] Pour la chabazite, le rapport Si/Al modifie fondamentalement les phénomènes d'adsorption.

Pure silicique SSZ-13 (ratio Si/Al =∞):

Le site III' (8MR) a été identifié comme le principal site d'adsorption du CO_2 dans les Chabazites purement silicique: les 8 atomes d'oxygène de la structure interagissent fortement avec le CO_2. Le reste des molécules de CO_2 s'adsorbe au centre de la cage, interagissant les unes aux autres. Les isothermes d'absorption du CO_2 montrent un comportement de type Dual-site Langmuir avec très peu de CO_2 absorbé chimiquement.[86]

r12-CHA (ratio Si/Al =12):

Les cations Li^+ et les cations Na^+ ont été observés uniquement au site SII du D6R (Figure 8b).[87] Les cations K^+ et Cs^+ peuvent occuper les sites D6R (SII) et 8MR (SIII').[83] Dans tous les cas de figures, le cation offre la possibilité d'une liaison forte par polarisabilité avec l'adsorbat. Le dioxyde de carbone est coordonné aux cations par physisorption (M^+---O=C=O) dans l'axe parallèle au 4MR pour maximiser son interaction de dispersion avec les oxygènes de la structure.

r6-CHA (ratio Si/Al =6):

Dans ce cas de figure, le nombre de cations augmente proportionnellement au nombre d'atomes d'aluminium permettant aux cations d'accéder à d'autres sites. La population mixte de sites d'adsorption explique le désordre élevé du deuxième site d'adsorption. La coordination du CO_2 avec ces cations métalliques diminue avec la dureté du cation $Li^+ > Na^+ > K^+ > Cu^{2+}$ sauf dans le cas du K^+, où les complexes pontés de CO_2 avec deux sites de cations K^+ ont été formés avec une énergie d'interaction supérieure à celle d'un seul site d'adsorption de cations.[83]

De plus, une importante adsorption de CO_2 sur le site dans la 8MR (site III') a encore été observée.[83] Le fait que la plupart des sites III' soit laissé libre, aucun effet Trapdoor ne peut avoir lieu.

r3-CHA et moins (ratio Si/Al < 3): Effet Trapdoor.

Comme exprimé precedemment, l'effet trapdoor ne peut etre observé que lorsqu'il y a un atome sur chaque site III'. Cela se produit seulement si le ratio Si/Al est inferieur à 3. Ce cas correspond à la situation où se trouve un atome d'aluminium par fenetre 8MR. A partir de ce constat, il est possible d'envisager une selectivité polaire. Si on comprend que ni les cations Na^+, Li^+ et Cu^{2+} ont pour vocation à occupé le site III', alors il n'y a de selectivité de polarité qu'avec les cations K^+, Rb^+ et Cs^+.[77]

Pour que les molécules puissent entrer dans les cages, le cation doit s'écarter du centre de la fenêtre 8MR. Il faut pour cela générer une interaction et augmenter l'énergie cinétique des cations, ce qui explique pourquoi au-dessus d'un certain seuil de température, tout les gaz avec un diamètre de moins de 3.8 Å peuvent accéder aux cages.

Grace à des calculs DFT (« théorie de la fonctionnelle de la densité »), Shang et collaborateurs ont expliqué le mécanisme de «l'effet trapdoor»[76]. En effet, les molécules de CO_2 créent une déformation du potentiel du cation, due au grand moment quadripolaire électronique et de la polarisabilité de la molécule. Le CH_4 et N_2 ne peuvent pas interagir suffisamment avec le cation pour lui faire passer la barrière de potentiel nécessaire à une migration. Cela provoque temporairement et de façon réversible une migration du cation qui s'éloigne du centre de la 8MR, ouvrant la voie à la molécule de CO_2. Il existe un seuil de température critique appelé Tc indépendant pour chaque molécule absorbée dans la chabazite. La variation du seuil de température d'entrée est corrélée à la taille de la molécule. Ainsi Li et collaborateurs proposent d'utiliser la Chabazite et l'effet Trapdoor pour faire de la séparation de gaz en modifiant la température ou faire du stockage de H_2 ou de CH_4 sans pression et d'en réguler thermiquement la libération[88].

Hong et collaborateurs ont étudié la performance de capture de CO_2 de CHA mésoporeuse sous haute pression et à température modérée[63]. Ils ont étudié les performances de capture de CO_2 de la zéolithe dans des conditions de température et de pression modérées. L'introduction de mésopores dans CHA conduit à l'augmentation des capacités de captage du CO_2 de la CHA après échange ionique dans des conditions de haute pression. Ainsi, la capacité d'adsorption de CO_2 a augmenté dans l'ordre suivant: LiCHA > CaCHA > NaCHA > MgCHA à 25°C.

La méthode de recristallisation de «fly ash» (aluminosilicate non poreuse) a permis d'obtenir de la CHA sans utiliser d'OSDA.[72,78] Les chabazite résultantes avaient une grande cristallinité et une mesure plus de 20µm. En revanche, les capacités d'adsorption de CO_2 sur la r1.9-KCHA (100 kPa, K^+ comme cation et Si/Al=1.9) sont relativement faibles comparées

aux résultats préalablement cités : 0.81mmol/g, 1.49mmol/g et 1.54mmol/g à respectivement 0°C, 30°C and 60°C.

C. L'effet « swing » sur la RHO

En 2012, Palomino a publié une communication sur l'utilisation de RHO pour séparer le CO_2 et le CH_4 [89]. La zéolithe Na-RHO est aussi capable de générer le phénomène de sélectivité de polarité. Les cations extra-réseau se localisent au centre des fenêtres de la cage α qui est le seul accès possible aux cages de la zéolithe RHO. Tandis que le dioxyde de carbone peut diffuser à travers ces fenêtres, le méthane et d'autres molécules gazeuses non polaires ne peuvent pas y diffuser, conduisant à un fort potentiel de séparation des gaz.

En 2017, Coudert et Kohen[90] ont étudié le phénomène déclencheur en utilisant des simulations de dynamique moléculaire *ab-initio* combinées aux méthodes d'énergie libre. D'après leurs calculs, le CO_2 interagit lorsque le cation de la zéolithe Na-RHO oscille thermiquement dans et en-dehors de son site, permettant au CO_2 d'entrer dans la cage. Dans ce schéma de l'adsorption sélective du CO_2, les cations de Na dans les anneaux 8MR agissent comme des portes battantes, agités par un mouvement thermique, à travers lequel le CO_2 peut passer pendant qu'elles sont entrouvertes. Quant au méthane, sans la forte interaction adsorbat-zéolithe et donc un site d'adsorption à l'entrée de la porte, il doit passer une barrière d'énergie beaucoup plus grande même lorsque le cation est un peu en dehors de la porte. Ceci serait à l'origine de la grande sélectivité démontrée expérimentalement par Paul Wright[91]. Comme il n'existe aucune donnée expérimentale permettant de prouver le mécanisme de diffusion, la dynamique moléculaire est la technique de simulation la plus adéquate pour valider le schéma de l'adsorption de CO_2. Leurs conclusions invalident le mécanisme « Trapdoor » pour la zéolithe RHO. D'après cette étude théorique, la présence de CO_2 n'affecte pas de manière significative le mouvement du cation. Le mécanisme alternatif propose que l'amplitude du mouvement thermique des cations est suffisamment grand pour que le CO_2 puisse diffuser lorsque la porte est ouverte, alors que les molécules non polaires telles que le méthane ne le peuvent pas. Ce mécanisme s'apparente d'avantage au mouvement de portes battantes que de celui lié à un piège.

IV. Conclusions

De manière générale, cette introduction permet de mettre en lumière les objectifs, les difficultés et les enjeux de la séparation du CO_2 du CH_4 (ou de N_2). Bien que les matériaux microporeux offrent une alternative très intéressante, il reste à déterminer les propriétés physicochimiques idéales pour leur utilisation dans les procédés d'adsorption.

De nombreux matériaux ont été étudiés pour l'adsorption du CO_2. La démonstration de l'efficacité des zéolithes à petit micropores a été mise en avant dans de nombreux travaux. Ainsi, les méthodes de synthèse doivent être pensées et orientées pour favoriser la formation de zeolites possédant les propriétés physicochimiques les plus adaptées. Les zeolites à petits micropores (CHA, RHO, LTA …) sont celles qui semblent les plus prometteuses.

La synthèse des zéolithes CHA et RHO sont particulièrement intéressantes puisque le développement de ces zéolithes à l'échelle nanométriques est très peu répandu. Tout un aspect de l'adsorption sur les nanozéolithes à petits micropores reste inexploré à ce jour. De plus, le nombre d'articles traitant du développement de CHA et RHO nanométriques est très restreint et proposent systématiquement l'utilisation d'agents structurants organiques (à l'exception de la méthode de « ball milling »). C'est à partir de ce constat que le choix de développer des nanozéolithes CHA et RHO a été fait. Le but est de modifier la synthèse pour obtenir les matériaux avec les propriétés physicochimiques optimales décrites par la littérature.

CHAPTER 2: MATERIELS ET METHODES

This chapter provides a general overview of the hydrothermal synthesis of CHA type zeolites.

It is explained in the previous chapter that the final capacities of the materials are closely related to its chemical composition, its structure and its microstructure.

This chapter describes the characterization techniques used to study the structure, the microstructure, chemical composition of materials and the adsorption of N_2 and CO_2 in the CHA type zeolites.

I. Synthesis of template free zeolites

A. Starting materials

The starting materials used in the synthesis of CHA type zeolites are listed below:

- sodium hydroxide (NaOH): (pellets): Sigma Aldrich;

- potassium hydroxide (KOH) (pellets >85%): Sigma Aldrich;

- cesium hydroxide (aqueous 50%): Alfa Aesar;

- colloidal silica (Ludox-HS 30, 30 wt% SiO_2, pH = 9.8): Sigma Aldrich;

- colloidal silica (Ludox-AS 40, 40 wt% SiO_2): Sigma Aldrich;

- sodium aluminate ($NaAlO_2$, Al_2O_3 55%, Na_2O 45%): Sigma Aldrich

B. Synthesis procedure

1. Synthesis of micronsized CHA zeolite

r2.0-CHA: The template-free micronsized CHA zeolite was prepared from a precursor mixture with a molar composition: 8 Na_2O: 1.25 K_2O: 0.30 Cs_2O: 0.8 Al_2O_3: 10 SiO_2: 120 H_2O.

Step 1): A clear aqueous aluminate **solution A** was prepared by dissolving 0.512g of sodium aluminate ($NaAlO_2$) in 3.34g of dd H_2O. A clear aqueous silicate **solution B** was prepared by mixing 6.667g of colloidal silica (LUDOX HS30) with 1.94g of NaOH, 0.550g of KOH, 0.599g

of CsOH (aq. 50%). As a result, a worm turbid suspension was obtained due to the exothermic reaction. The turbid turns into clear suspension after 10 minutes and it is stirred for additional 1h.

Step 2): **Solution A** was added dropwise under vigorously stirring to the **solution B** kept in ice.

Step 3): The resulting clear suspension was then aged 20h at room temperature (i.e. 25 °C).

Step 4): Then, the hydrothermal crystallization was conducted at 90 °C for 8 h to obtain different types of particles in terms of size, morphology, chemical composition. The time of hydrothermal treatment depends on the temperature and the chemical composition.

Steps 5) and 6): The CHA zeolite samples were purified by repeating steps of centrifugation (20000 rpm for 20min) and dispersed in distilled water until reaching pH=8 of the decanting solution, and then the solid product was freeze-dried.

2. Synthesis of nanosized CHA zeolite

r2.5-CHA : The template-free nanosized CHA zeolite was prepared from a precursor mixture with a molar composition: 6 Na_2O: 1.25 K_2O: 0.20 Cs_2O: 0.6 Al_2O_3: 16 SiO_2: 140 H_2O.

Step 1): $NaAlO_2$ (m=0.54g, Sigma Aldrich) as aluminum source was dissolved in ddH2O (m=3.2g). NaOH (m=1.47g, 97%, Sigma Aldrich) and KOH (m=0.54g, 85%, Sigma Aldrich) and CsOH (m=0.40g, 50%) was added to the aluminum solution to form a clear solution. Step 2): The Ludox-AS40 (8.0g, 40 wt% SiO_2, Sigma Aldrich) was added dropwise to hydroxide solution under vigorous stirring.

Step 3): The resulting suspension was aged at room temperature for 12 days under stirring conditions. During this period, the white suspension turned clear after 3h of stirring.

Step 4): Then, the hydrothermal treatment was performed at 90 °C for 7 h.

Step 5): The crystalline product was diluted with 80 °C double distilled water, purified by centrifugation (20000 rpm, 20 min) and finally dispersed in ddH_2O. The resulted suspension was dried at 60 °C for further characterization and the rest was kept as suspension for post-synthetic modifications.

3. Synthesis of nanosized BPH and RHO type zeolites

The template-free, nanosized RHO zeolite was prepared from the precursor suspension with a molar composition: 8 Na_2O: 0.60 Cs_2O: 0.8 Al_2O_3: 10 SiO_2: 90 H_2O.

The suspension was aged at room temperature for 20 h under stirring. This time, the hydrothermal treatment was performed at 90 °C for 2 h.

The template-free, nanosized BPH zeolite was prepared from a precursor suspension with a molar composition: 8 Na_2O: 1.25 K_2O: 0.30 Cs_2O: 0.8 Al_2O_3: 10 SiO_2: 120 H_2O.

Table 5: Conditions scope of the new CHA, RHO and BPH synthesis.

Sample	Chemical composition						Hydrothermal treatment	
	Na_2O	K_2O	Cs_2O	H_2O	SiO_2	Al_2O_3	Temp.	Time
r-2.0-CHA micronsized	8.0	1.25	0.30	120	10	0.8	90	7 h
r-2.0-CHA nanosized	9.5	0.85	0.35	140	16	0.8	90	7 h
r2.5-CHA nanosized	6.0	1.25	0.20	140	16	0.6	90	8 h
RHO	8.0	-	0.60	90	10	0.8	90	2 h
BPH	8.0	1.25	0.30	120	10	0.8	RT	12 days

The resulting suspension was kept at room temperature for 12 days under stirring. The resulted white suspension was purified directly and then subjected to characterization.

The Table 5 resumes the conditions synthesis of the nanosized CHA, BPH, RHO and micronsized CHA.

The synthesis procedure for CHA zeolite is shown in Figure 12. It consists of mixing of hydroxides source and colloidal silica suspension, and then the aluminium source was added into the silica suspension.

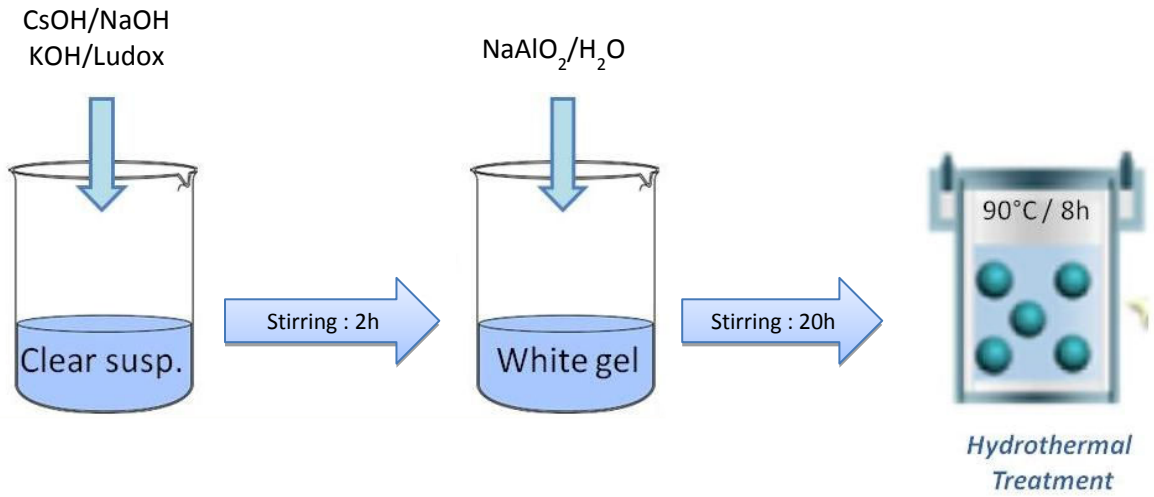

Figure 12: The procedure applied for synthesis of CHA type zeolite.

C. Ion exchange

In order to test the influence of cation effect on the CO_2 adsorption, the Na^+, K^+, Cs^+ cations were introduced in the purified samples by ion exchange (samples will be abbreviated as H-CHA, Na-CHA, K-CHA, Cs-CHA). Cation' nitrate solutions were used with a concentration of 0.1 M; the zeolite sample (0.2 g) was mixed with the solution (25 mL). This mixture is stirred overnight at room temperature. Afterwards the solution was filtered and washed with distilled water, and the zeolite powder was separated. This whole process is repeated one to three times depending on the requirements. Finally the samples were dried overnight in an oven at 50 °C prior to calcination. The chemical composition of the samples was determined by inductively coupled plasma mass spectroscopy (ICP).

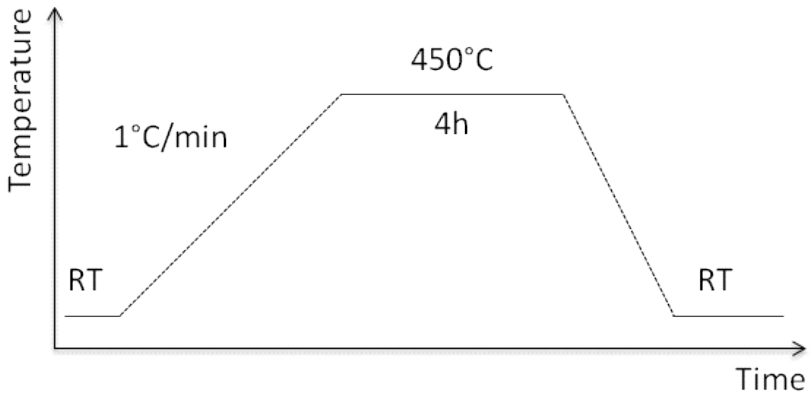

Figure 13: Scheme of the calcination procedure applied to zeolite samples after ion-exchange.

An ion exchange with NH_4NO_3 and $NaNO_3$ is adapted in order to keep the integrity of the zeolite and prevent collapsing of the structure. The material was ion-exchanged with a

solution of 0.1 M of NH_4NO_3 for 20 h at room temperature (i.e. 25 °C). The powder was washed twice by centrifugation (20000 rpm for 20 min). The procedure was repeated 3 times. Then the zeolite was washed with dd H_2O, and calcined (e.g. at 450 °C for 2h, ramp of 1°/min) in order to eliminate of the NH_3 and NOx and obtaining the acidic form of CHA (Figure 13).

II. Characterization

A good understanding of the physical and chemical properties of synthesized zeolite is the key of a proper functionalization for certain applications. Detailed information on the characterization techniques used in this work is provided in this chapter.

A. Powder X-ray diffraction (PXRD) analysis

1. Principe

A monochromatic X-ray beam is sent on a powder sample made of crystallites whose individual size can vary from tens of nanometers to tens microns. The irradiated part of the sample contains a very large number of crystallites that is assumed to be randomly oriented with respect to the incident X-ray beam. In this condition, there will always be a number of crystallites that will present a family of (hkl) planes satisfying the condition for having a diffraction event following the Bragg's law: $n.\lambda = 2\mathrm{d}.\sin\theta$. Bragg's law is useful to determine the distance between atomic planes (d_{hkl}) of the crystalline structure, based on the relationships between the diffraction angle (θ) and the wavelength (λ) of the incident X-ray beam. In powder X-ray diffraction (PXRD), (hkl) planes from different crystallites will diffract simultaneously forming a cone of diffracted beams whose axis of rotation is the direction of the incident radiation with 2θ the half-angle value at its vertex (Figure 14a). The recorded PXRD pattern corresponds to a one dimensional section of the diffraction cones (Figure 14b). A powder diffractometer can present different configurations. In Bragg-Brentano configuration (reflection), the sample is plane and is placed in the center of the goniometer and in Debye-Scherrer configuration (transmission), the sample is introduced into a capillary placed in the center of the goniometer.

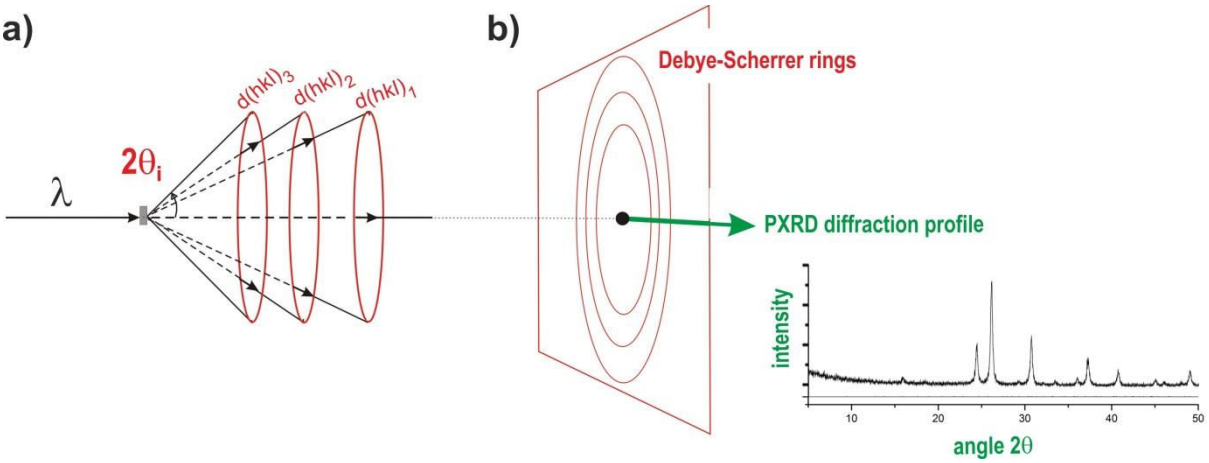

Figure 14: a) X-ray diffraction by a polycrystalline sample (Debye-Scherrer geometry). b) the detection of the diffracted intensities is usually done using a 1D detector in order to obtain a PXRD diffraction profile corresponding to a section of the Debye-Scherrer rings.

Zeolites are crystalline aluminosilicates whose structure is formed by a network of three-dimensional building blocks. Different zeolites will have their own unique PXRD patterns, so-called "fingerprint", used for phase and purity recognition. Attentive pattern interpretation is required in order to obtain detailed information about the zeolite structure, namely, peak position, intensity and width, which depend on the specific unit cell parameters and symmetry elements, type and position of atoms, crystallinity and average crystallite size respectively. The peak broadening is usually associated with the presence of small nanocrystals, whereas very sharp peaks indicate high material crystallinity, representative for micron sized crystals.

2. Refinements

Unit cell parameters of zeolite samples synthesized in this work were obtained from PXRD diffraction data by the Le Bail whole profile matching method[92]. This method allows refining the unit cell parameters taking into account a number of experimental parameters such as the peak's profile function (shape of the diffracted peaks), the zero shifts or the background. In this approach the I(hkl) intensities are extracted from the experimental patterns and not calculated based on the structure of the sample (type and position of atoms in the unit cell). It requires an approximate knowledge of the unit cell parameters (which are refined) and the space group of the sample. It is a convenient approach to obtain unit cell parameters when the structure is not or poorly known. It is also usually a preliminary step to check phase purity and fix profile functions before starting a Rietveld refinement.

The Rietveld method allows structure refinements based on the exploitation of the whole profile of the PXRD patterns[93]. This method consists of simulating a PXRD patterns (including intensities) from a structural model, then adjust the parameters of this model so

that the simulated PXRD patterns match the experimental one as much as possible. In comparison to the Le Bail method, it requires a-prior knowledge of the type and position of atoms in the unit cell (which are refined). In this thesis, Le Bail and Rietveld refinements were performed using the JANA2006 program**.**

To construct the calculated diffractogram, the intensity of the i^{th} point are calculated by summing the contributions of Bragg's reflection with the background such as:

$$y_{ci} = y_{bi} + \sum_{\Phi=1}^{N} S_{\Phi} \sum_{k=1}^{k} Mp_{\Phi k}.Lp_{\Phi k}.|F_{hkl}|^2.PSF_{\Phi k} \quad \text{Equation 1}$$

Where:

y_{bi} is the background intensity.

S_{Φ} is a scale factor of the Φ phase,

$M_{\Phi k}$ is the multiplicity of the k^{th} reflection of the Φ phase,

$Lp_{\Phi k}$ contains Lorentz, polarization, multiplicity factors,

$P_{\Phi k}$ is the orientation function,

$|F_{hkl}|$ is the structure factor

$PSF_{\Phi k}$ is the profil function of the k^{th} reflection of the Φ phase

Φ = 1 : single phase, and if Φ>1 : multi phase

The convergence of the refinements is followed by the least squares method with the minimization of a cost function representing the sum of the differences between observed points $y_{i, obs}$ and calculated points $y_{i, cal}$:

$$\mathbf{S} = \sum_{\mathbf{i=1}}^{\mathbf{n}} \mathbf{w_i}.\left[\mathbf{y_{i,obs}} - \mathbf{y_{i,cal}}\right] \quad \text{Equation 2}$$

Where: w_i is a weighting factor generally defined as $wi = 1/\sigma_i$; with σ_i the standard deviation on $y_{i,obs}$

The relevance of structural refinements is verified by the factors of agreement

- Bragg factor :

$$R_p = \frac{\sum_k |I_{k,obs} - I_{k,cal}|}{\sum_k I_{k,obs}} \quad \text{Equation 3}$$

Where: $I_{k,obs}$, $I_{k,cal}$ are the intensited intensity measured and calculated for the k reflexion

- Structure factor observed :

$$R_{obs} = \frac{\sum_k |F_{k,obs} - F_{k,cal}|}{\sum_k F_{k,obs}} \quad \text{and, } wR_{obs} = \frac{\sum_k w_k |F_{k,obs} - F_{k,cal}|}{\sum_k w_k F_{k,obs}} \qquad \text{Equation 4}$$

Specific factors of the Le Bail and the Rietveld method attest of the goodness of fitting of the observed profile and the profile calculated on the entire diagram (Bragg peaks and background)

$$R_{exp} = \left[\frac{N - P + C}{\sum w_i y_i^2}\right]^{1/2} \qquad \text{Equation 5}$$

Where: N is the number of points in the diffractogram, P is the number of refined parameters and C, is the number of applied constraints

- The profile factor R_p and the weighted profile factor wR_p

$$R_p = \frac{\sum_i |y_i - y_{ic}|}{\sum_k y_i} \quad \text{and, } R_{wp} = \left[\frac{\sum_i w_i |y_i - y_{ic}|^2}{\sum_k w_i y_i^2}\right]^{1/2} \qquad \text{Equation 6}$$

Where: y_i et y_{ic} are the observed and the calculated intensities at 2Θ ; y_{if} is the intensity of the background at 2Θ and w_i is the weighting of every intensity y_i.

- A statistical criterion is also defined:

$$GoF = \frac{R_{wp}}{R_{exp}} \text{ or } \chi^2 = \left[\frac{R_{wp}}{R_{exp}}\right]^2 \qquad \text{Equation 7}$$

For a Rietveld refinement from powder data, when the Bragg factor is less than 10%, it can be considered that the proposed structural model is likely correct (if the inter-atomic distances and atomic displacement parameters are consistent). The good agreement between the observed and calculated diagrams given by the R_p and wR_p factors are also indicators to be considered.

Some general comments on the applicability of Rietveld analyses for the sample investigated in this thesis shall be made. In the case of zeolites, the scattering power of Al^{3+} and Si^{4+} cations is too close to be differentiated. In the case of template-free zeolites, several extra framework cations are present such as Cs^+. These extra framework cations strongly impact the diffracted intensities to the point that using a starting model considering only the framework cations might not be sufficient. The occupancies of extra framework cations were sometimes fixed based on the compositions obtained by ICP and EDS measurements (see below) in order to reduce variables in the Rietveld refinements. In the case of nanosized

zeolites, the Rietveld refinements are further complicated by an enlargement due to the reduced size of the crystallites.

3. CO_2 adsorption in nanosized zeolites studied by in situ PXRD

Zeolite samples were activated at 350 °C for 2 h in order to desorb the water. Then the powder zeolite samples were measured using a *PANalytical* X'Pert Pro diffractometer with CuKα monochromatized radiation (λ=1.5418 Å). The samples were scanned in the range 5-110° 2θ with a step size of 0.02° (Figure 16). Prior to CO_2 adsorption measurements, all samples were again activated in situ at 350 °C for 2 h; (10 K/min) to 623K. Then the samples were measured at 350 °C under CO_2 flow (1bar) with decreasing the temperature until room temperature (Figure 15).

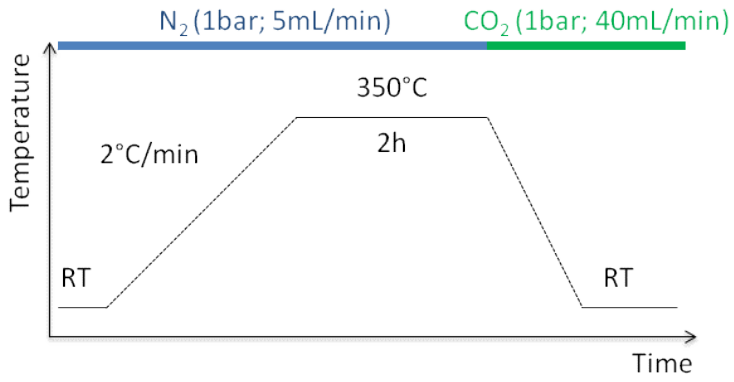

Figure 15: In situ activation procedure of zeolite samples prior to CO_2 adsorption.

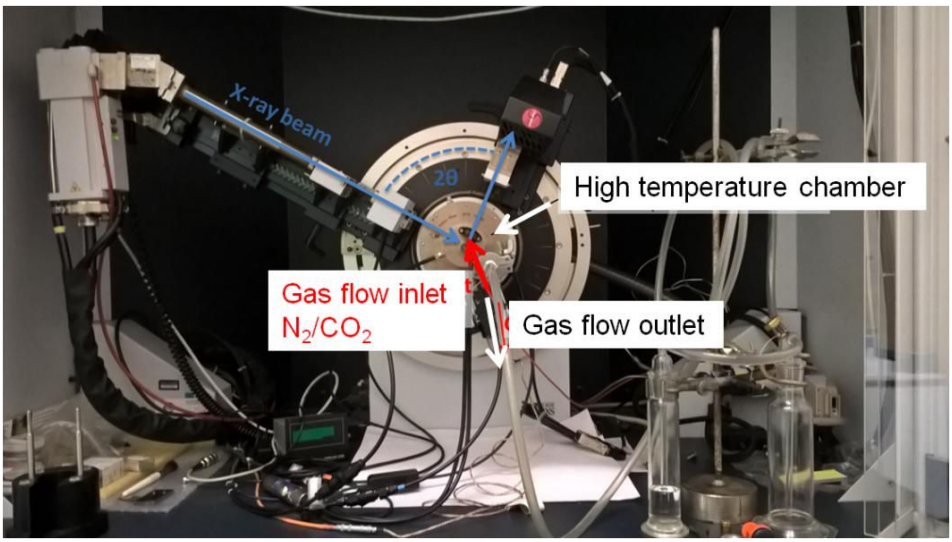

Figure 16: Set up used for in-situPXRD study of zeolite samples under CO_2 adsorption.

B. Gas physisorption measurements

The gas adsorption is one of the most powerful and widely applied methods to study physical adsorption and textural characteristics of porous materials. This technique delivers information about surface area, pore volumes and sizes of porous materials. The fundamentals of this method are based on the adsorption of inert gases (N_2, Ar and CO_2) at constant cryogenic temperatures over a range of pressures. Physisorption occurs when the adsorbate gas (adsorptive) interact with the surface of a solid (adsorbent). During such process chemical bonds are not broken or formed as only van der Waals forces are involved.

4. N_2 adsorption study

Commonly, nitrogen adsorption at -196 °C has been employed for the micropore size analysis of zeolites. However, it is becoming clear that nitrogen is not an ideal adsorptive for microporosity evaluation, due to the presence of quadruple moment, which influences the micropore filling. Therefore, Ar at -186 °C should be used as a preferred gas for micropore characterization of zeolites, but argon's extremely high price suppress its utilization and for that reason nitrogen is still largely employed. The physisorption begins with sample outgassing to remove physically adsorbed molecules from the material surface (mostly water), followed by gradual increase of adsorptive pressure and finishing with pressure decrease. The results are expressed in the form of adsorption/desorption isotherms, where the quantity of adsorbed gas is presented as a function of the relative pressure. The isotherms of different shapes are used to determine valuable parameters, namely, surface area and pore structure.

The Figure 17 shows the different type of isotherm profiles[94]. The type I(a) and I(b) isotherms are characteristic for microporous materials with pore width below 0.7 nm and in the range 0.7–2 nm, respectively. Type II isotherms are found in non-porous or macroporous materials, govern by mono-and then multi-layer surface adsorption. Point B usually indicates the completion of the monolayer coverage. Type III isotherm is also typical for nonporous or macroporous solids, but in this case the lack of point B indicates very weak adsorbent adsorbate interactions. The adsorbed species are gathered around the most favorable site on the adsorbent surface. Unlike to Type II isotherm, the amount adsorbed is restricted at p/p_0. Type IV(a) and IV(b) isotherms are representative for mesoporous materials, where the difference between them is associated with the size of mesopores. Regarding type IV(a) isotherm the hysteresis begins to appear for pores wider than ~4 nm, whereas in case of type IV(b) isotherm the absence of hysteresis loop indicates completely reversible process characteristic for mesopores of smaller width. Additionally, type IV(b) isotherms appear when

the analysis is performed on conical and cylindrical mesopores that are closed at the tapered end. The shape of type V isotherm is comparable to type III at low P/P_0, indicating weak adsorbent-adsorbate interactions. However, with increasing relative pressure the pore filling process begins, which is usually seen in case of water adsorption on hydrophobic microporous and mesoporous solids. Type VI isotherm represents typical layer-by–layer adsorption on non-porous surface.

In order to calculate the specific surface area of zeolite, the Brunauer-Emmett-Teller (BET) method is applied. Despite its imperfection related to theoretical assumptions, this technique continues to be widely used.

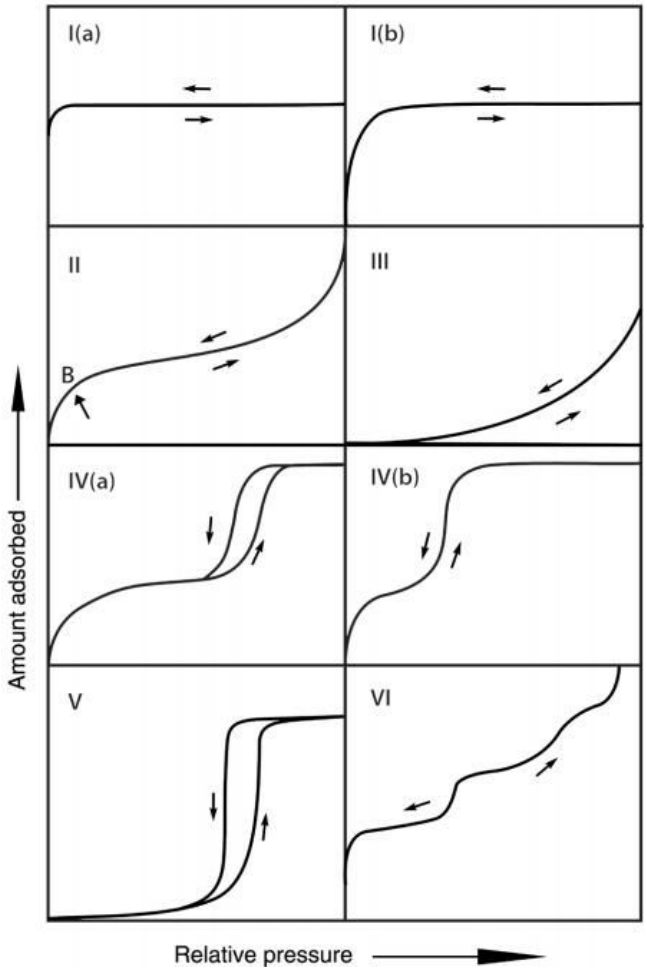

Figure 17: IUPAC classification of physisorption isotherms.

Nitrogen adsorption/desorption isotherms in this thesis were measured using Micrometrics ASAP 2020 volumetric adsorption analyser. About 0.100 g of sample was degassed at 350 °C under vacuum overnight prior to the measurement. The external surface area (S_{ext} / m^2g^{-1}) and micropores volume (V_{micro} / cm^3g^{-1}) were estimated by Dubinin-Radushkevich.

$$\frac{W}{W_0} = e^{-BT\,ln\left(\frac{p^\circ}{p}\right)}$$ Equation 8

$$\log W = \log(W_0) - k\left[\log\left(\frac{p^\circ}{p}\right)\right]^2$$ Equation 9

Where W is the volume of the pores that has been filled at p/p° (cm^3/g); W_0 is the micropore volume; k and B are constants;

5. CO_2 adsorption study

Model: Several models are used to model the adsorption of CO_2 onto zeolites but the two most known are the *Langmuir (Eq 9)* and the *Toth* isotherm (Eq 10) model.

$$q_i = \frac{q_{sat,i}.b_i.P}{1+b_i.P}$$ Equation 10

$$q = \frac{q_{sat}.b.P}{(1+(b.P)^t)^{1/t}}$$ Equation 11

These two models are not sufficient to describe the adsorption isotherms in the range of pressure we used. Therefore, the *Dual site Langmuir* (DSL) is used to describe the CO_2 adsorption in aluminosilicates (zeolites).

The *Dual-site Langmuir* parameters for adsorption of CO_2 were obtained by fitting the Langmuir model defined by the following equation and the CO_2 isotherm adsorption. The adsorption data for CO_2 in CHA zeolite at 0 °C were fitted with the Dual-site Langmuir model[95,96]:

$$q_{total} = q_A + q_B = \frac{q_{sat,A}.b_A.P}{1+b_A.P} + \frac{q_{sat,B}.b_B.P}{1+b_B.P}$$ Equation 12

Where $q_{sat.A}$ ($mmol.g^{-1}$) and $q_{sat.B}$ ($mmol.g^{-1}$) are the saturation quantity adsorbed on the site with respective equilibrium constant b_A (Pa^{-1}) and b_B (Pa^{-1}) at pressure P (Pa).

$$b_i = \frac{k_i^\circ}{k_{-i}^\circ}.e^{-\frac{\Delta H_i}{RT}}$$ Equation 13

$$\ln(b_i) = \ln\left(\frac{k_i^\circ}{k_{-i}^\circ}\right) + -\frac{\Delta H_i}{RT}$$ Equation 14

This method was used to describe the CO_2 adsorption in zeolites over the entire pressure range.

Selectivity: Henry's constant is directly related to the interaction of adsorbate/adsorbent. In order to evaluate adsorption characteristics between adsorbent and adsorbate, Henry's constant was determined by using the Henry equation:

$$P = \frac{q}{K_H} . e^{(A1.q + A2.q^2 + \dots)} \qquad \text{Equation 15}$$

Where A_1, A_2 are the variable coefficients and q is the loading amount ($mmol.g^{-1}$). And K_H the Henry constant ($mmol \cdot g^{-1} \cdot bar^{-1}$)

A plot of ln(P/q) in function of the adsorbed amount q, should approach the axis linearly as $\lim_{q \to 0}$ with the intercept $-\ln(K_H)$.

The selectivity is defined by the following equation by comparison of the Henry's constant of 2 different compounds. (Example with the selectivity of CO_2/CH_4):

$$\alpha\,(CO_2/CH_4) = \frac{K_{H,CO_2}}{K_{H,CH_4}} \quad \text{and,} \quad \alpha\,(CO_2/N_2) = \frac{K_{H,CO_2}}{K_{H,N_2}} \qquad \text{Equation 16}$$

Where : $\alpha(CO_2/CH_4)$ is the selectivity CO_2 toward CH_4, $\alpha(CO_2/N_2)$ is the selectivity CO_2 toward N_2 and K_{Hi} is the Henry constant of the i compound.

C. Thermal analysis (TG)

Thermal analysis method is employed to determine the physio-chemical changes of zeolites at elevated temperatures. The main properties of a catalyst that could be analysed by this technique are stability, decomposition of organic molecules, and dehydration. There are two different types of thermal analysis; (i) thermogravimetric analysis (TGA), which evaluates the change of sample weight as a function of temperature/time, and (ii) differential thermal analysis (DTA) that correlates the difference in temperature between the sample and inert reference material. Hence, the physico-chemical transformations of the sample are temperature dependent they are usually supplemented with the liberation or absorption of heat, which corresponds to exo-and endothermic reactions respectively. Therefore, if the difference in temperatures (sample from the reference) is plotted against time, exo-and endothermic curves can be linked to particular reactions occurring at specific time and temperature.

TGA/DTA measurements of different zeolite samples were carried out on a SETSYS 1750 CS evolution instrument (SETARAM). Prior measurement, the samples were placed in a

desiccator at around 70% humidity and stored overnight. About 15-20 mg of each sample was introduced in an alumina crucible that was loaded in the analyser chamber. The sample was heated from 30 °C to 800 °C with a heating ramp of 5 °C/min under air (flow rate: 40 mL/min).

CO_2 and CH_4 adsorption study

After activation (water desorption) at 350 °C for 2 hours under nitrogen flow (5 mL/min), the zeolite samples were placed at room temperature under a continuous flow of CO_2 (flow rate: 40 mL/min, 1 bar) for 9 hours. The quantity of CO_2 or CH_4 absorbed was determined using the mass increase compared to the total mass of the sample. Regarding the CH_4, the flow started at room temperature.

Cycles of CO_2 adsorption/desorption were conducted and monitored by TGA. An alternance between activation at 350 °C for 2 hours under N_2 flow (flow rate: 40 mL/min) and CO_2 adsorption at room temperature (flow rate: 40 mL/min, 1 bar) for 2 hours has been performed 10 consecutive times.

Multi cycle ad/desorption was performed with a TGA-DSC 1500. The sample (26.91 g) was dehydrated at 350 °C for 1h (ramp: 5 °C/min). The CO_2 flow (40 mL/min) was injected during the temperature decreasing (20 °C/min). The temperature was maintained at 35 °C for 50 min under CO_2 flow. Then, the sample was activated at 350 °C for 1h (ramp: 5 °C/min) the procedure was repeated 9 more times.

D. Electron microscopy

1. Scanning electron microscopy (SEM)

Scanning electron microscopy (SEM) uses a high-energy beam of electrons ejected from a filament, accelerated by a voltage (typically 30kV or below) and focused into a small probe that is scanned over the surface of the sample. SEM images are usually generated as a result of transformed signals of secondary electrons (SE) or backscattered electrons (BSE). SE images are formed from low energy electrons ejected from the surface of the sample and can provide high depth of field images with topographical information. BSE images are formed from electrons with a higher energy coming from below the surface and provide images with both chemical (Z-contrast) and crystallographic orientation informations. The resolution of modern SEMs is of the order of few nanometers. In this thesis, mostly SE images where used to examine the morphology, particle size and homogeneity of our zeolite samples

The SEM characterizations were performed on small amounts of dried sample in powder form. They were mounted on a specimen holder using double stick carbon tapes. To improve the electrical conductivity of the sample, they were coated with platinum using CRESSINGTON 108 auto evaporative coating machine. SEM micrographs were recorded with TESCAN Mira field-emission scanning electron microscope operating at 30 kV.

2. Transmission electron microscopy (TEM)

Transmission electron microscopy (TEM) uses high speed accelerated electrons (typically between 80 to 300 kV) to produce images based on the detection of electrons (transmitted and scattered) that have passed through a very thin sample. A set of magnetic lenses associated with diaphragms, called the condenser system, makes it possible to modify the illumination mode of the sample (parallel or convergent beam). TEM has a higher resolution (about 0.1 nanometer) than the SEM. In parallel beam illumination, such high resolution images can be obtained from the interference of transmitted and diffracted beams. The image has all the properties of periodicity and crystalline symmetries present in the diffraction pattern. High resolution TEM (HRTEM) images allow to access information on the atomic scale including porosity, interatomic distances and atoms arrangement in the sample. It can also be used to identify structural defects, such as dislocations and stacking faults. Besides image mode, TEM can also be used to perform electron diffraction experiments (see below).

The TEM high resolution imaging were performed using a FEI Tecnaï G2 (LaB_6 – 300 kV) or a JEOL ARM-200F (Field Emission Gun – 200 kV) microscope. The zeolite samples were dispersed in ethanol (99.9%) and then a drop of solution was deposited on a TEM copper grid covered by a holey carbon membrane.

3. Energy Dispersive Spectroscopy (EDS)

Energy Dispersive Spectroscopy (EDS) is a technique coupled to an electron microscope (SEM or TEM). It allows a qualitative and semi-quantitative analysis of the chemical elements constituting a material. EDS analyses were performed on a JEOL 2010 (LaB6- 200 kV) transmission electron microscope.

Upon interaction of the incident electron beam with the sample, the incident electron can ionize an atom by expelling an electron from an inner layer. A hole on this inner layer is formed. An electron of an upper layer of the element will fill this hole, and this electronic de-excitation is accompanied by an emission of X-rays whose energy is characteristic of the ionized atom. A spectrum is obtained showing the intensity of the radiation emitted as a

function of the energy, in the form of peaks. The emitted X-rays being specific to each element, a qualitative analysis is possible thanks to the position of the peaks. Moreover, the ratio of the intensities of the emitted X-rays being proportional to the ratio of the mass concentrations of the chemical elements present in the sample, a semi-quantitative analysis can be carried out.

The obtained values depend on several parameters such as the atomic number, matrix effects, absorption or fluorescence. This is why it is necessary to make corrections to the values obtained by comparing with a standard of known composition. In this thesis, a particular attention has been paid to obtain a chemical composition of our samples as reliable as possible by using various zeolites as reference samples.

E. Local structure of zeolites by solid-state nuclear magnetic resonance (NMR)

Solid-state Nuclear Magnetic Resonance, also known as solid-state NMR, is a spectroscopic technique, which can provide qualitative and quantitative information on the zeolite solid-state NMR is often seen as a complementary technique to XRD. While XRD provides long-range information, NMR focuses on short-range environment. Liquid NMR is a technique that is very commonly applied for liquids and gasses. However, different from liquids and gasses, the absence of fast thermal/molecular motions of the nuclei in a solid results in peaks broadening. The influence of anisotropic internal magnetic interaction on the line width is not averaged to zero by thermal motions for solids. This anisotropy can be reduced by applying magic angle spinning (MAS). During MAS the sample is spun around an angle of 54.74° to the axis of the external magnetic field. At this angle the maximal line narrowing effect is achieved. Magic angle spinning can be seen as the man-made analogy of molecular motions in liquids resulting in peak narrowing. The information, which can be obtained from an NMR experiment, depends on the identity of the nuclei that is studied. Next, the main nuclei in zeolite catalysts will be briefly described.

1. ^{27}Al NMR spectroscopy (I = 5/2, natural abundance 100.0%)

As stated by Lowenstein's rule, an aluminum atom is always connected to four silicon atoms. As a result ^{27}Al tetrahedral signals will usually be found in a relatively small shift range (50 - 60 ppm). However, aluminum can also be present as extra framework atoms, which can be found around 0 ppm. Hence, the technique can be used to distinguish between tetrahedral framework aluminum atoms and extra framework aluminum atoms. ^{27}Al is a quadrupolar nucleus (I = 5/2). Quadrupolar nuclei will interact not only with the external magnetic field but also with the electric field gradient. These quadrupolar interactions cause broadening of the

signals that cannot be removed using just magic angle spinning. However by applying certain NMR techniques the information can still be obtained. Due to second-order quadrupolar interactions aluminum atoms depend on their local chemical environment. This interaction can provide useful structural information such as the aluminum distribution within the zeolite framework. When dehydrated samples are studied, the sensitivity for the local environment results in very broad and often overlapping resonances. Therefore, samples are usually hydrated by leaving them overnight in a desiccator holding a moisturizing agent.

2. ^{29}Si NMR spectroscopy (I = 1/2, natural abundancy 4.7%)

In a zeolite each silicon atom is connected via an oxygen atom to four atoms. These can be silicon or aluminum atoms, resulting in five different species. Depending on the connected atoms, the chemical environment for the silicon atom will differ. This can be seen in the ^{29}Si NMR spectra as different chemical shift ranges. With increasing the neighboring aluminum atoms, the electron deficiency increases, resulting in a more deshielded silicon atom and thus a higher chemical shift. In a zeolite consisting of only equivalent T-sites maximum five different chemical environments can be found, each in a well-defined range. In this case, the NMR spectra only contain information on the framework composition. In a less homogeneous zeolite, the number of signals present and their intensities will provide information on the number and the relative population of the non-equivalent crystallographic sites. Using the following equation, the intensities of the ^{29}Si signals can be used to calculate the silicon/aluminum ratio:

$$\frac{n_{Si}}{n_{Al}} = \frac{\sum_{n=0}^{4} I_{Si(nAl)}}{\sum_{n=0}^{4} 0.25*n*I_{Si(nAl)}} \qquad \text{Equation 17}$$

The chemical shift can provide information on the bond angle, the bond distance and the nature of the neighbor.

F. Electron Diffraction

The most common technique for structure determination of crystalline materials is single crystal X-ray diffraction (SCXRD), which can only be used for crystals larger than ~10 µm with in-house diffractometers or a few microns with synchrotron light sources. In this work related to the synthesis of nanosized zeolites, only PXRD can be used due to the lack of suitable single crystals. While effective, PXRD suffers from certain drawbacks notably when dealing with nanosized particles. The particle size reduction produces a broadening of the diffracted peaks which usually complicate their deconvolution and the subsequent structural

analysis. Under such a circumstance, electron diffraction appears as a good alternative to X-ray diffraction. Owing to the strong electron/matter interactions, electron diffraction experiments can be performed using a TEM on single crystals with size below 50 nm.

In X-ray crystallography, the kinematic approximation allows to consider a proportionality relationship between the diffracted intensities I(hkl) and the structure factor F(hkl) which contains the information about the position of atoms in the unit cell. Using structural resolution programs developed for X-ray diffraction, it is possible to exploit electron diffraction data for structural analyses in a way similar to X-ray diffraction. Only the scattering factors should be adapted for electron diffraction. Like for X-ray, electron scattering factors does have a dependence to the atomic number but there are differences due to the fact that X-rays probe the electron density while electrons probe the electrostatic potential in the crystal. This picture would be perfect if the kinematical approximation is known to be no longer valid in the following two cases:

- in X-ray diffraction on very large perfect crystals (monochromator crystals).

- in electron diffraction whatever the crystal.

The strong electron/matter interactions allow analyzing tiny crystals but leads to multiple diffraction events which invalidate the kinematical approximation. The main effect of multiple diffraction on electron diffraction patterns is a seemingly uniform distribution of the diffracted intensities because each reflection is associated, not to only one, but several diffraction events. This blurs the information with notably a loss of the ranking between reflections (high, medium or low intensity) which is of importance for an accurate structure analysis.

Despite this strong drawback, electron crystallography has grown very fast this last ten years (notably in the zeolite community) due to the introduction of approaches aiming to limit these multiple diffraction events[97]. Thanks to these approaches (see the ones used during this work below), the kinematic theory of diffraction is good enough to obtain a structural model (structure solution) of an unknown structure using programs already developed for X-ray diffraction. Nevertheless it fails to achieve accurate structure refinements and, to account for multiple scattering events, the dynamical theory of diffraction should be used. It actually complicates the data analysis[98,99] but allows to obtain results approaching the accuracy of SCXRD[100].

3. *Precession Electron Diffraction (PED)*

Precession electron diffraction (PED)[101] is a technique used to reduce the multiple diffractions events ("dynamic effects") present in the diffracted intensities. The PED collects the electron diffraction patterns of a sample in a TEM with the electron beam (parallel illumination) performing a precession motion at the surface of a cone with the vertex at the sample. This precession movement is achieved using the microscope's deflectors. First, above the sample, the incident electron beam is tilted and rotated around the optical axis of the microscope (SCAN). This forms a cone of half-angle α (precession angle) whose axis is the optical axis of the microscope and the vertex is the object (Figure 18). Below the sample, the electron beam is tilted back to the microscope axis (DESCAN) in order to obtain a spot patterns. The difference with conventional parallel beam diffraction techniques such as selected area electron diffraction (SAED) or nanobeam electron diffraction (NBED) is that the PED patterns is the summation of all the diffraction patterns collected during the rotation θ (2π or more) of the beam. The PED has thus the advantage to collect integrated electron diffraction data and, with this technique, the kinematical approximation is a good hypothesis to analyze quantitatively the intensities and use structure solution methods.

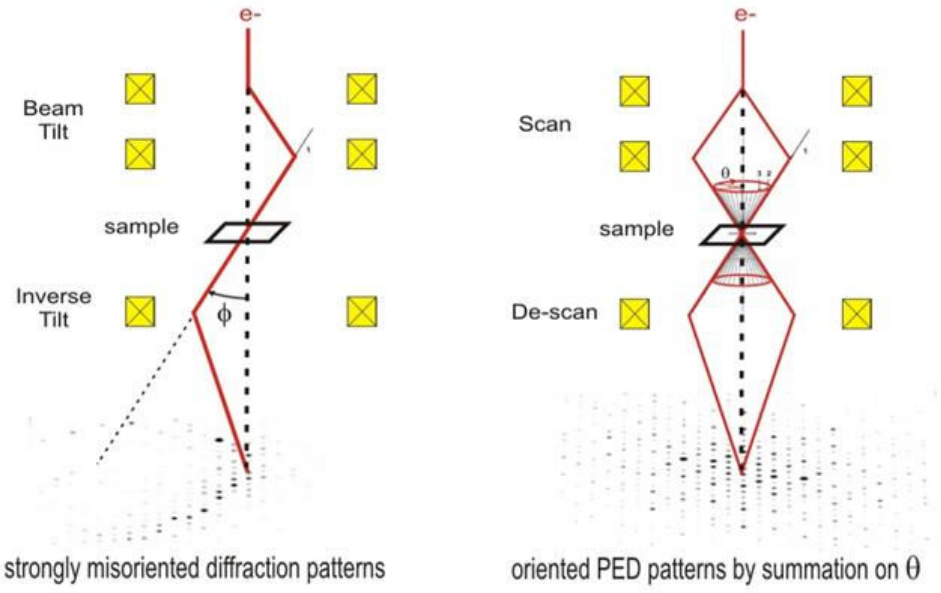

Figure 18: Schematic representation of the electron beam motion in PED.

Among the advantages of the PED we can mention:

- **Quasi-kinematical diffraction patterns:** The hierarchy of measured intensities (high, medium and low) is close to that expected in kinematic conditions.

- **Broader range of measured reflections:** During the precession movement, the Laue circle extends farther into reciprocal space allowing to collect more reflections at high scattering angles.
- **Low sensitivity to local thickness and orientation variations**: PED intensities are less sensitive to thickness variations and crystal bending.

4. Precession Electron Diffraction Tomography (PEDT)

Electron diffraction tomography (EDT) or automated diffraction tomography (ADT) is a powerful method for the structure determination of unknown materials. EDT follows the principle of the rotating crystal method used in SCXRD. A series of diffraction patterns are sequentially recorded from a single crystal while tilting the crystal over the largest angular range possible by rotating the TEM goniometer with a constant step (Δx). The intensities from each electron diffraction patterns are extracted and combined in order to reconstruct a three-dimensional (3D) collection of reflections *hkl* with their intensities *I* and estimated error $\sigma(I)$. This technique proposed in 2007 by the group of Ute Kolb (Germany) offers two advantages:

- diminish the dynamic effects by recording non oriented off-axis patterns.

- acquire a maximum number of patterns to improve the completeness of the dataset.

Nonetheless, the geometry of the TEM does not allow a continuous rotation of the crystal and thus an EDT experiment does not allow reconstructing the entire reciprocal space in 3D. The maximum angular range (about 110° for dedicated instruments) is dependent on both the microscope and the sample holder. One single EDT experiment can be sufficient depending on the symmetry of the crystal under investigation. If not enough, a convenient way to increase the data completeness is to combine data sets from different crystals.

EDT data acquisition approach can be combined with the use of PED[102] resulting in the so-called precession electron diffraction tomography technique (PEDT)[103]. For structural resolution and fine structure characterization of our CHA sample, we used PEDT on isolated single zeolite crystal. The PEDT intensities extraction and data reduction were performed using the program PETS and PETS 2.0[104]. The program Superflip[105] was used for the structure solution. The program JANA 2006[106] was used for the structure refinement (in both kinematical and dynamical cases).

5. CO_2 absorbed in CHA zeolite: PEDT experiments

In the earlier stage of the work PEDT experiments on CHA were performed at CRISMAT, Caen using a liquid nitrogen cooling holder to limit the degradation of the sample under the electron beam. At some point we realized that once the as-prepared (i.e. hydrated) CHA samples were introduced in the TEM, the water was almost immediately removed resulting in the analysis of dehydrated CHA samples. Since the ultimate aim was to characterize host/guest interactions of CO_2 absorbed and CHA, we went to the Institute of Physics of the Czech Academy of Sciences in Prague to perform the PEDT experiments (collaboration with Lukas Palatinus). There, a cryotransfer holder was used to freeze the sample to liquid nitrogen temperature before introduction in the TEM in order to prevent the released of the CO_2 under the TEM high vacuum. The experiment was conducted on a Philips CM120 TEM with an LaB6 cathode operated at 120 kV. The precession movement of the electron beam was controlled with a Digistar precession unit (Nanomegas). Images and diffraction patterns were recorded with a CCD camera (Olympus SIS Veleta, 2048 x 2048 pixels, 14 bit depth). For the CO_2-absorbed CHA sample, a significant weakening of the diffracted intensities was observed after several minutes of data collection slightly limiting the number of available PEDT patterns per crystals. To overcome this, several PEDT data sets were combined in order to achieve a sufficient resolution. A great attention has been paid to record and combine PEDT data sets for crystals presenting as little defects as possible. Another interest to work at low temperature (-196 °C) is to limit the mobility of the cations inside the CHA framework notably for highly mobile Na^+ cations.

The Table 6 shows how the three techniques are complementary study structures that cannot be solved by either method alone.

Table 6: Overview of structural resolution methods. [107]

	PXRD	HRTEM	ED	
	One-dimensional	Two-dimensional	Two-dimensional	Three-dimensional
Crystal size	>50 nm	>5 nm	>50 nm	>50 nm
Unit-cell determination	Difficult	Requires expertise	Requires expertise	Easy
Symmetry determination	Difficult	Easy	Requires expertise	Easy
Peak overlap	Yes	No	No	No
Data completeness	High	Low	Low	High

	PXRD	HRTEM	ED	
	One-dimensional	Two-dimensional	Two-dimensional	Three-dimensional
Intensities	Kinematic	Affected by objective lens	Dynamic	Dynamic
Structure factor phase information	No	Yes	No	No
Data collection	Easy	Requires expertise	Requires expertise	Easy
Structure determination	Difficult	Requires expertise	Difficult	Easy
Sample information	Representative	Individual	Individual	Individual

G. Inductively coupled plasma-atomic emission (ICP) spectroscopy

Inductively coupled plasma atomic emission spectroscopy (ICP-AES) is considered as the most precise method for quantitative chemical analysis of materials. This technique can inspect up to 50 elements simultaneously and thanks to its sensitivity it can detect trace levels of components. The sample introduced into spectrometer is atomized with argon into hot plasma, which ensures electron excitation of elements. The excited sample emits light wavelengths characteristic for each element in the ultraviolet or visible region. Further, spectrometer disperses the emitted light and separates the particular element emissions. The intensity of emitted light is directly proportional to the concentration of each element in the analysed sample. Special software is used in order to transform the electronic signal into concentrations.

The elemental analysis of all samples was performed by inductively coupled plasma–atomic emission spectroscopy using an OPTIMA 4300 DV (Perkin–Elmer) instrument. The procedure for preparation of samples for ICP is as follows: (i) 50 mg of sample was dissolved in 3 ml of hydrofluoric acid (HF) (Sigma Aldrich 40-45%), (ii) 0.5 ml of mixture (HNO_3: HCl ≡ 1:3 v/v) was added and heated at 100 °C for 1 h in polytetrafluoroethylene (PTFE) bottle, and finally (iii) 10 ml of double deionized water (dd H_2O) and 1.4 g of boric acid (H_3BO_3) were added. The resulted solution was transferred to PTFE volumetric flask (100 mL), diluted with ddH_2O up to 100 ml mark and homogenised by shaking.

H. Fourier transformed infrared spectroscopy (FTIR)

Fourier transformed infrared spectroscopy (FTIR) is a well-known characterization tool for zeolite structure investigation as well as identification of adsorbed species.[108] This method studies the transitions between vibrational levels due to absorption of molecules at specific frequencies (v). The distinct absorption frequency is influenced by the mass of atoms in the molecule and the bond strength. The vibrational frequencies increase with increasing bond strength and with decreasing mass of the vibrating atoms. In fact, not all the vibrations are infrared active due to the lack of change in the dipole moment.

There are different types of infrared spectroscopy, such as diffuse reflectance (DRIFT), transmission and attenuated total reflectance (ATR). The choice of appropriate method relays on the type of material analyzed and desired structural information. In case of zeolites, the transmission infrared spectroscopy mode is usually applied. For the purpose of measurement, the sample has to be pressed into self–supporting homogeneous wafers of about 20 mg. IR enables to obtain quantitative information about the sample when the Lambert-Beer law is applied, however for zeolites the determination of molar extinction coefficient is of significant importance.

This technique also permits to acquire information about zeolite acidity and adsorption capacity. The choice of probe molecule is of great importance, since depending on the properties of the probe, diverse particularities about zeolite structure can be obtained. For the purpose of this study different, gases (CO_2, O_2, and NO) were selected as probe molecules, to assess the adsorption capacity of modified zeolites.

The IR spectra of prepared porous materials were recorded on a Nicolet Impact 410 FTIR spectrometer equipped with a MCT detector in the range 400-4000 cm^{-1}. The adsorption CO_2 on 20 mg of self-supported pellets as-prepared CHA was followed using *in-situ* FTIR spectroscopy. The cell was connected to a 10^{-5} Pa high-vacuum. The sample was activated at 350 °C for 2 h to remove the adsorbed water. After cooling to room temperature, a spectrum of the samples before adsorption was recorded for further use as a reference. The IR spectra of CO_2 and CH_4 probe molecules were collected at room temperature; the gas injection was done in small doses for CO_2 and equilibrium for CH_4. The OMNIC version 7.3 SP1 program was used for data processing.

CHAPTER 3: NEW SYNTHESIS ROUTES OF NANOSIZED CHA-TYPE ZEOLITES

The objective of this work is to develop a new synthesis strategy for CHA nanosized zeolite; the target size of the CHA crystals is below 100 nm. The CHA zeolite was selected due to the promising performance in gas separation especially for CO_2 from CH_4.

We have seen that even though many studies deal with the topic "Trapdoor effect" only DFT studies tend to prove movement of the door keeping cation. Coudert's theoretical study[90] opens the door to a new discussion on the phenomenon and its true nature: is the Cs/K displaced because of its interaction with CO_2 or is it in constant motion, vibrating and oscillating to leave only the space necessary for a molecule of CO_2 to lodge in the cage? This is a question that we will try to answer in the second part of this chapter.

A. Synthesis of nanosized CHA from FAU by recrystallization

The first phase of the study aims to reproduce the synthesis of CHA using commercial FAU CBV400 and CBV720 as initial material. This study will provide reference materials and set objectives

In the application of zeolites, mass transfer and diffusion of molecules on the zeolite are very important and size of both zeolite crystal and pores have an effect on the utilization of the zeolite. Higher utilization of the zeolite can be accomplished by a modification of the microporosity or by reducing the size and so the diffusion path length for molecules[109]

To remind, Chabazite zeolite can be synthesized using organic structure directing agents (OSDAs) which are typically costly and require calcination of the zeolite to remove the organic template (Chapter 1). Another way to obtain the CHA zeolite is through interzeolite transformation where only inorganic structure directing agents are used. CHA obtained by an interzeolite transformation of faujasite (FAU) has been used for many investigations, however, only limited research has been dedicated on the effect of the starting material on the size and morphology of the CHA crystal. The starting material commonly used is the CBV400 and provides CHA with a Si/Al=1.9 (ICP in w/w); the average size of the crystals is 1 µm.[59]

Here, interzeolite transformation of commercial FAU zeolite CBV720 with an initial Si/Al ratio of 13 (ICP in w/w) to r2.3-CHA (IT = interzeolite transformation) was done at 95 °C after 7

days under treatment with KOH solution (Si/K/H_2O ratio of 1/1/30). The X-ray powder diffraction pattern (XRPD) for CBV720 and r2.3-CHA(IT) are shown in Figure 19. Two minor impurity peaks are also present in the diffraction pattern for r2.3-CHA(IT) marked with grey circles (Figure 19b). The interzeolite transformation of CBV720 with the used synthesis composition results in the CHA with a Si/Al ratio of 2.3 (ICP). During this interzeolite transformation, only part of the Si is converted into the CHA product from the starting FAU. As evidenced, a higher Si ratio in the starting material results in a higher Si content in the product.

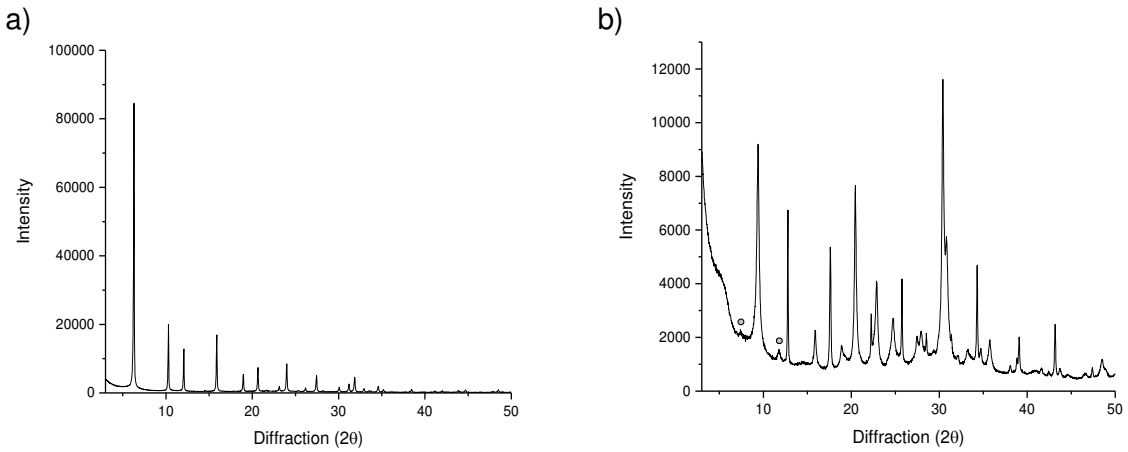

Figure 19: (a) XRPD patterns of CBV720 (Commercial FAU) and (b) r2.3-CHA(IT). The circles correspond to impurities.

It has been suggested that interzeolite transformation proceeds through a dissolution of the zeolite crystal which are used to construct the new zeolite.

SEM pictures of the CBV720 (Figure 20a) shows that it consists of zeolite crystals of various sizes (200-1000 nm) with a rough surface. The r2.3-CHA(IT) crystals have a different appearance. The zeolite consists of agglomerates (~500 nm) of smaller zeolite crystals of 50-100 nm (Figure 20b). It is speculated that the mesopores in the CBV720 could facilitate dissolution of the crystal into smaller crystals which would result in the formation of smaller CHA zeolite crystals.

The porosity of r2.3-CHA(IT) was assessed by nitrogen physisorption, which shows that the obtained r2.3-CHA(IT) possesses both micro- and mesoporosity from the uptake at low pressure (<0.01 P/P°) and from the hysteresis loop at higher partial pressure (Figure 21a). The r2.3-CHA(IT) exhibits a high surface area of 249 m^2/g compared to other CHA zeolites obtained from the interzeolite conversion using K^+ as structure directing agent. The total pore volume of 0.39 cm^3/g has only a limited contribution from the micropores with 0.05 cm^3/g.

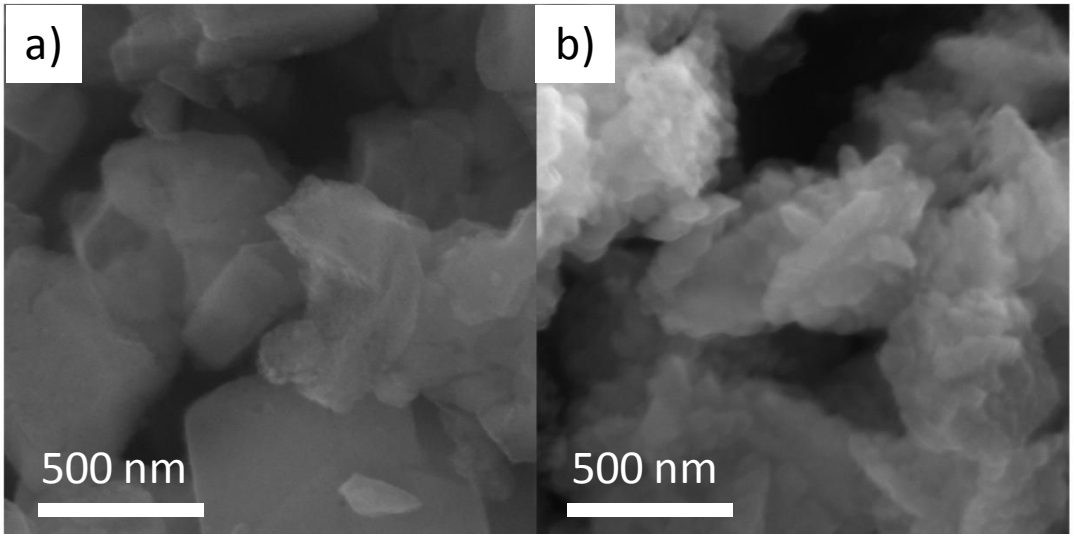

Figure 20: SEM images of CBV720 (a) and r2.3-CHA(IT) (b).

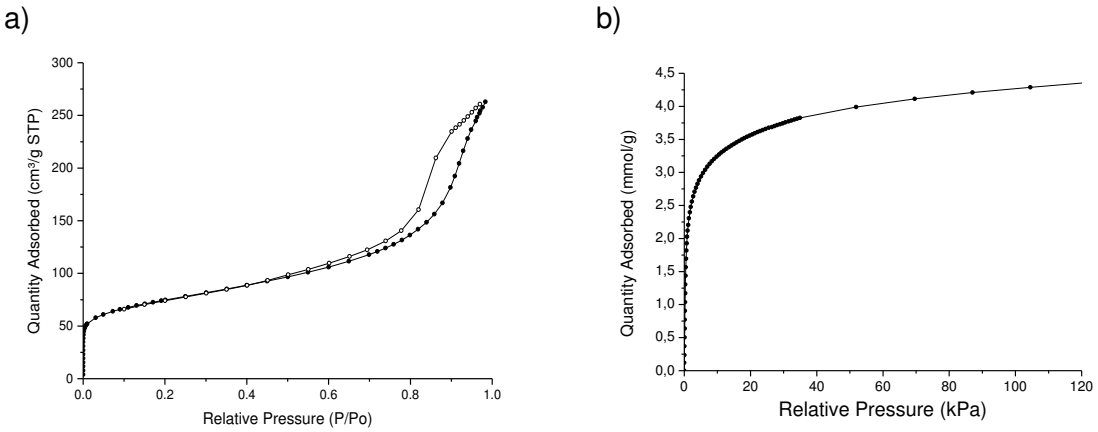

Figure 21: (a) N_2 at -196 °C and (b) CO_2 at 0 °C physisorption isotherm of r2.3-CHA(IT).

As shown in Figure 21b, the adsorption isotherms of pure CO_2 on r2.3-CHA(IT) were measured at 0 °C. The adsorption equilibrium capacity is 4.35 mmol/g at 120 kPa. This value corresponds to the materials studied in the literature in this Si/Al range.[80] Here, the synthesized CHA materials contain well-dispersed nanocrystals.

B. Target properties

The Table 7 summarizes the desired physicochemical properties. We have seen in Chapter 1 that the Si / Al ratio must preferentially be lower than 3, but preferentially between 2.0 and 2.5, to optimize the amount of CO_2 captured and the selectivity toward CH_4 or N_2. In order to consider the material “nanosized”, the crystallites must be smaller than 200 nm.[110] Thus we will target the syntheses of crystallites with a size of 100 nm. Regarding the thermal

stability, the material must be activated at 200 °C (toward CO_2, H_2O ...), more importantly, material must be stable up to 800 °C.[111] In another hand, it is interesting to note that nanosized zeolites with low Si amount are rarely stable at that temperature.

Table 7: Targeted chemical and physical properties of CHA zeolite.

Properties	Target
Si/Al (w/w)	2.0 - 2.5
Crystals size	< 100 nm
CO_2 adsorption	4.0 mmol/g
Selectivity CO_2/CH_4	> 100
Selectivity CO_2/N_2	> 100
Regenerability	Reversible at 200 °C
Stability	> 800 °C

C. Exploration of new synthesis strategy.

In order to synthesise CHA without organic structuring agent, several parameters have to be consider:

- type and number of extra framework cations (Na, K, Li ...).

- Al_2O_3 / H_2O / Hydroxides ratios.

- hydrothermal treatment conditions (time, temperature, stirring conditions ...)

The main secondary building unit of Chabazite is the 8MR. From our expertise, we learned that Cs cation was the best for stabilizing of 8-tetrahedron windows in the case of RHO. In addition, Cs was applied as an inorganic structuring agent for Cs-ABW[44] or Cs-ANA[5] zeolites which are also composed of 8MRs. Moreover, the use of CsOH in the synthesis of seeds assistance[18] validate the use of component in the direct synthesis of CHA. The second important secondary building units of CHA structure is the D6R rings. This is also an essential constituent of the FAU structure, explaining the recrystallization of CHA from FAU (see Chapter 1.II). Iwama et al. has shown that the addition of KOH to the sodium system will favour the formation of D6Rs.[46] This secondary building unit was not present in RHO or the

other dense zeolites previously mentioned. The idea was to integrate some CsOH to the synthesis in order to form the 8RM in addition to the D6Rs obtained in presence of NaOH and KOH.

However, a freedom has been taken concerning the synthesis temperature: the majority of the syntheses of CHA were carried out at 140 °C or higher temperatures but we made the choice to work at temperature lower than 100 °C to facilitate the formation of nanocrystals. Thus, by mixing the 3 hydroxides and lowering the crystallization temperature, we hoped to identify the conditions for CHA crystallization.

D. First synthesis of nanosized CHA type zeolite

The first CHA samples synthesized are listed in Table 8. First a screening of different chemical composition was performed revelling that the low sodium amount was incompatible with the crystallization of monophasic CHA zeolite (entry 1). Increasing the NaOH amount and decreasing the Al_2O_3 proved useful to synthesise pure CHA (entry 2). The synthesis time required to obtain CHA without ANA is further optimized (entry 2-4). Additionally, the synthesis was performed under stirring conditions at 140°C for 1h25 (entry 5).

Table 8: Chemical composition and synthesis conditions used to obtain CHA phase.

Entry	Chemical composition			Hydrothermal treatment		Phase**
	Na_2O	K_2O	Cs_2O	Temp	Time	
1*	3	0.85	0.8	90 °C	24 h	CHA/EDI
2	5	0.85	0.8	90 °C	5 h	Am
3	5	0.85	0.8	90 °C	8 h	CHA
4	5	0.85	0.8	90 °C	16 h	ANA
5*	5	0.85	0.8	140 °C	1.25h	CHA

* Al_2O_3 / SiO_2=0.33 **Stirring conditions in oil bath.
** EDI = Edingtonite, CHA = Chabazite, Am = Amorphous , ANA = Analcine

The CHA crystals obtained are aggregates with a size of 2 microns (Figure 22). It can be seen that the particles are composed of crystals smaller than 100 nm.

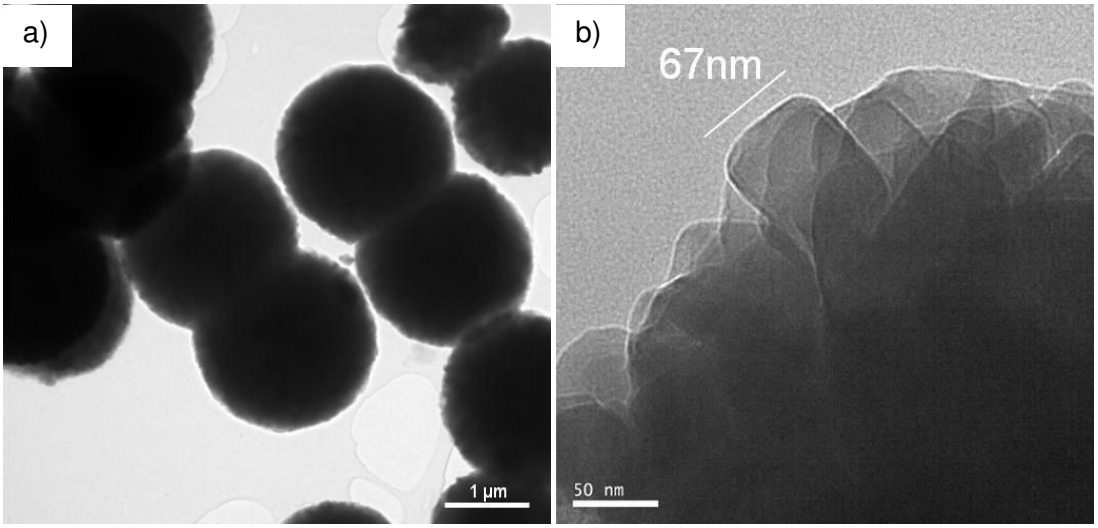

Figure 22: TEM images of CHA (entry 3): (a) M = 1 µm, and (b) M = 50 nm.

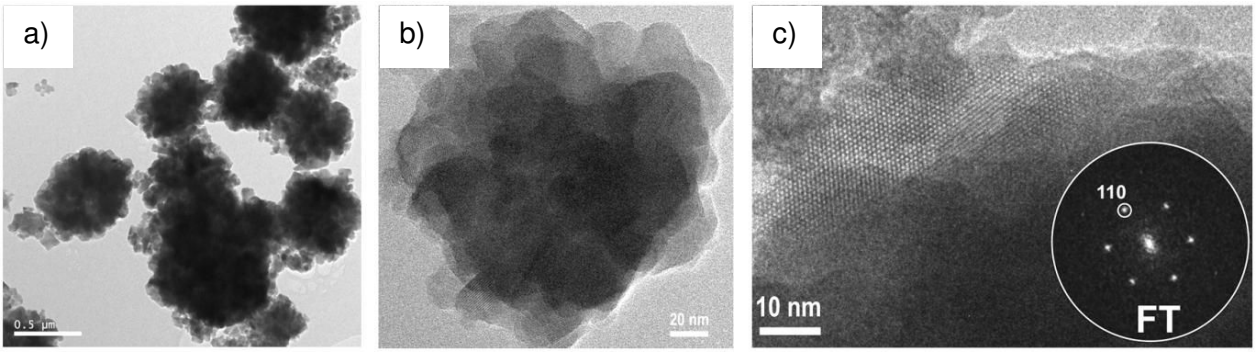

Figure 23: TEM images of CHA (entry 5): (a) M= 0.5 µm, and (b) M= 20 nm and (c) M=10 nm; Insert: Fourier transformation (FT).

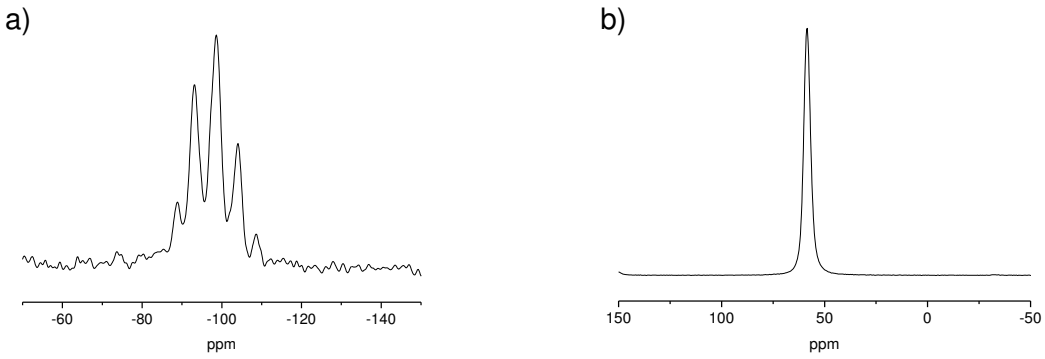

Figure 24: Solid-state ^{29}Si-MAS-NMR (a) and ^{27}Al-MAS-NMR (b) spectra of CHA zeolite (entry 3).

The ^{27}Al-MAS-NMR shows an intense and narrow peak at 58.7 ppm corresponding to the tetrahedral Al meaning that the Al atoms are well insert into the framework and extra-framework Al was found (Figure 24). The Si-MAS-NMR spectrum of the as-synthesized CHA shows five resonances centered at approximately −109 ppm, −104 ppm, −97 ppm, −93 ppm and -89 ppm, that can be attributed to Si(0Al), Si(1Al), Si(2Al), Si(3Al) and Si(4Al) environments, respectively. The Si/Al ratio is determinated 1.7.

The high crystallinity of the sample is confirmed by PXRD (Figure 25). The PXRD pattern was indexed using the CHA structure in the R-3m space group

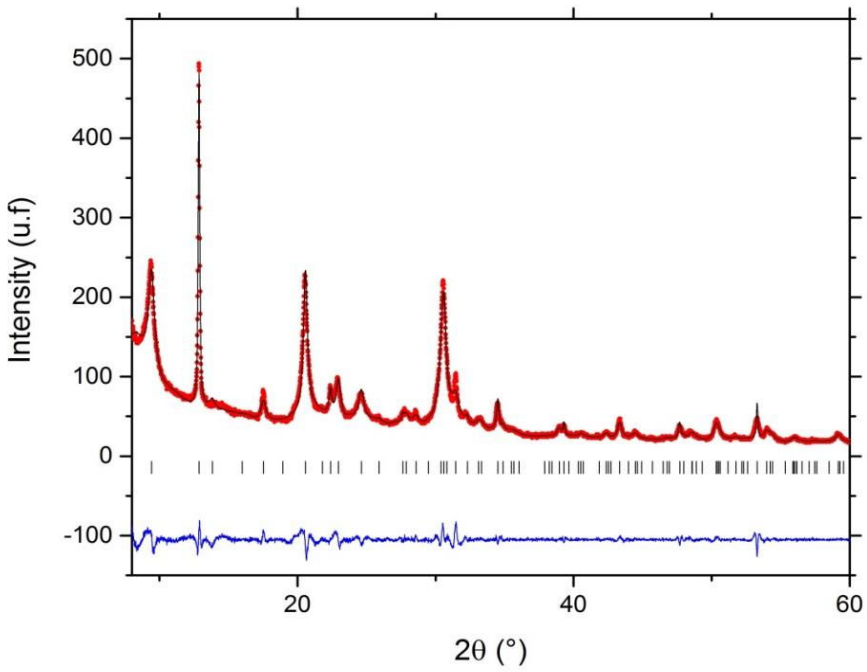

Figure 25: PXRD pattern at 300 °C for CHA and a LeBail fitting profile. The refinement gave a unit cell of a = 13.7405(6), c = 15.164(2) Å with a space group R-3m.

The first observation is that the peaks are very anisotropic. The shape of the particles seems to be a hexagonal crystal with mean sizes of 15 nm along the (ac) plan, more than 100 nm along (ab) plan. The shape of the crystallites matched the size and shape of the nanosized aggregates crystals observed with transmission electron microscopy.

III. Study of the synthesis of CHA zeolite

In the previous section we demonstrated that CHA could be synthesized without OSDA. Reducing the amounts of CsOH and increasing NaOH and KOH was carried out in order to prepare pure CHA and eliminate the side phases.

A. Optimized synthesis of agglomerated nanosized CHA

The optimized CHA-type zeolite was prepared in the absence of organic template as described previously in the Chapiter I.B.2. The final precursor suspension has the following molar composition:

$$8.0\ Na_2O\ /\ 1.25\ K_2O\ /\ 0.3\ Cs_2O\ /\ 10\ SiO_2\ /\ 0.8\ Al_2O_3\ /\ 120\ H_2O.$$

Different samples were synthesized and summarized in Table 9 showing the importance of the 3 hydroxides. Elemental analysis of the final zeolite samples indicated that the Si/Al ratio is 1.7. SEM images of CHA sample show aggregates of size of 800 nm with individual crystallites of 30-100 nm (Figure 27). The zeolite nanocrystals exhibit flake morphology with well-developed faces. This size was determined using the PXRD data, confirming the size of 180 nm. In addition, the N_2 adsorption isotherm shows a hysteresis at high partial pressure P/P° typical of aggregates nanocrystals (Figure 26b).

Table 9: Screening of hydrothermal conditions to obtain dispersed CHA nanocrystals.

Entry	Chemical composition			Hydrothermal treatment		Properties of crystals		
	Na_2O	K_2O	Cs_2O	Temp.	Time	Phase	Si/Al (w/w)	Particle size
6	**8**	**1.35**	**0.30**	**90** °C	**8 h**	**CHA**	**1.7**	**900 nm**
7	-	1.35	0.30	90 °C	8 h	Am	-	-
8	8	-	0.30	90°C	8 h	RHO	1.4	< 200 nm
9	8	1.35	-	90°C	8 h	FAU (EMT)	1.4	< 300nm

This entry 6 will be the starting point of the understanding the key parameters governing the formation of disaggregated CHA (single) crystals.

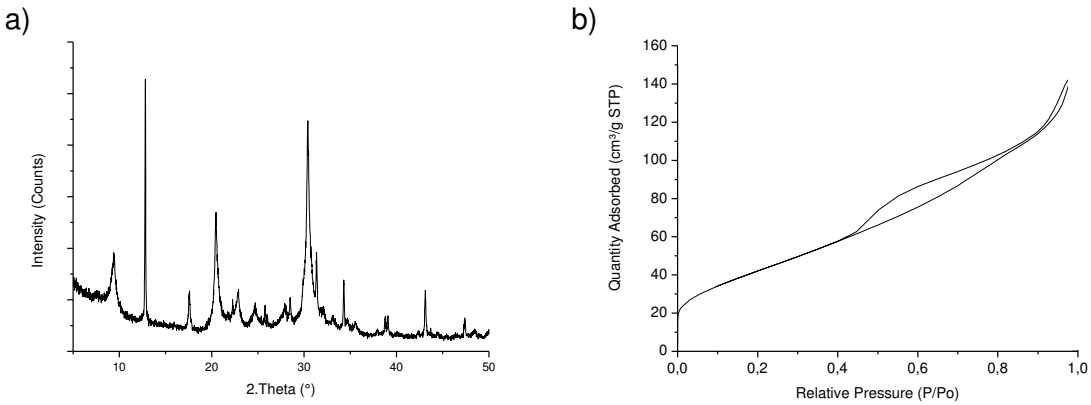

Figure 26: PXRD pattern(a) and N_2 adsorption isotherm (b) of aggregated nanosized CHA (entry 6).

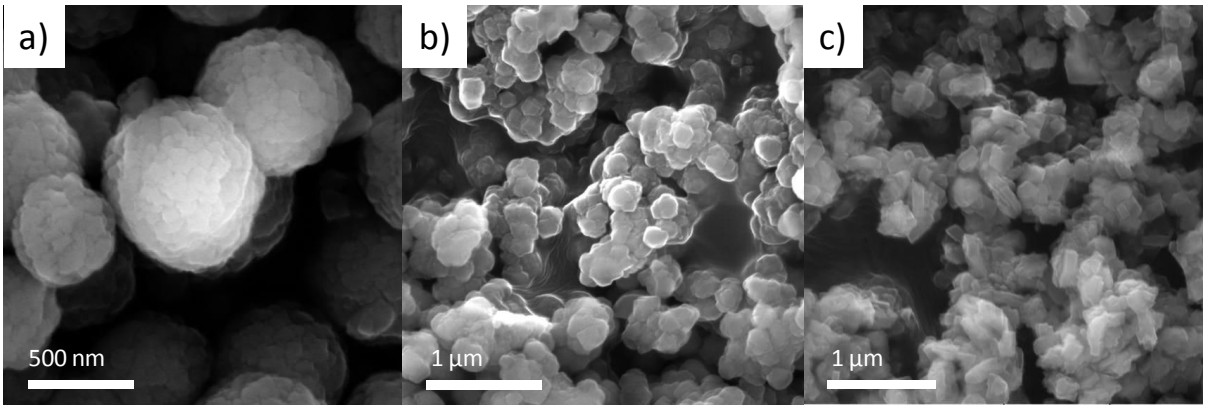

Figure 27: SEM pictures of (a) CHA (entry 6), (b) RHO (entry 7), (c) FAU (entry 8).

B. Importance of initial chemical composition of precursor suspensions

The phase diagrams representing the crystallization field of CHA zeolite in the presence of different amounts of KOH and CsOH is presented in Figure 28. The synthesis time is adapted to avoid the formation of ANA: the synthesis of some zeolites is faster than some others. For example, the RHO (y=0 and x=0.6) need 1h15 of hydrothermal treatment in those condition, while CHA (y=1.0 and x=0.4) starts to be crystalline after 8h.

The chemical composition of K_2O and Cs_2O for the precursor suspensions of 0.3:1.25, 0.4:1.0 and 0.6:0.7 provided pure CHA. Reducing the Cs_2O or the K_2O values result in impurities such as BPH and RHO. Likewise, increasing the hydroxide content leads to formation of EDI and make easier the formation of ANA.

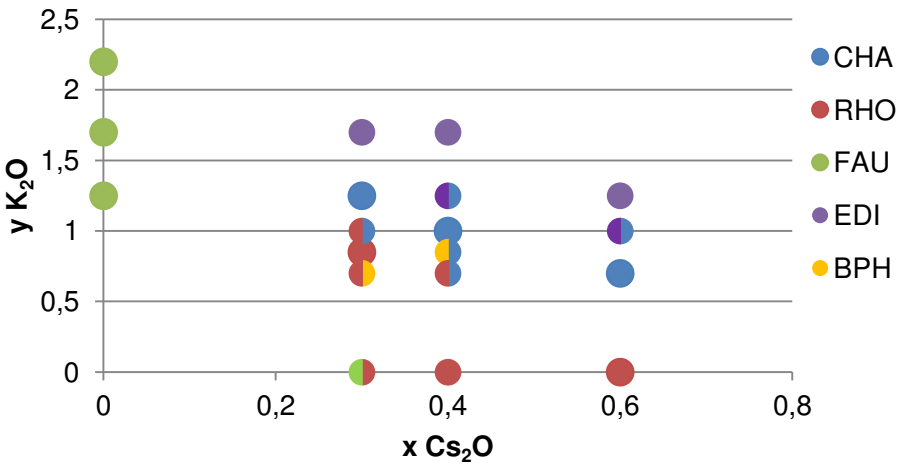

Figure 28: Effect of Cs_2O and K_2O amount in the synthesis of zeolites. Synthesis of zeolites from precursor suspension: $10Si_2O$ / $0.8Al_2O_3$ / xCs_2O / yK_2O / $8.0Na_2O$ / $110H_2O$, containing different amounts of CsOH and KOH at 90 °C.

EDI = Edingtonite (K-F type), CHA = Chabazite, FAU = Faujasite (LSX type), BPH = Beryllophosphate-H (Linde Q type).

It is interesting to note that once the Cs content was fixed to Cs_2O = 0.3, several zeolites were obtained as pure phases by varying the amount of K_2O introduced into the synthesis precursor suspension. Table 10 lists pure zeolites and zeolite mixtures obtained as a function of the amount of KOH used.

Table 10: Zeolites obtained from precursor suspensions with different amount of K_2O.

K_2O	Zeolite	Density T_{atom} / A^3	Density cm^3/mol	Si/Al (ICP, w/w)
0	RHO/FAU	-	-	-
0.65	RHO	14,5	41,7	1.4
0.8	RHO/BPH	*	-	-
1.0	CHA/RHO	-	-	-
1.25	CHA	15,1	40,3	1.7
1.5	EDI	16,1	37,9	1.2

* density of BPH = 14.6 T_{atom} / A^3

Table 11: Zeolites obtained from precursor suspensions with different amount of Cs_2O.

Cs_2O	Zeolite	Density T_{atom} / A^3	Density cm^3/mol	Si/Al (ICP, w/w)
0	FAU	13.3	45.0	1.4
0.3	RHO/BPH	-	-	-
0.4	RHO/CHA	-	-	-
0.6	CHA	15.1	40.3	1.7
1.0	ANA	19.2	31.0	2.0

It can be noted that the density of the zeolites obtained under increasing the amount of K_2O also increases (Table 11). As described previously, the absence of KOH in the synthesis gives mainly RHO (14.5) and a low amount of FAU zeolite (density: 13.3).

In view of the experimental conditions, it is clear that the less dense phase such as LTA, FAU, RHO will be formed under low KOH and CsOH amounts. Marlon T. Conato and coworkers concluded that their ternary phase diagram of zeolites prepared at high Si/OH and Si/Al molar ratios in OSDA-free conditions *"revealed that high alkali concentration facilitated zeolite nucleation by promoting the formation of aluminosilicate polymeric species*"[112]. They do not provide any conclusions regarding a correlation between phase changes and a hydroxides concentration. Till now, I didn't find any explanation of the obtaining of dense phase at high CsOH or KOH content. Curiously, the temperature increasing leads to the same phenomenon: formation of denser phase at high temperature as described by the Ostwald low (Chapter 1). So, the impact of the synthesis temperature on the preparation of zeolites will be further explored.

C. Effect of temperature

Chabazite was prepared under hydrothermal conditions within the temperature range of 90 - 160°C (Table 12).

Table 12: Synthesis of CHA zeolite at different temperatures.

Entry	Hydrothermal treatment		Phase	Properties	
	Temp.	Time		Si/Al (w/w)	Particle size
10	25 °C	12 days	BPH	1.5	10-70 nm
11	70 °C	20 h	BPH (CHA)	-	-
12	90 °C	8 h	CHA	1.7	800 nm
13	120 °C	4 h	CHA	1.7	800 nm
14	140 °C	1.25 h	CHA	1.8	> 5 µm
15	160 °C	0.75 h	ANA	-	-

Chemical composition: 10 Si_2O / 0.8 Al_2O_3 / 0.3 Cs_2O / 1.35 K_2O / 8.0 Na_2O / 110H_2O.

Pure CHA phase could be obtained at synthesis temperatures higher than 90 °C. The synthesis time decreased much with the increase of synthesis temperature for the samples to avoid the formation of ANA secondary phase.

The Si/Al ratio of the crystals was independent of synthesis temperature, while synthesis above 140 °C resulted in the formation of agglomerates and crystals with bigger sizes.

CHA consists of spherical aggregates with a temperature dependent particle size of 500-5000 nm. The ICP results showed that all samples have a Si/Al values in a range of 1.7-1.8.

Increasing the temperature of the synthesis leads to an increase of crystallites and aggregate sizes, as shown by PXRD using the Scherrer formula. As the Cs amount decreases with temperature rising, the CO_2 adsorption decreases. At this stage, we can't know what is the reason for adsorption decreasing. Further results will be presented in the next Chapter concerning the CO_2 adsorption capacity of these samples synthesized at 90 °C instead of 120 °C.

Table 13: Properties and CO_2 adsorption capacity of aggregated CHA zeolite crystals.

Entry	Temperature	Time	BET Surface Area (m^2/g)	Micropore volume (cm^3/g)**	Crystallites size (nm)*
12	**90** °C	**8 h**	157.2	0	19 / 186
13	**120** °C	**4 h**	-	-	16 / 169
14	**140** °C	**1.25 h**	59.0	0	47 / 348

** The average sizes of the crystallites in the (ab) plane were obtained from PXRD using the the Scherrer's equation on the reflection [2, -1, 0] using the corresponding peak at 12.82°. ** Calculated from the t-plot method*

Those results demonstrate that the synthesis at low temperature (90-100 °C) is preferred to avoid the formation of BPH or ANA and the formation of bigger aggregates. The next resultants target the disaggregation of the particles.

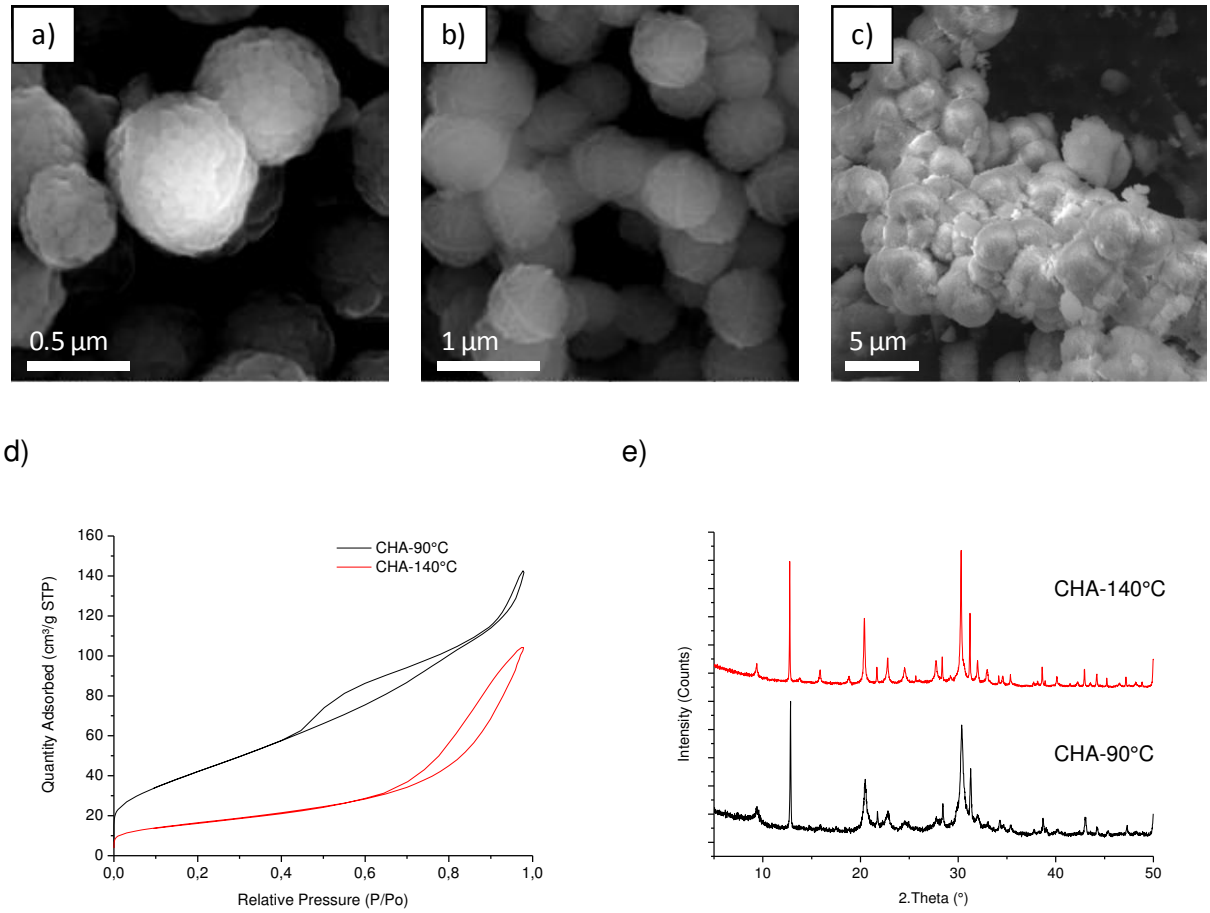

Figure 29: Characterisation of the CHA synthesised at different temperatures. SEM images of CHA at (a) 90°C, (b) 120°C and (c) 140°C zeolite samples, (d) N_2 adsorption results and (e) PXRD patterns of CHA at 90°C and 140°C.

D. Synthesis of agglomerated CHA zeolite

An aluminate precursors aqueous suspension was prepared by dissolving 0.512 g of $NaAlO_2$ in 3.34 g of double distilled H_2O. This suspension is a clear suspension. A silicate precursors aqueous suspension was prepared in 4.97 g of double distilled H_2O by mixing 6.667 g of colloidal silica (LUDOX® HS30) with 1.94 g of NaOH, 0.550 g of KOH, 0.599 g of CsOH (aq. 50%). As a result, a warm turbid suspension was obtained due to the exothermic reaction. The turbid turns into clear suspension after 10 minutes and it is stirred for additional 1h. The aluminate precursors aqueous suspension was added dropwise under vigorously stirring to the silicate precursors aqueous suspension kept in ice. The weight ratio of the aluminate precursors aqueous suspension over the silicate precursors aqueous suspension is equal to 0.387.

The resulting clear suspension for entry 1' had the following molar compositions (Chapter I.B.1): 10 SiO_2 : 0.8 Al_2O_3 : 8 Na_2O : 1.25 K_2O : 0.30 Cs_2O : 140 H_2O

This resulting clear suspension was then mixed during 20h at room temperature (e.g. 25°C) under vigorous stirring (e.g. 800 rpm). Then, the hydrothermal crystallization was conducted at 90°C for 8 hours to obtain a different type of particles in term of size, morphology, chemical composition. The time of hydrothermal treatment depends on the temperature and the chemical composition. The CHA zeolite samples were purified by repeating steps of centrifugation (20000 rpm for 20 min) and dispersed in distilled water until reaching pH=8, and then freeze-dried.. The molar composition for entries 1' to 8' (Table 14) of the clear suspension after addition of the first aqueous suspension to the second aqueous suspension has the following composition:

$$a\ SiO_2 : b\ Al_2O_3 : c\ Na_2O : d\ K_2O : e\ Cs_2O : f\ H_2O$$

$a = 10.0$

$0.5 \leq b \leq 2.5$;

$6.0 \leq c \leq 10.0$;

$1.0 \leq d \leq 1.6$;

$0.05 \leq e \leq 0.60$; and

$90 \leq f \leq 150$.

Entries 1' to 8' were obtained in a yield varying between 60% and 65%. The properties of the CHA zeolite samples (Si/Al molar ratio, size of crystals and agglomerates) are summarized in Table 14. The CHA crystals are in the form of platelets whose size varies from 80 to 200 nm in the (a,b) plane with a thickness around 50 nm. The size of the crystals given Table 14 corresponds to the size obtained from PXRD using the Scherrer's equation for the Bragg peak at 9.35 ° (2θ). Note that entry 8' reveals a higher Si/Al molar ratio (1.90) and bigger particles when compared to entry 1' (1.77) due to higher dilution.

E. Design of experiment (DoE)

The synthesized materials presented up to now are micronsized aggregated particles consisting of zeolite nanocrystals.

The next experimental plan aims finding the link between the variables of an experiment (x_i) and the quantifiable quantity targeted (y_i).

The simplest plan used is the 2-level factorial plan. This type of plan has a number limited to 2 values per factor. All combinations of levels are performed in a balanced way.

2-Level fractional factorial plans 2k-q allow to study all factors but with a reduced number of trials compared to full factorial designs. The full factorial design is a combination of every variable which needs n^2 experiments (n is the number of parameters) to evaluate the entire range of possibilities. A fractional factorial design at 2 times less, or 4 times less or 2q times less than the corresponding full factorial. At the end of a fractional factorial plane, the goal is not to solve such a system but to obtain an overview of the effect of the parameters and identify the main parameters which will lead to disaggregation of particles[113].

The chosen variables were the amount of sodium (Na_2O), the amount of cesium (Cs_2O), the amount of water (H2O), the amount of aluminum (Al_2O_3), the stirring time (stirring) and the synthesis temperature (T°). Only the synthesis time and the amount of potassium will be adjusted to avoid the formation of side phases such as ANA and RHO. The modalities 1 and 2 are chosen so as to obtain CHA phase in all circumstances. All experiments are summarized in Table 14.

Table 14: 2-Level fractional factorial plans 2^6 applied toward synthesis of CHA zeolite.

	Parameters						Results		
	H_2O	Na_2O	Cs_2O	Al_2O_3	Time mixing	Synthesis temperature	Crystals size (nm)*	Aggregates size (nm)**	Si/Al (w/w)
modality 1	140	8	0,3	1	1day	90°C			
modality 2	120	6	0,2	0,7	4days	100°C			
1’	140	8	0,3	1	1 day	90 °C	136	1650	1,77
2’	140	6	0,3	0,7	4 days	100 °C	109	700	1,84
3’	140	6	0,2	1	1 day	100 °C	105	1800	1,75
4’	140	8	0,2	0,7	4 days	90 °C	233	1600	1,63
5’	120	6	0,2	1	4 days	90 °C	90	600	1,68
6’	120	8	0,2	0,7	1 day	100 °C	156	1900	1,56
7’	120	8	0,3	1	4 days	100 °C	222	800	1,64
8’	120	6	0,3	0,7	1 day	90 °C	98	1000	1,90

* Scherrer equation **SEM measurement

The results of the DoE plan are evaluated by calculating the size of the aggregates measured by SEM. Although essentially focusing on aggregate size, the Si/Al ratio was determined by ICP and the crystallite size was calculated via the Scherrer equation using the peak at 12.8 ° for each PXRD pattern.

Thus, the average effect of modality 1 and modality 2 were evaluated and combined with the other parameters (Table 15).

Table 15: Example of average effect for crystallite size evaluation for each modality (A: H_2O / B: Na_2O / C: Cs_2O / D: Al_2O_3 / E: Stirring / F: Temperature).

Entry	A1	A2	B1	B2	C1	C2	D1	D2	E1	E2	F1	F2
1’	136		136		136		136		136		136	
2’	109			109	109			109		109		109
3’	105			105		105	105		105			105
4’	233		233			233		233		233	233	
5’		90		90		90	90			90	90	
6’		156	156			156		156	156			156
7’		222	222		222		222			222		222
8’		98		98	98			98	98		98	
Average (nm)	145,8	141,5	186,8	100,5	141,3	146	138,3	149	123,8	163,5	139,3	148

The calculation of the average effects makes it possible to evaluate graphically the influence of the modality by a global average represented by a transverse black line Figure 30.

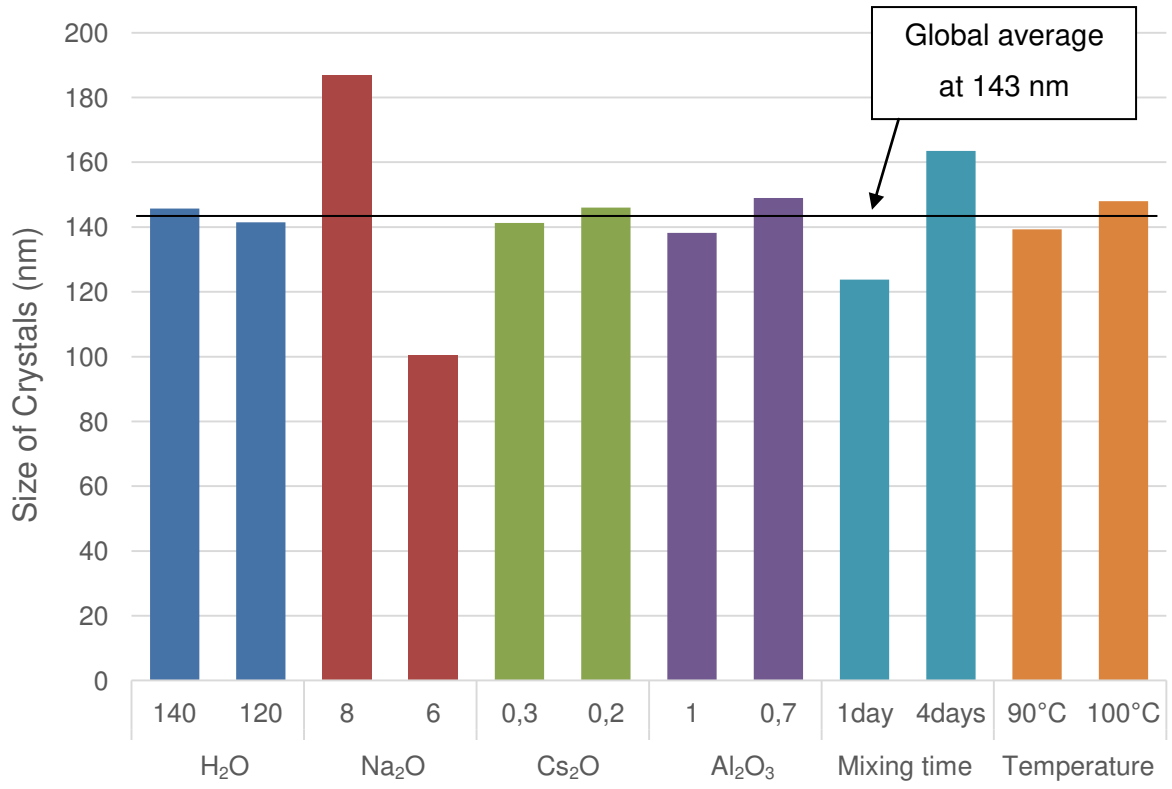

Figure 30: Graphical representation of the average effects of various modalities (1 and 2) on the size of CHA crystallites.

The average effect of each modality on the crystallite size was evaluated. The most significant parameter affecting the size of crystals is undoubtedly the amount of sodium. Indeed, for the modality "Na_2O = 8", the average size of the crystals obtained was 186.8nm whereas for the modality "Na_2O = 6", the average size was 100.5 nm. It is clear that to obtain the smallest possible crystals we primarily have to use Na = 6. It can also be seen that the agitation time of 24 hours leads to much smaller crystallites size than a stirring of 4 days (123.8 nm against 163.5 nm). This curious observation results of the “coupling of parameters”.

Here, a detailed observation of the resultants shows that the combination of "Na_2O = 8" and "mixing time = 4 days" leads to larger crystals while the combination "Na_2O = 6" and "mixing time = 4 days” keep a value closer to the global average (143 nm).

When E = 4 days of mixing and B = 6 Na_2O => Size (A,1,C,D,2) = 100 nm

E = 4 days of mixing and B = 8 Na_2O => Size (A,2,C,D,2) = 226 nm

When E = 1 days of mixing and B = 6 Na_2O => Size (A,1,C,D,1) = 102nm

E = 1 days of mixing and B = 8 Na_2O => Size (A,2,C,D,1) = 146 nm

Thus it seems that the particles grow in the presence of high amounts of sodium. This observation is very important to adjust the amount of Na_2O at the beginning of synthesis. It explain why we will prioritize the synthesis with Na_2O = 6 in order to synthesis small particles.

Figure 31, it can be seen that the average effects for the amount of water, Na_2O, Cs_2O and the stirring time are far from the average value of the 8 samples. Therefore, these are important parameters for disaggregating CHA crystals. The main parameter that has the greatest impact on aggregate size is the stirring time.

The same work was done to evaluate the parameters influencing the Si/Al ratios of the final crystalline product. It seems that the amounts of sodium and cesium have the major impact on the Si/Al ratio of the CHA samples. In agreement with our observations, it seems that for the synthesis of CHA with a Si/Al as low as possible, it is preferable to incorporate more sodium and less cesium in the synthesis gel.

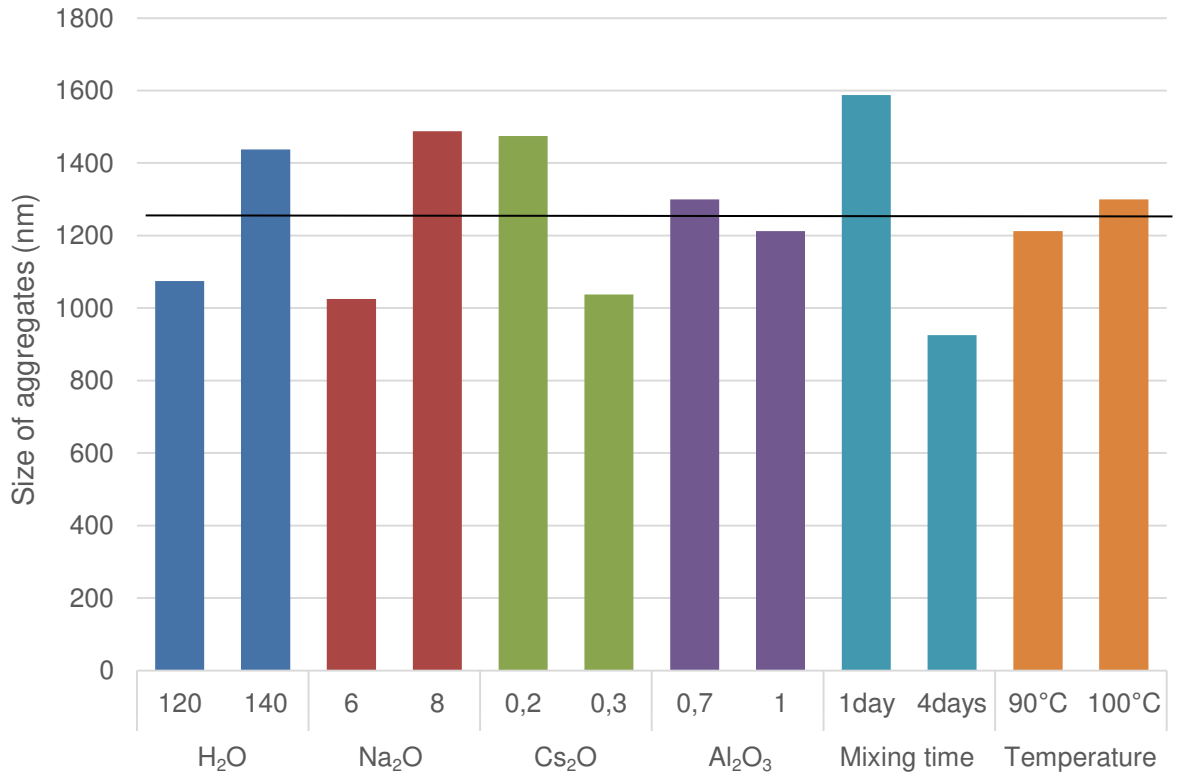

Figure 31: Graphical representation of the average effects of various modalities (1 and 2) on the size of CHA aggregates.

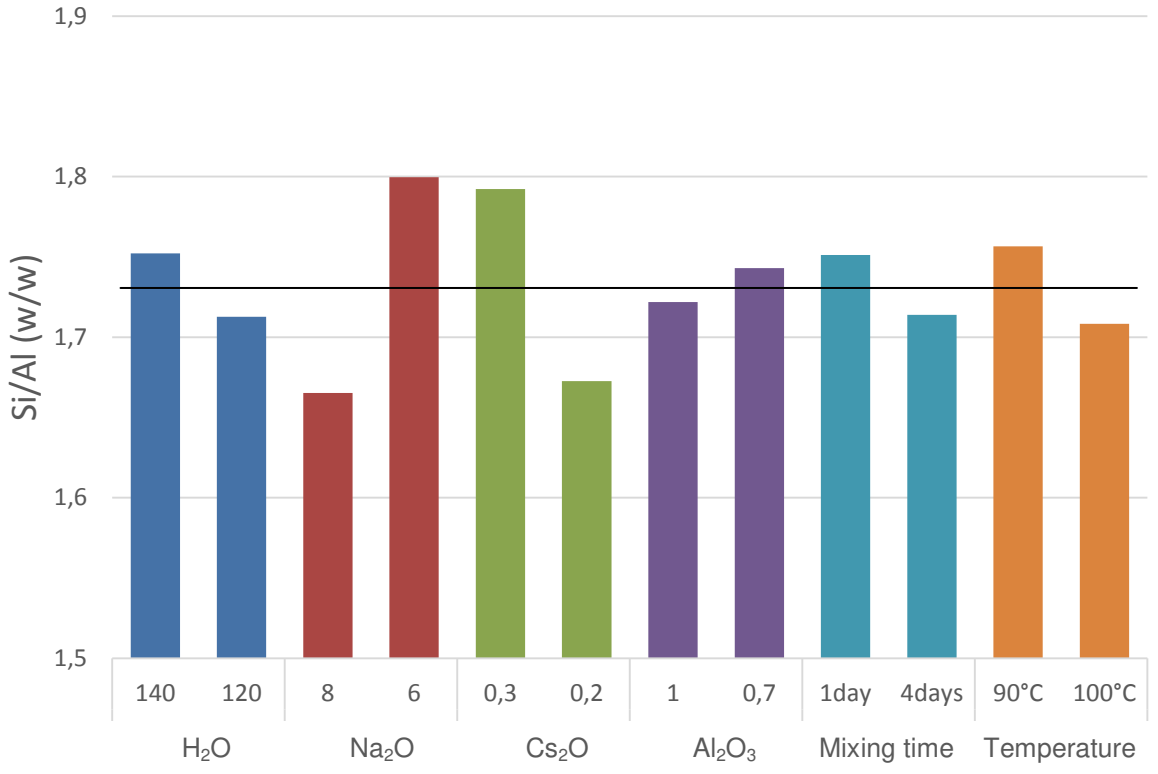

Figure 32: Graphical representation of the average effects of various modalities on the Si/Al ration of CHA aggregates or crystals.

IV. Synthesis of discrete CHA crystals

A. Discrete nanosized CHA

The synthesis of CHA zeolite with inorganic templates is affected sensitively by the cations type and amount (specially the Cs^+, see Figure 28), synthesis temperature and time. The textural properties are modified by the sodium amount, time stirring and the temperature of synthesis.

Table 16: Hydrothermal conditions used to prepare CHA zeolites.

Entry	Chemical composition					Hydrothermal treatment		Properties			
	Na_20	K_20	Cs_20	SiO_2	Al_2O_3	Stir. time	Synt. Time	Phase*	Si/Al (w/w)	Particle size (nm)**	Crystals size (nm)***
1' ****	8	1.5	0.30	10	1	1d	8 h	CHA	1.7	1650	136
16	8	1.5	0.30	10	1	1d	8 h	CHA	1.7	800	186
17	8	1.5	0.30	10	1	4d	8 h	CHA (BPH)	1.7	700	≈ 200
18	8	1.5	0.30	10	1	12d	8 h	BPH	1.4	70	74
19	6	1.5	0.30	10	1	4d	8 h	CHA	1.8	1000	≈ 100
20	6	1.5	0.30	10	1	12d	8 h	CHA	1.8	2000	≈ 100
21	6	1.5	0.25	16	0.7	12d	3 h	CHA/ ANA	2.6	200	87
22	6	1.5	0.25	16	0.7	12d	2.5 h	CHA	2.6	200	87
23	6	1.6	0.15	16	0.7	4d	8 h	CHA	2.4	300	116
24	6	1.6	0.15	16	0.7	14d	8 h	CHA	2.4	-	99

*Main phase (minority phase) / **SEM measurement / ***Scherrer equation. / **** Procedure of macronsized Chapiter II.B.1.

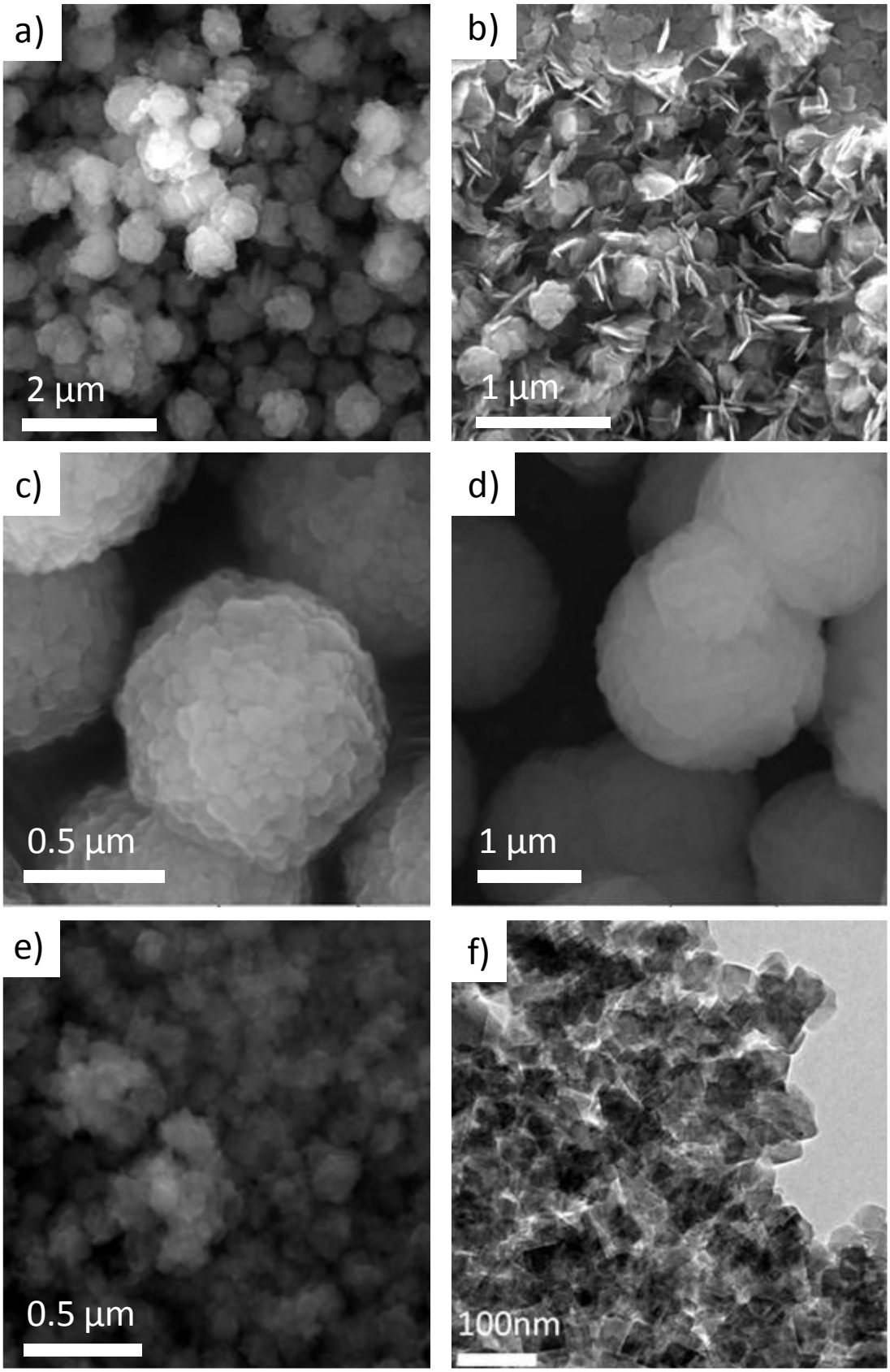

Figure 33: (a-e) SEM images of samples from entry 17-18-19-20-21-23 and (f) TEM image of sample 24.

First, stirring time was modified leading to a small diminution of the aggregate size. Unfortunately, the formation of Linde Q (BPH-type zeolites) as a side product increased with the stirring time: after 12 days of stirring, despite of the hydrothermal treatment at 90 °C, BPH without CHA was obtained. The BPH samples will be presented in the Annex 1. The NaOH content was used to control the formation of BPH and to reduce the crystal size (entry 19-20). Then, the Si/Al ratio was changed in order to disaggregate the nanocrystals (entry 21). This strategy allows synthesizing individual non-aggregated crystals; the cesium cation was reduced to avoid the formation of ANA phase. Finally, individual CHA crystals were obtained (sample 24) by increasing the stirring time and adjusting the chemical composition of the precursor suspensions. The SEM pictures are shown in Figure 33.The sample from the entry 24 fulfills all defined criteria: it is fully dispersed and composed of nanosized individual non-aggregated particles.

B. Variation of synthesis conditions: synthesis of monodispersed CHA zeolite

An aluminate precursors aqueous suspension was prepared by dissolving 0.384 g of $NaAlO_2$ in 2.551 g of double distilled H_2O. This suspension is a clear suspension. Then 1.411 g of NaOH, 0.593 g of KOH, 0.499 g of CsOH (aq. 50%) was added. As a result, a worm turbid suspension was obtained. The turbid turns into clear suspension after 10 minutes and then stirred for 2h.

A silicate precursors aqueous suspension was prepared by dissolving 10.667 g of colloidal silica (LUDOX® HS30). This suspension is a clear suspension.

The silicate precursors aqueous suspension was added dropwise under vigorously stirring to the aluminate precursors aqueous suspension kept in ice. The weight ratio of the aluminate precursors aqueous suspension over the silicate precursors aqueous suspension is 0.7.

The resulting turbid suspension for entries 22-26 had the following molar compositions:

$$16\ SiO_2 :\ b\ Al_2O_3 :\ 6\ Na_2O :\ 1.35\ K_2O :\ e\ Cs_2O :\ f\ H_2O$$

$0.4 \leq b \leq 0.6$;

$0.15 \leq e \leq 0.25$;

$130 \leq f \leq 150$;

This resulting turbid suspension was aged under mixing (*e.g.* 800 rpm) during 12 days at room temperature (*e.g.* 25°C).

Then, the hydrothermal crystallization for CHA zeolite (entry 22) was conducted at 90°C for 2.5 hours to obtain monodisperse nanoparticles of synthetic CHA zeolite.

The hydrothermal crystallization for CHA zeolite samples (entries 24, 25 and 26) was conducted at 90°C for 11 hours and up to 19 hours to obtain monodisperse nanoparticles of synthetic CHA zeolite and 3% of ANA zeolite as a side-product.

Chabazite crystals were purified by three steps centrifugation (25000 rpm for 4h) followed by redispersion in water until the decanting water reached a pH of 7, and then freeze-dried prior to further characterization.

The Si/Al ratio of the synthetic chabazite is in the range of 2.4 - 2.6. The prism-like crystals with the largest size between 80 nm and 120 nm and a thickness comprised between 15 nm and 25 nm (from PXRD using Scherrer's equation) are measured. The TEM images show crystals with a size between 30 nm and 70 nm. The surface area of 121 m^2/g was determined by BET method based on N_2 adsorption measurements. Table 17 summarizes the molar composition of the amorphous precursor mixtures used for these samples.

Table 17: Molar composition of the amorphous precursor mixtures used for different samples prepared in accordance with the procedure presented in Chapter 2.II.B.

Entry	SiO_2	Na_2O	K_20	Cs_2O	Al_2O_3	H_20	Mixing time (days)	Synthesis temperature	Synthesis time
22	16	6.0	1,35	0,25	0,6	130	12	90°C	2.5h
24	16	6.0	1,35	**0,15**	0,6	130	12	90°C	11h
25	16	6.0	1,35	0,15	**0,4**	130	12	90°C	11h
26	16	6.0	1,35	0,15	0,6	**150**	12	90°C	11h

The chemical compositions and properties of the zeolite (entries 22 to 26**)** are presented in Table 18. The Si/Al ratio of the as-prepared materials is between 2.4 and 2.6.

Table 18: Properties of the CHA zeolite samples

Entry	Formula *	Si/Al	Crystals size (nm)**	Specific surface area (m^2/g)	CO_2 uptake (mmol/g)***
22	$(Cs_{4.2}K_{5.3}Na_{1,1})Si_{25,4}Al_{10,6}O_{72}$	2.6	87	112	4.70
24	$(Cs_{5,2}K_{4,7}Na_{0,9})Si_{25,2}Al_{10,8}O_{72}$	2.4	99	83	3.80
25	$(Cs_{4.5}K_{4.9}Na_{0,8})Si_{25,8}Al_{10,2}O_{72}$	2.6	119	-	-
26	$(Cs_{3.7}K_{5.4}Na_{1.1})Si_{25,8}Al_{10,2}O_{72}$	2.5	90	-	-

** Determined based on ICP analysis ** Scherrer's equation *** BET experiments (At 0°C, 121 kPa; Static CO_2 isotherm adsorption).*

The crystalline yield of samples of entries 22, 24, 25 and 26 was 55%, 54%, 47%, and 54, respectively. The as-prepared sample 24 was stable up to 800°C. The ion-exchanged sample 24 with $NaNO_3$, KNO_3 and $CsNO_3$ did not collapse after calcination (450°C, 2 h). This same is an excellent candidate to study the adsorption of CO_2 (Chapter 4).

This r2.5-CHA with the smallest crystal size is excellent for the application but anisotropic peak broadenings complicate the X-ray analysis of PXRD patterns. Consequently, a material was design to make an indispensable the structural determination. The material must have a particle size around 150 nm and must be perfectly dispersed to perform electron diffraction experiments.

The most appropriate sample synthesized during the period of the PhD study for the targeted application is **r2.5-CHA**. The sample was studied in details and will be presented in the next chapters: the sample r2.5-CHA corresponds to the entry 24 (see further details chapter 4)

C. Synthesis of monodispersed r2.0-CHA zeolite.

An aluminate precursors aqueous suspension was prepared by dissolving 0.546 g of $NaAlO_2$ in 3.242 g of double distilled H_2O. Then 2.264 g of NaOH, 0.374 g of KOH, 0.699 g of CsOH (aq. 50%) was added. As a result, a worm turbid suspension was obtained due to the exothermic process. The turbid suspension turns into clear suspension after 10 minutes, and it is stirred for 2h.

A colloidal silica (LUDOX® HS30) was added dropwise under vigorously stirring (7.667 g) to the first aqueous suspension and kept in ice. The resulting milky suspension for samples 27 and 28 had the following molar composition:

$$10\ SiO_2 : 0.8\ Al_2O_3 : c\ Na_2O : 0.85\ K_2O : 0.35\ Cs_2O : f\ H_2O$$

$9.0 \leq c \leq 9.5$;

$110 \leq f \leq 130$;

This rmilky suspension was then aged for 7 days at room temperature (*e.g.* 25°C) under vigorous stirring (*e.g.* 800 rpm). Then 3 g of aqueous silicate (colloidal silica (LUDOX® HS30)) was added dropwise in order to increase de Si/Al molar ratio in the precursor suspension.[114] Then the suspension was stirred for 1 hour at 650 rpm. Then, the hydrothermal crystallization was conducted at 90°C for 8 hours to obtain monodisperse nanoparticles of synthetic CHA zeolite. The resulted CHA monocrystals were purified by three steps centrifugation (25,000 rpm for 4h) followed by redispersion in water until the decanting water reached a pH of 7, and then freeze-dried prior to further characterization. A screening of different chemical composition is shown Table S1 in annex 2

Table 19 reports the molar compositions of the amorphous precursor mixture used for the synthesis of samples **27** and **28** (extra amount of silica was added according to the procedure described above).

Table 19: Molar composition of the amorphous precursor mixtures used for CHA zeolites.

Entry	SiO_2	Na_2O	K_2O	Cs_2O	Al_2O_3	H_2O	Mixing time (days)	Synthesis temperature	Synthesis time	Si/Al (ICP)
27	16	9.5	0.85	0.35	0.8	140	7 + 10	90°C	7h	2.1
28	16	9	0.85	0.35	0.8	120	7 + 10	90°C	7h	2.0

The Si/Al ratio as determined by ICP (Table 19). This ratio was confirmed by EDX (Table S2) and Si-MAS-NMR (Figure S1). The entry 27 was chosen for further crystallographic study. For the rest for this manuscript, the name **r2.0-CHA will refer to the entry 27**. The complete characterization is described in the Chapter 4.

V. Conclusions

Small pores nanosized zeolites were synthesized in absence of organic structural directing agents (ODSA). By proper control of the gel composition and the hydrothermal treatment, EDI, ANA, and more interestingly CHA, BPH and RHO type zeolites were obtained. The CHA zeolite samples are monodispersed or formed aggregates with a size between 400 nm and 2000 nm. The present chapter highlights the study of the CHA synthesis and the synthesis strategy to prepare monodispersed and discreate particles.

Monodispersed and nanosized CHA samples with a Si/Al molar ratio in the range of 1.7 - 2.6, an average crystal size of 80 - 250 nm and a specific surface area of 50 - 200 m^2/g are obtained. These properties of the nanosized CHA zeolite samples were determined by a combination of different techniques (^{29}Si MAS-NMR, EDX, ICP, PXRD and N_2 sorption); the synthesized materials do match our target properties of CHA or CO_2 capture with an expected selectivity over CH_4 (chapter 4). We can tune the synthesis condition in order to obtain a CHA sample with different characteristics. For example, we synthesized a material with an average crystals size of 170nm and a Si/Al ratio of 2.1; this material was subjected to profound structural investigation by PXRD and PEDT (chapter 4).

The future prospect of this project consists of having a better understanding of the role of the cations leading to the formation of CHA. A decrease or absence of KOH leads to the formation of RHO. The structural determination is still a challenge but some interesting results will be presented in chapter 5. It was found that a long time aging of the initial precursor mixture leads to the formation of BPH type zeolite at ambient conditions. A summary of the most important findings is presented in annex 1.

CHAPITRE 4: CO_2 ADSORPTION STUDY ON NANOSIZED CHA-TYPE ZEOLITES

CO_2 has become one of the most important environmental issues. As a reminder, the small pores CHA zeolites (0.38 x 0.38 nm) is considered as an appropriate compound for selective adsorption and storage of CO_2. CHA zeolite with low Si/Al ratio develops a polar selectivity towards CO_2 in addition to the shape selectivity. The high aluminium incorporated in the framework is compensated by cations responsible of the polar selectivity of the CHA zeolite. Moreover, the separation ability is modifiable for CHA type zeolite with a Si/Al ratio lower than 3 due to a phenomenon named "Trap Door effect"[78,79,115,116]. Shang, J *et al.* have reported that the selectivity of low-Si CHA zeolites can be tuned and change in the following order Cs >K >Na >Li [80].

The use of FAU as starting material for further recrystallization into CHA has drawbacks such a long time synthesis (15 days at 95°C) and need to be in the ammonium form that are removed via combustion prior to use[2,8,9]. Our group has developed a low-cost and green preparation method without the use of seeds, zeolites recrystallization or OSDAs. The nanosized CHA type zeolite was synthesized by using a temple-free method[62,63,118]. The as-prepared materiel demonstrated an excellent capacity to absorb CO_2 and discriminate the CH_4 in a gas mixture. In order to study the adsorption phenomenon and the selectivity, several characterization methods have been used. The results showed that the chemical composition of the small pore CHA type zeolite and mainly the type of extra framework cations played a major role in the selective adsorption of CO_2.

The present chapter deals with the use of the nanosized chabazite-type zeolites as a sorbent for carbon dioxide. The CO_2 adsorption/desorption mechanisms in the newly synthesized nanosized CHA zeolite was studied by *in-situ* FTIR.

I. CO_2 adsorption in nanosized CHA zeolite

A. Study of r2.5-CHA sample

As shown in Figure 34a, the PXRD pattern of the as-prepared material corresponds to pure CHA type zeolite. The Si/Al ratio of the sample was 2.4 as determined by ICP, EDS and ^{29}Si-NMR. The prism-like crystals with elongated size between 80 and 100nm ((ab) plane) and a thickness of 15-25nm ((ac) plane) were synthesized.

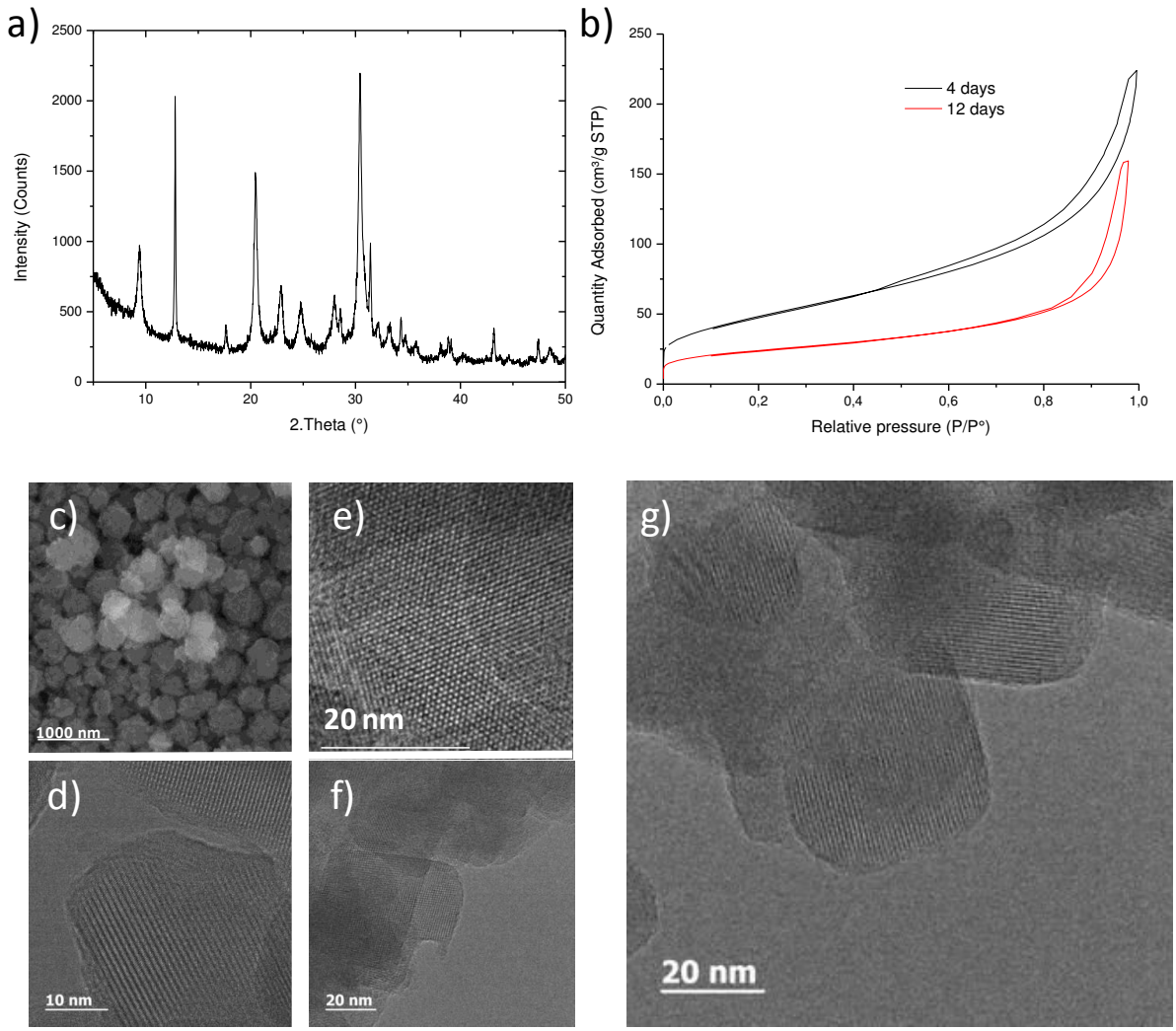

Figure 34: Main physicochemical properties of nanosized CHA zeolite: (a)PXRD pattern, (b) Nitrogen adsorption/desorption isotherms of dispersed (red) and aggregates (black) nanosized zeolite samples. (c) SEM of aggregated sample. (d-g) TEM images of the dispersed nanocrystals (sample r2.5-CHA).

The strategy to decrease the particles was based on the variation of mixing time of all compounds. The conditions of the synthesis for sample r2.5-CHA determine the morphology of the final crystals. Here, the stirring time play an important role in the disaggregation of the nanocrystals: 4 days of stirring provides 500nm aggregates (Figure 34b) and 12 days of stirring allow a disaggregation of the particles. The PXRD is not affected by the mixing time; however, the N_2 adsorption shows the intercrystallite mesoporosity of the aggregated sample. Regarding the dispersed sample, the TEM images show crystals with a size between 30nm and 70nm (Figure 34c). The surface area was 121m^2/g as determined by BET method using the N_2 adsorption measurements (Table 20).

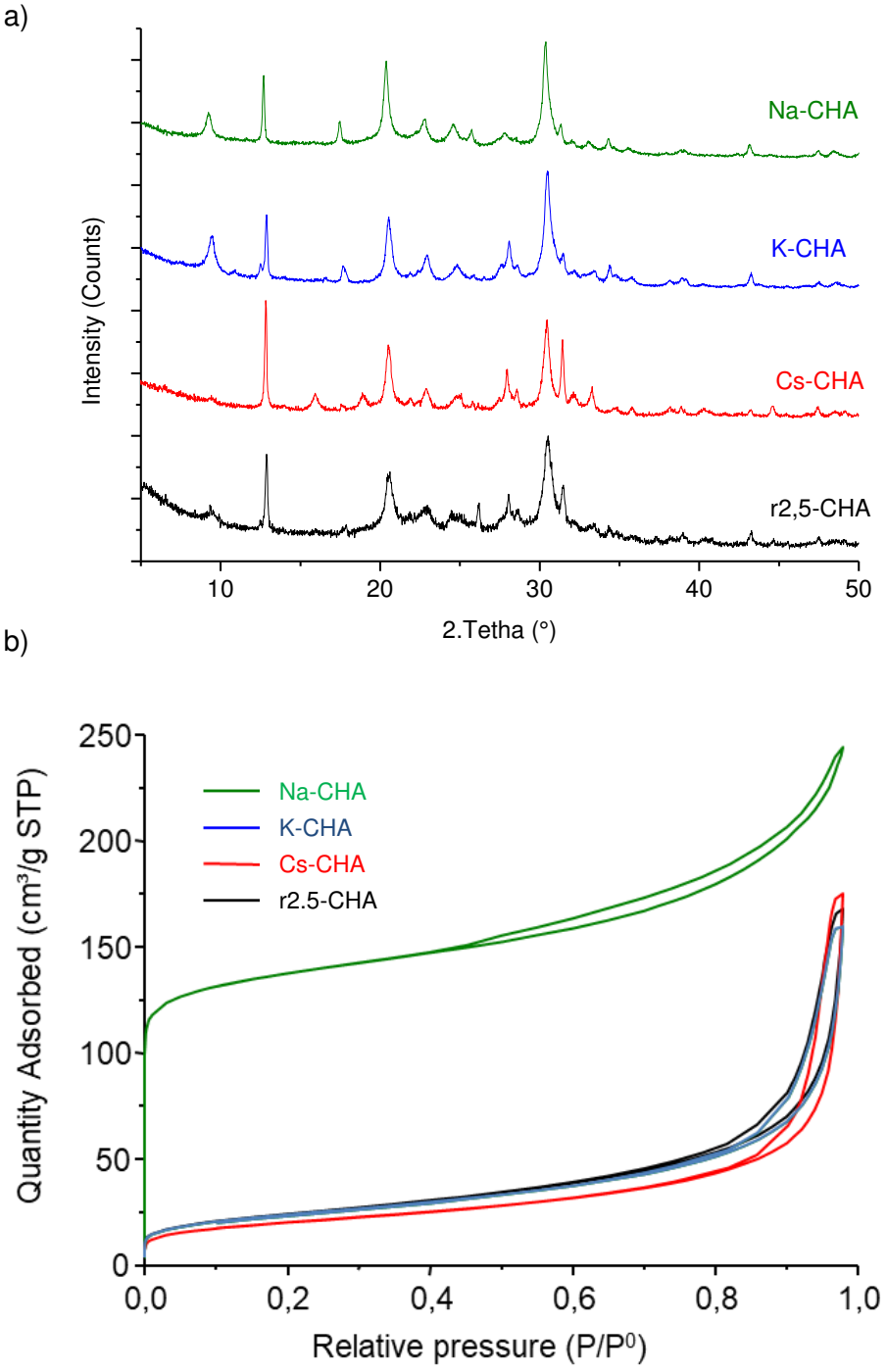

Figure 35: PXRD patterns (a) and N_2 adsorption isotherms recorded at -196 °C (b) of ion-exchanged nanosized CHA zeolites.

The CHA nanosized sample was ion-exchanged with $Cs(NO_3)$, $K(NO_3)$ and $Na(NO_3)$. The main physicochemical properties of as-synthesized r2.5-CHA, potassium form (K-CHA), cesium form (Cs-CHA) and sodium form (Na-CHA) nanocrystals CHA are presented in Figure 36. The CHA structure is preserved after ion exchange treatment. The crystallinity of

sample r2.5-CHA was preserved as shown by TG analysis (stable phase till 800°C). While the CHA structure collapse after calcination of the samples with Si/Al lower than 2.0.

Table 20: Chemical composition and porosity of CHA samples after and before ion exchange.

Samples	r2.5-CHA	Na-CHA	K-CHA	Cs-CHA
Chemical composition	$(Cs_{3,1}\ K_{5,3}\ Na_{2,2})$ $Si_{25,4}\ Al_{10,6}\ O_{72}$	-	$(Cs_{0,8}\ K_{9,8})$ $Si_{25,4}\ Al_{10,6}\ O_{72}$	$(Cs_{9,7}\ K_{0,9})$ $Si_{25,4}\ Al_{10,6}\ O_{72}$
Micropore Vol.	0.0063 cm^3/g	0.164 cm^3/g	0.0046 cm^3/g	0.0054 cm^3/g
External Surf. Area	70.4 ± 0.2 m^2/g	112,0 ± 0,5 m^2/g	75.64 m^2/g	59.72 m^2/g
BET Surf. Area	83.4 ± 0.8 m^2/g	432 ± 11 m^2/g	85.4 ± 0.7 m^2/g	71.1 ± 0.7 m^2/g

The porosity of zeolite nanoparticles before and after ion exchange treatment was investigated by N_2 sorption analysis (Figure 35). The as-prepared (Cs,K,Na)-CHA, K-CHA and the Cs-CHA zeolite samples exhibit a Type II isotherm, indicated that the micropores are not accessible, while the high adsorption uptake at higher P/P° demonstrates the textural mesoporosity of packed zeolite nanoparticles. In contrast, the pure sodium form of the CHA zeolite (Na-CHA) shows a Type I isotherm which is characteristic of microporous materials. The K^+ and Cs^+ cations are localized in the 8MR and block the access into the cage while the Na cations are set into the cage (SIII and SII) so the 8MR are accessible for N_2.[79,119–121]

B. Adsorption of CO_2 on sample r2.5-CHA

The CO_2 adsorption isotherms for samples Cs-CHA and Na-CHA are shown in Figure 36. The CO_2 adsorbed of 2.0 mmol/g and 4.0 mmol/g at 121 kPa for samples Cs-CHA and Na-CHA, respectively are measured (Figure 36). The adsorption capacities of the as-prepared CHA and the K-CHA have similar values (3.8 mmol/g at 121 kPa). In contrast, the Cs-CHA sample has the lowest CO_2 adsorption capacity as previously reported in the open literature (2.25 mmol/g at 121 kPa). This decrease of capacity might be attributed to the size and the polarity of the cation. This is reflected experimentally by a decrease in the value of $q_{sat,1}$ compared to the other samples. The CO_2 uptake increases more steeply at low CO_2 pressure for sample Cs-CHA. The role of the cations on the adsorption behavior is further studied by in-situ FTIR method.

Table 21: Dual-site Langmuir model parameters of CO_2 adsorption on CHA nanosized crystals.

Sample	Dual-site Langmuir parameters				
	$q_{sat.A}$	b_A	$q_{sat.B}$	b_B	R^2
r2.5-CHA	2.22	98.1	3.77	0.60	0.9995
Na	2.84	809.6	1.60	5.97	0.9996
K	2.54	290.4	1.41	3.09	0.9999
Cs	0.31	160.2	2.08	10.11	0.998

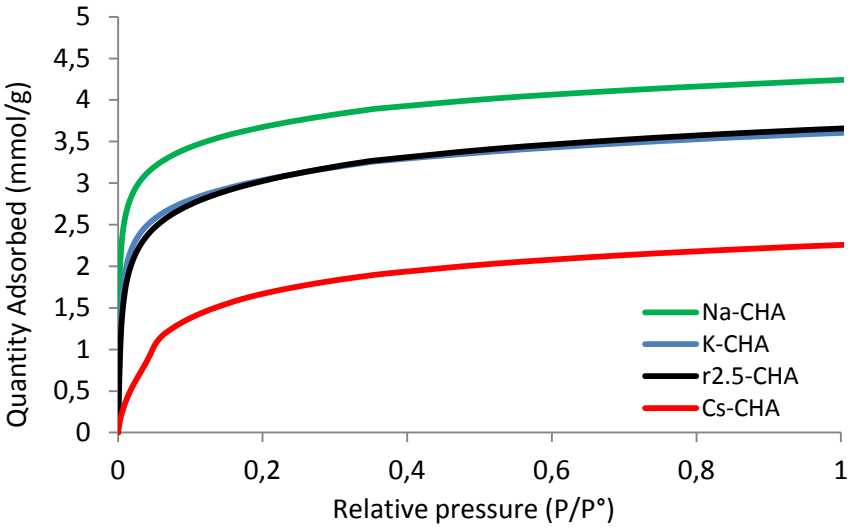

Figure 36: CO_2 adsorption isotherms on nanosized CHA samples at 0 °C: Cs-CHA (red), K-CHA (purple), Na-CHA (green) and the as-prepared sample (blue).

In-situ IR spectroscopy was carried out to study the CO_2 sorption in the as prepared r2.5-CHA sample. The adsorption of CO_2 on CHA zeolite after activation was performed at room temperature. Every 2min, a known amount of CO_2 is delivered on the pellet (23.15mg) and the difference with the reference sample is plotted. The FTIR spectra of CO_2 adsorbed on sample r2.5-CHA are shown in Figure 37. The absence of the band at 1627 cm^{-1} corresponding to water in the IR spectra conformed that the samples were activated under the conditions described above.

Three different regions evolved with the increasing of the CO_2 partial pressure: (A) 1800-1200 cm^{-1}, (B) 2400-2300 cm^{-1} and (C) 3400-3800 cm^{-1}. The (B) and (C) regions are characteristic for physisorbed while the region (A) corresponds to chemisorbed CO_2. A well pronounced adsorption band at 2347 cm^{-1} is present, which corresponds to the asymmetric stretching mode of physically adsorbed CO_2. The bridged bidentate carbonate formation is

indicated by the bands at 1350 and 1324 cm^{-1}. The observed peaks are in accordance with the results show for low silica FAU and LTA type zeolites.[75,122]

The interactions of CO_2 with the zeolite framework and extra-framework cations explain the differences CO_2 adsorption isotherms. Figure 37a shows that the bands increased with the CO_2 concentration. Interestingly, the characteristic band of physisorbed and chemisorbed CO_2 seem to evolve constantly with the increase in the amount of CO_2 at low pressure. The plot of the area of the IR band as a function of the CO_2 concentration might tend to show that the physisorption depends on the CO_2 amount (Figure 38a). However, at low pressure (Figure 38b) the carbonates formation (band at 1680cm^{-1}) is linearly time dependent (r^2=0.990). It seems that the CO_2 concentration and the time play a role in the carbonate's formation.

Figure 37b shows that the chimisorption bands hardly changes at low (P/P° < 0.01 bar) and moderate pressures. On the other hand, the characteristic bands of the physisorbed CO_2 continue to increase in intensity (band at 3703 cm^{-1}) and in width (band at 2347 cm^{-1}). The CO_2 desorption on sample r2.5-CHA was performed at RT. The characteristic bands of physisorbed CO_2 decreased together with the decrease of pressure. In contrast, the bands corresponding to the carbonates don't evolve with the pressure decreasing. An increasing of temperature at 250 °C was required to desorb the carbonates from the zeolite.

Figure 39 shows the FTIR spectra collected upon adsorption of CO_2 on Cs-CHA, K-CHA and Na-CHA samples. In all three zeolites, peaks due to carbonates formation were observed similar to the as-prepared CHA. The results suggested that the Cs cations favors the formation of carbonates species. Figure 39b shows that the Cs-CHA has the highest amount of the chemisorbed CO_2. While K-CHA, Na-CHA and as-prepared CHA have lower amount of carbonates species.

Interestingly, the physisorbed υ_3 vibrational mode for the r2.5-CHA as well as for K-CHA is observed at the same wavenumber (2347 cm^{-1}) but for Cs-CHA and Na-CHA is shifted. The υ_3 CO_2 appears at 2343 cm^{-1}, and 2345-2362 cm^{-1} for Cs-CHA and Na-CHA, respectively. This relatively small shifts are the consequence of the M^+-O=C=O interactions.

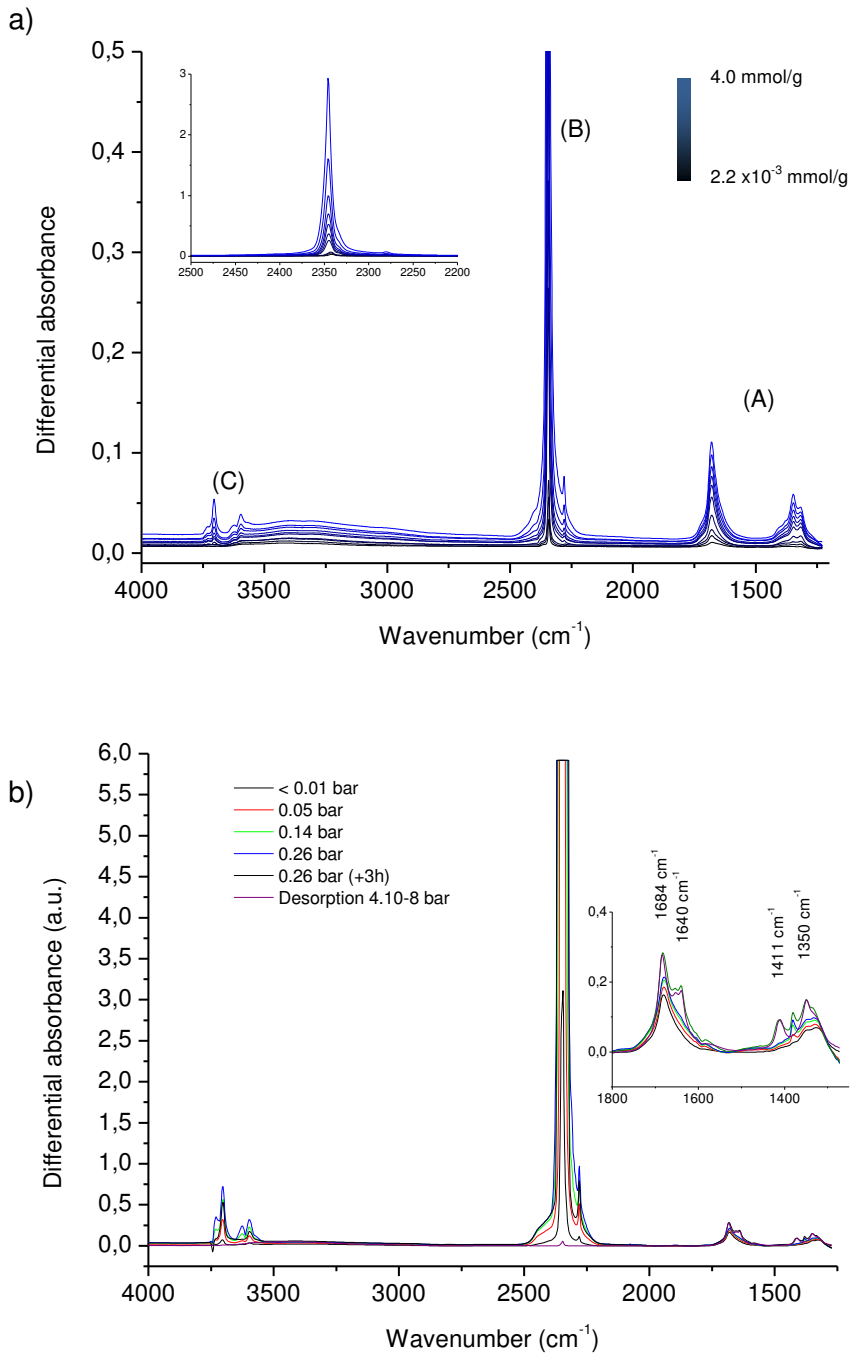

Figure 37: FTIR spectra CO_2 adsorbed on as-prepared r2.5-CHA nanozeolite: (a) small doses from $2.2x10^{-3}$ to 4.0 mmol/g of CO_2.(b) High pressure of CO_2 (black) at 0.05 bar (red), 0.14 bar (green), 0.26 bar (blue and grey) and desorbed at 4.10^{-8} bar (purple).

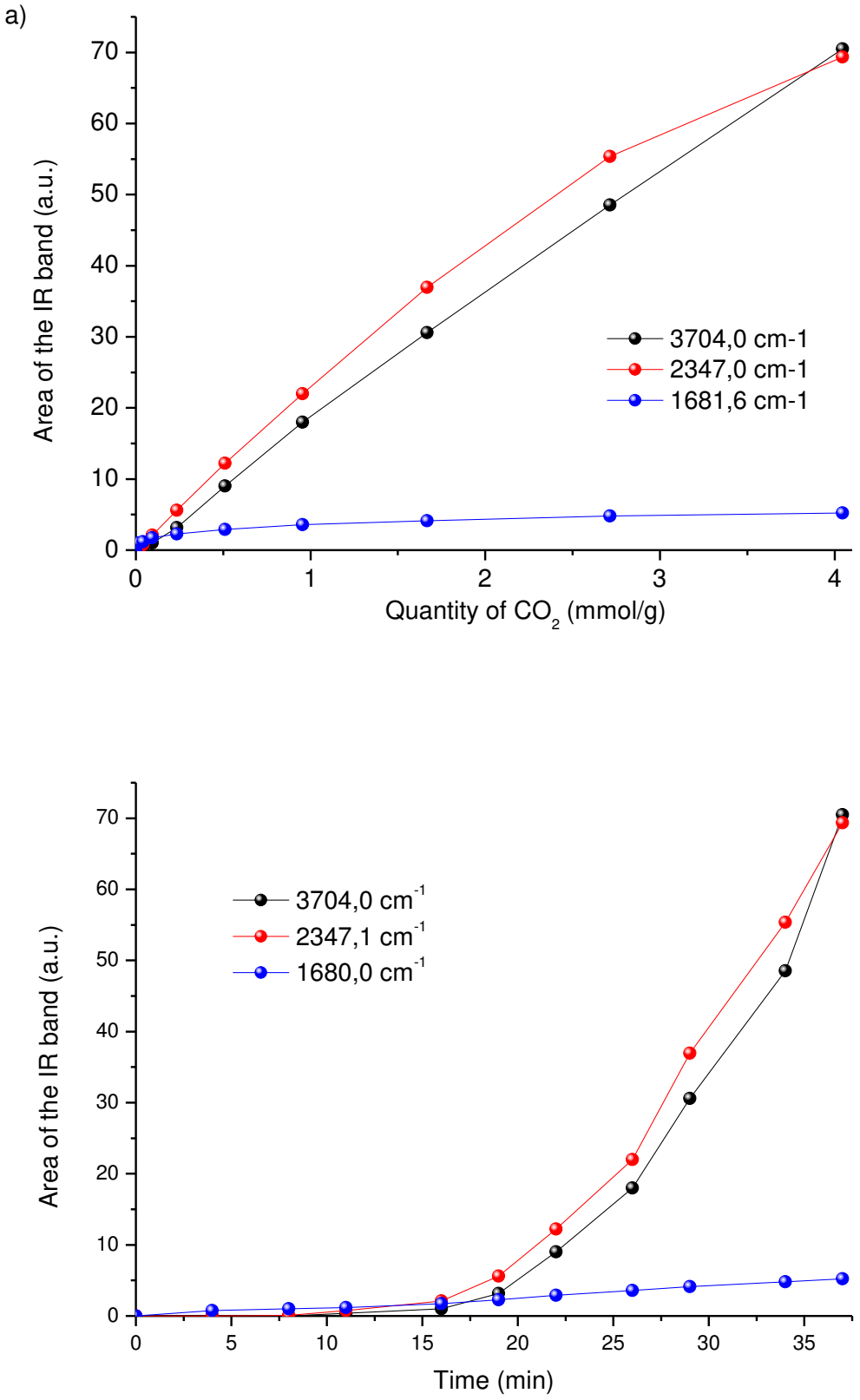

Figure 38: CO_2 sorption capacity of sample r2.5-CHA measured by integration of the area of the bands at 3704 cm^{-1}, 2347.1 cm^{-1} (red) and the band at 1680 cm^{-1} (blue) as a function of CO_2 concentration (a) and time (b).

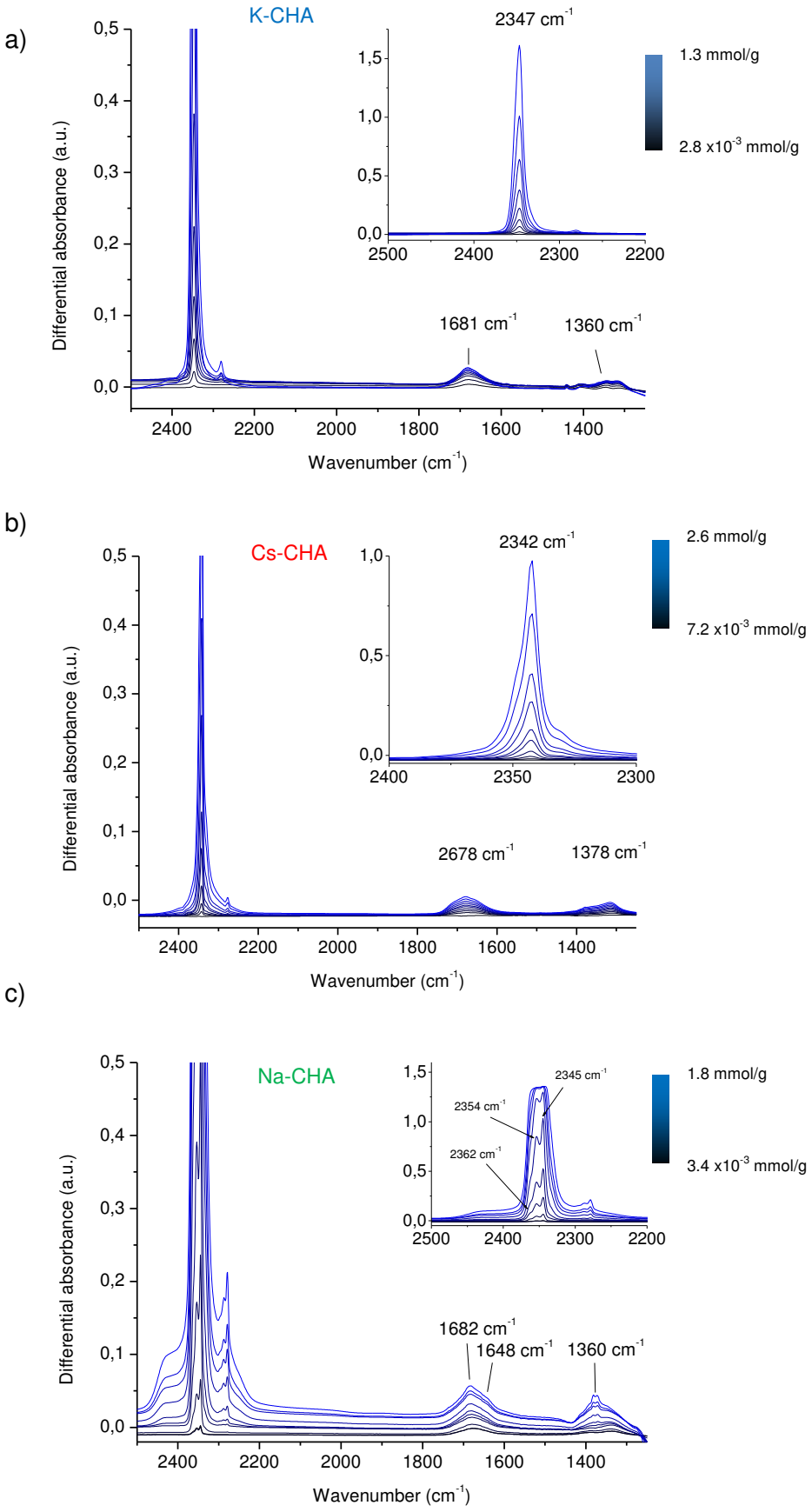

Figure 39: FTIR spectra recorded from CO_2 adsorbed on samples (a) K-CHA, (b) Cs-CHA and (c) Na-CHA.

The spectra recorded for sample Na-CHA with different amount of CO_2 are presented in Figure 39c. The physisorbed CO_2 on the Na-CHA sample is higher than on the other ion exchanged CHA. This spectrum contain 3 bands at 2345.0 cm^{-1} (area: 56 %, FWHH: 4.19 cm^{-1}), 2355.5 cm^{-1} (38%, 6.77 cm^{-1}) and 2363.6 cm^{-1} (6 %, 5.41 cm^{-1}).

The PXRD patterns of the sample Na-CHA prior and after CO2 adsorption were recorded (Figure 40). The patterns were fitted by LeBail method: R-3m space group, unit cell parameters: a = b = 13.768(2) Å, c= 15.085(4) Å for the Na-CHA hydrated and a = b = 13.752(2) Å, c= 15.089(4) Å for the Na-CHA CO_2 loaded.

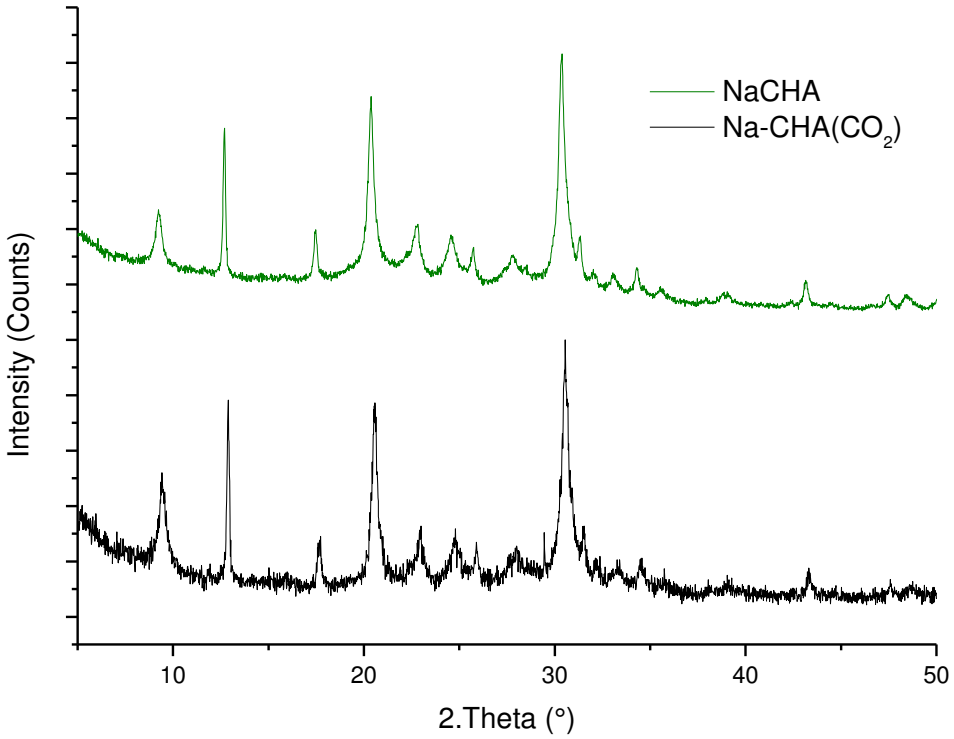

Figure 40: PXRD patterns of Na-CHA samples before and after CO_2 adsorption measurement.

However, the quality of the PXRD pattern was insufficient for a structure determination. We expected to localize the CO_2 in the 8MR where the oxygen atoms coordinate the CO_2 molecules, while other site would correspond to the physisorbed CO_2 into the cages.[123]

C. Adsorption kinetics of CO_2 on nanosized CHA zeolites

The experiments performed in this part follow the work reported by O. Cheng [124] on LTA type zeolites. The goal is to study the adsorption of CO_2 as a function of time.

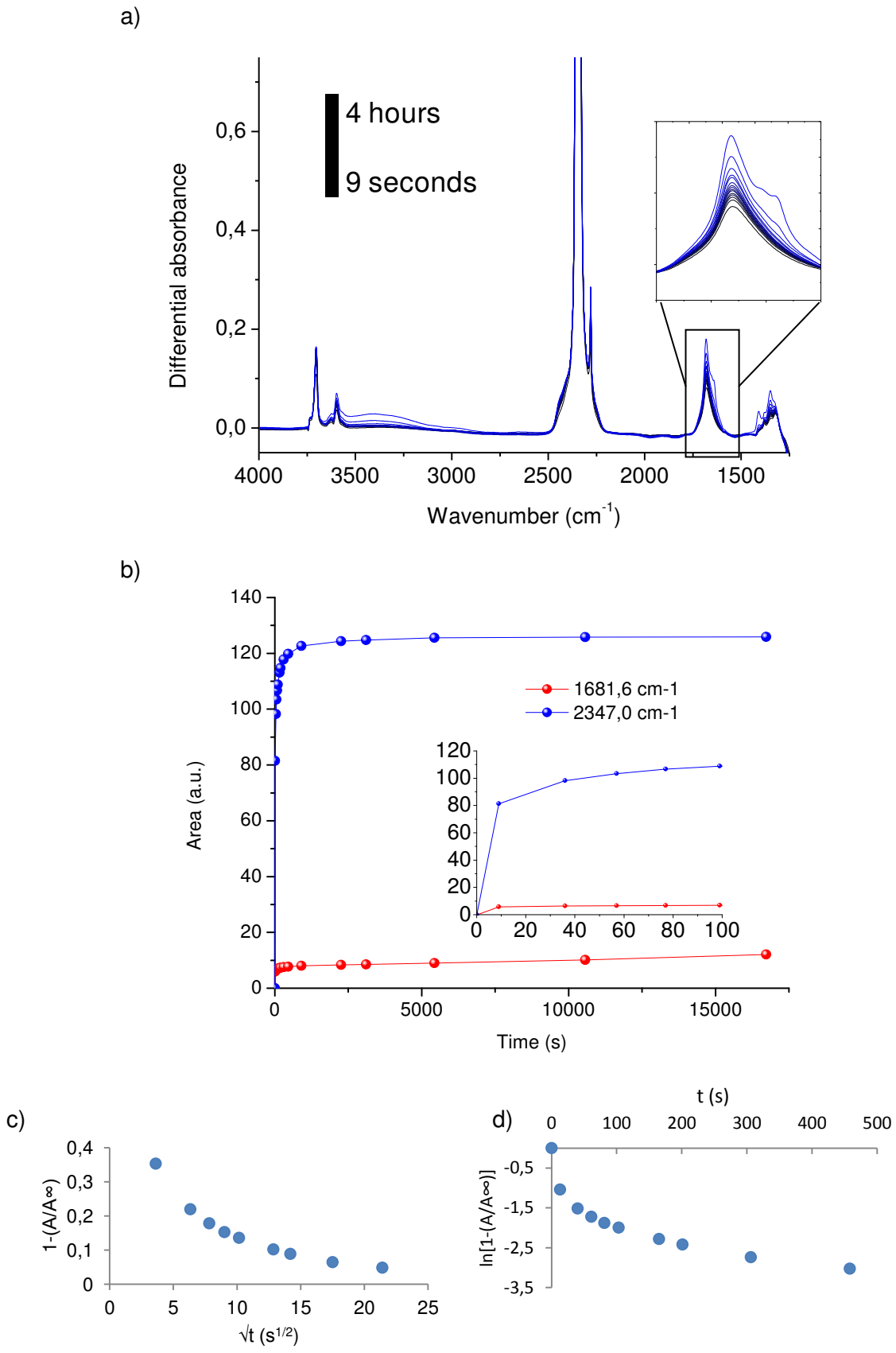

Figure 41: a) Evolution of CO_2 FTIR spectra of sample r2.5-CHA with time. b) Evaluation of the area of the bands corresponding to CO_2 species as a function of time. (c) Relative uptake capacity calculated from physisorbed IR band area as a function of square time. (d) A logarithmic relative uptake capacity as a function of time (linearly declining function indicate that a surface layer restricted the diffusion).

FTIR spectra are recorded on sample r2.5-CHA at different time. In order to be able to visualize the evolutions of the characteristic bands of CO_2, the spectra are presented after subtraction of the spectrum of the activated AMP under vacuum. The analysis time has been reduced to 4s per spectrum so that a maximum of spectrum is recorded during the initial stages of the adsorption of CO_2.

The Figure 41 shows that after 4 seconds the CO_2 is already adsorbed by the CHA sample. It can also be noted that the intensity of the corresponding bands of physisorbed (2350 cm^{-1}) and chemisorbed (1200-1800 cm^{-1}) CO_2 increases very rapidly during the first minutes until reaching a saturation after less than one minute.

About 90% of the physisorbed CO_2 is adsorbed during the first two minutes (Figure 41b). On the other hand, the peaks corresponding to the carbonates continue to increase and then reaching the plateau.

The relationship between the fractional uptake (A/A_∞) of CO_2 and the time of exposure to CO_2 can provide information on the mechanism of the transport within zeolite. Fractional uptake shows a $1-(A/A_\infty) \alpha t^{1/2}$ dependency on time while the adsorption of CO_2 is controlled by intracristallins diffusion at the initial stage. In contrast, if the adsorption kinetics is controlled by the surface resistance of a skin layer, then the fractional uptake shows a $\ln[1-(A/A_\infty)]$ dependency on time.[125]

Unfortunately, the CO_2 uptake (expressed as $\ln[1-(A/A_\infty)]$ either $1-(A/A_\infty)$) did not scale linearly with time and time square (Figure 41c and d). Hence, the data did not clearly indicate the governing uptake mechanism of CO2 adsorption in CHA zeolites. O. Cheng and coworker proposed an explanation in the case of adsorption in LTA zeolite: “A portion of CO_2 exhibited an unusually slow uptake. This small fraction could relate to the differential levels of ion-exchange in the different zeolite Na,K-LTA crystals in the sample.” As a result, the fitting might have fail because of the inhomogeneity of the cation dispersion, especially the cage keeper.

D. CO_2/N_2 selectivity

The CO_2 is expected to adsorb on two different sites: hence, CO_2 can be described adequately by dual-site Langmuir (DSL) model. The CO_2 adsorption isotherms were collected r2.0-CHA and described with the DSL model (Figure 42a).

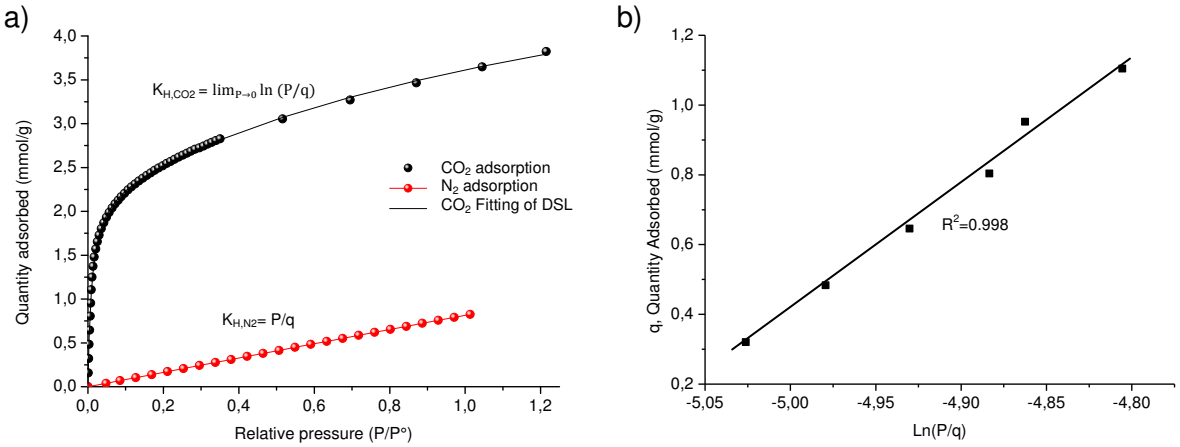

Figure 42: N_2 (red) and CO_2 (black) adsorption isotherms on nanosized CHA samples at 0 °C (a) and the plot of CO_2 quantity adsorbed as a function ln(P/q) (b).

Table 22: Henry constant of CO_2 and N_2 at 0 °C and CO_2/N_2 selectivity for r2.5-CHA sample.

Material		CO_2 capacity	Henry's constants, K_H		Selectivity
Sample	Cation	(mmol/g)	CO_2, 0 °C	N_2, 0 °C	$K_{H,CO2}/K_{H,N2}$
Ref.*	K	4.1	811	0.12	1081
	Cs	2.2	90	0.05	1791
r2.0-CHA nanosized	Na, K, Cs	3.8	165	0.82	206
	Cs	1.9	29	-	-
	K	3.4	279	-	-
r2.5-CHA nanosized	Na, K, Cs	3.7	691	0.42	1657
	Cs	2.3	72	-	-
	K	3.7	827	0.89	925
	Na	4.1	3593	1.45	2478

*Sample synthesized by recrystallization of FAU with a SI/Al=1.9 (w/w).

The calculation of the Henry's constant of CO_2 is detailed in Chapter 2.II.B by plotting the quantity of CO_2 adsorbed in function ln(P/q) (Figure 42b). Regarding the N_2, the adsorption is linear, so the value can be obtained by calculated the slope of the isotherm curve (Figure 42a). The determination of the selectivity with isothermal analyzes or breakthrough curve will

be carried out later, but today an approximate quantification has been made and the results are summarized in Table 22.

II. Structure investigation of nanosized CHA with CO_2 absorbed

The structural analysis of the CHA samples using in-situ PXRD and PEDT was initiated in the earlier stage of this work together with the optimization of the synthesis conditions toward preparation of zeolites with predesigned properties. The r2.5-CHA sample with the smallest crystal size, severe anisotropic peak broadenings complicated the Rietveld analysis of PXRD patterns. For this reason, we consider another CHA sample with slightly larger crystals with size of about 170 nm and Si/Al ratios of 2.1. This sample corresponds to entry 27 in Table 19 (Chapter 3).

This CHA sample was synthesized using inorganic cations only (Na, Cs and K). The cations not only stabilized the colloidal precursor suspensions but also prevent the Ostwald ripening during the crystallization process and thus only nanosized CHA crystals were synthesized. The nanosized CHA crystallites exhibit plate-like morphology with an average width of 100 - 200 nm (b-c).

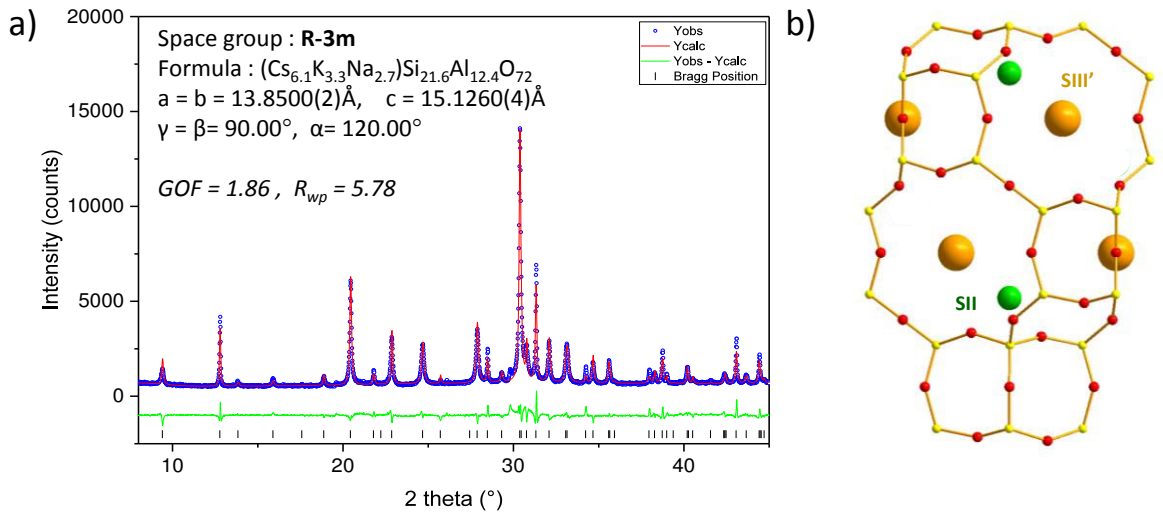

Figure 43: Characterization of as-prepared CHA sample (Table 19, entry 27). (a) XRPD pattern of the as-prepared nanosized CHA. Unit cell volume of samples and space group were obtained from electrons and X-ray diffraction data based on a Rietveld refinement and pseudo-Voigt profile function using the JANA2006 software. (b) Structure and location of cations in the as-prepared nanosized CHA.

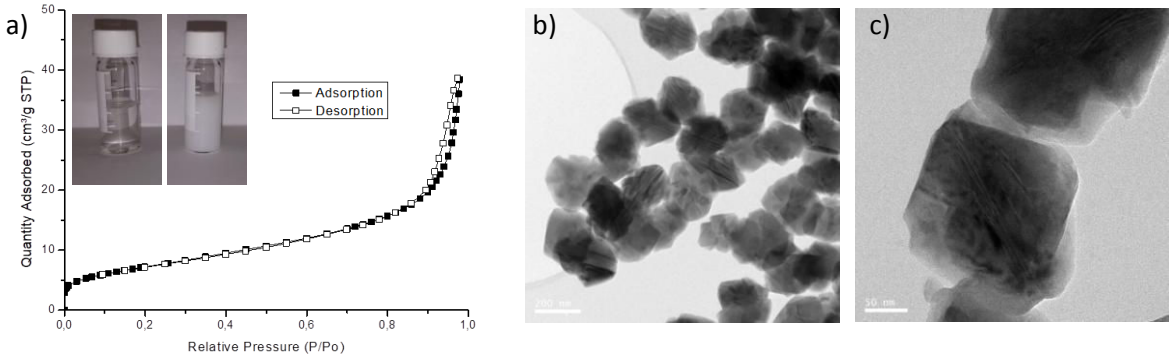

Figure 44: Nitrogen adsorption/desorption isotherms at 77 K. Insert: Pictures of suspensions amorphous gel after 1day of stirring and crystalline suspension with solid concentration of 20 wt.% (a). TEM images at different magnification of the as-prepared CHA(b-c).

The high crystallinity of the nanosized as-prepared CHA zeolite is confirmed by X-ray powder diffraction (XRPD) (Figure 43); the pattern contains all Bragg peaks expected for pure CHA zeolite.[126] The size of the CHA zeolite crystals determined by Scherrer equation is 68 nm thick and a length of 170 (R-3m space group). The nanosized CHA crystals have a Si/Al ratio of 2.0 as determined by ^{29}Si NMR; the ^{27}Al NMR spectrum shows no Al in octahedral environment. (Figure S1, Annex 2).

A. Temperature dependent X-ray powder diffraction

Temperature dependent powder x-ray diffraction (TD-PXRD) was used to track the evolution of the as-prepared hydrated CHA sample from activation by dehydration under N_2 atmosphere (1 bar) at 350°C to CO_2 absorption under CO_2 atmosphere (1 bar) from 350°C to room temperature (Figure 45). As qualitatively evidence by TD-PXRD, the absence of adsorbed molecules (H_2O or CO_2) in the CHA framework is signed by the strong intensity of the (2-10) peak observed in the dehydrated sample. We also noticed the decreasing of the unit-cell parameters after dehydration. Going down from 350°C to room temperature under CO_2 atmosphere, causes a large decreasing of this peak intensity which correlates with CO_2 entering the CHA framework. By following the evolutions of the (2-10) peak intensity and the unit-cell parameters when the temperature decreases, we can see that the CO_2 adsorption starts only around 150°C. This result is in accordance with the TG analyses (Figure 46). There is no evolution between patterns recorded at room temperature under CO_2 or N_2 atmosphere which proves that the CHA keeps the CO_2 adsorbed at room temperature. Under N_2 flux the CO_2 starts to desorb around 90°C.

B. Precession Electron Diffraction Tomography

Having the characteristics of a small pore zeolite compatible with the Trapdoor effect, we sought to obtain crystallographic information on the location of extra-framework cations and its relation with CO_2 capture capacities. The recent crystallographic studies related to the CO_2 absorption by synthetic Cs-CHA, K-CHA or Na-CHA were carried out mostly on samples containing only Cs[76], K[83,88] or Na[83] but rarely on samples with two or more extra-framework cations. As a fact, the template-free synthesis of low Si/Al CHA requires the introduction of a significant amount of three types of extra-framework cations. Although the framework of the CHA structure is known[53,127], the stabilization of nanosized r2.0-CHA using hydrothermal synthesis offers similarities with natural chabazites in terms of structure analysis requiring, notably, to locate first the position of several extra-framework cations before focusing on the guest molecules. To our knowledge, the direct localization of CO_2 from diffraction data has been investigated only for high Si/Al CHA[83] i.e. CHA without Trapdoor effect. In the past, the structures of natural chabazites were often investigated by single crystal x-ray diffraction.[87,128] This technique is undoubtedly the reference technique for fine crystallographic studies. In the present case, considering the size of the available crystals (less than 10^{-2} μm^3), we used precession electron diffraction tomography (PEDT).

PEDT data from seven nanocrystals were combined to obtain high quality intensity data. First, an *ab initio* electrostatic potential map was obtained by the charge flipping method using the program Superflip. Besides the framework structure, two extra-framework sites were found to be occupied: SIII' at the center of the 8MR and SII above the D6R (Figure 47a and b). Judging from the relative potential found on these two sites, and in agreement with previous studies on A^+-CHA, SIII' is occupied preferentially by Cs and eventually K.[129] The SII site could host K and Na.[129] However, considering the chemical composition $Na_{2.4}K_{3.6}Cs_{6.74}Al_{12.74}Si_{23.26}O_{72}(CO_2)_8$ estimated from ^{29}Si NMR spectrocopy, TG analysis and EDS (Table 23), partial or mixed occupancy of these sites are expected. To obtain a more reliable structure model and reveal fine structural details, structure refinement taking into account both the dynamical diffraction theory and the PEDT geometry was carried out.[98,99] Details about the PEDT data used for the so-called "dynamical refinement" are given Table 26.

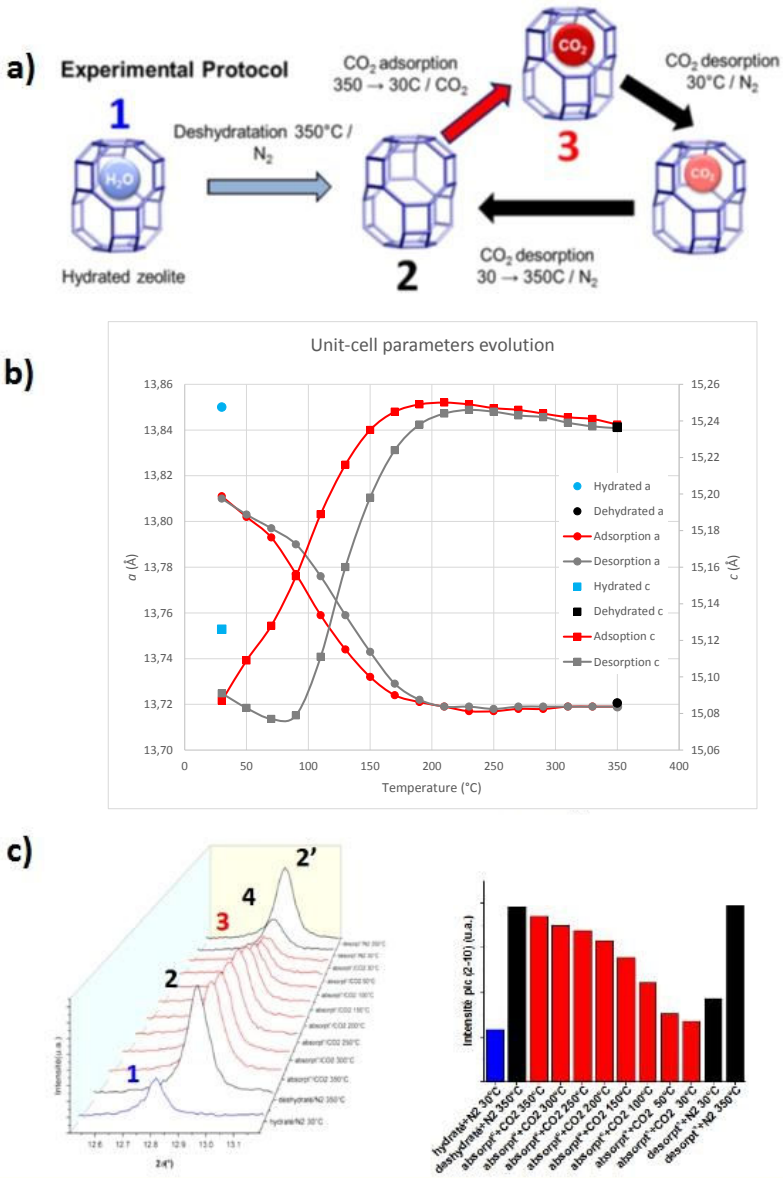

Figure 45: (a) Scheme of the activation and CO_2 adsorption procedure. (b) Change of the cell volume and unit cell parameters under adsorption and desorption of CO_2 .(c) Variations of, diffraction peak intensities (2-10), unit-cell parameters and volumes, for CHA zeolites with different crystallite sizes.

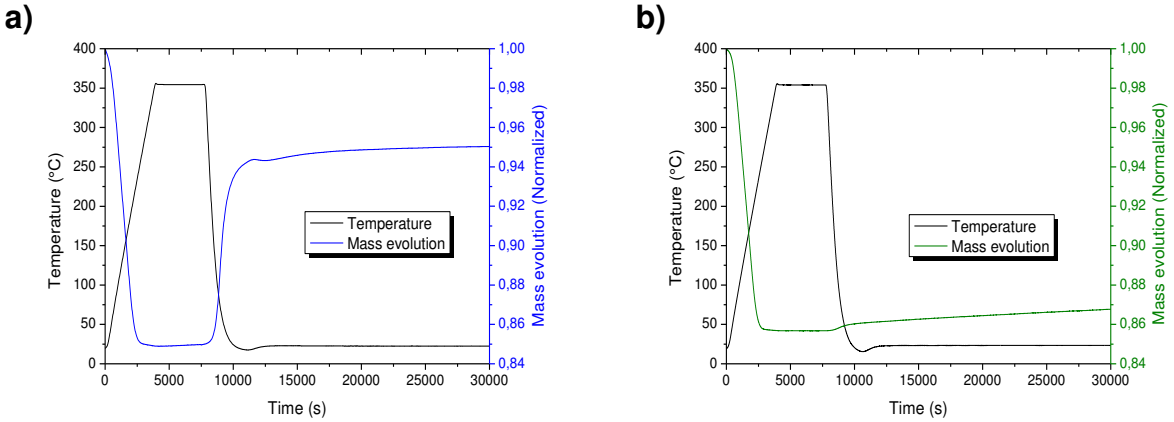

Figure 46: Thermogravimetry analysis. (a) CO_2 sorption (blue) and (b) CH_4 sorption (green) on activated as-prepared CHA. The CH_4 flow was delayed and started at 25°C instead of 350°C for a safety reason.

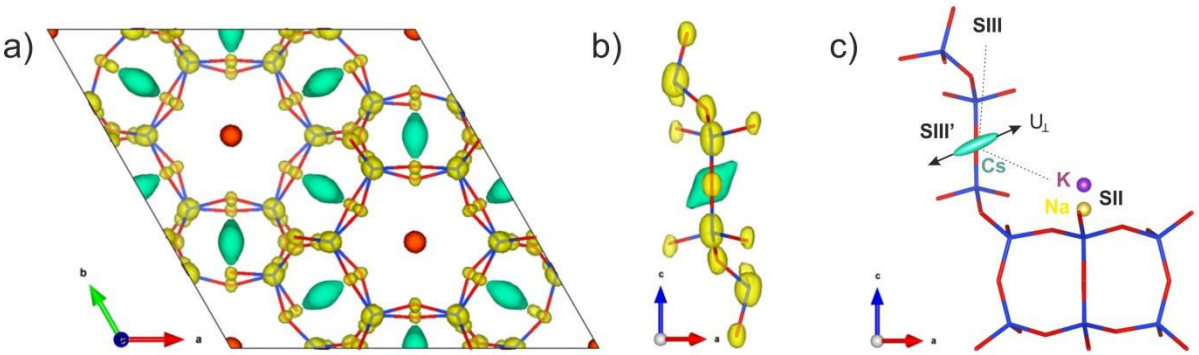

Figure 47: Electrostatic potential map obtained from superflip. Isosurface levels correspond to 3σ[V(r)]. a) Projection along c. Yellow, red and green transparent colours indicate framework, SII and SIII' sites, respectively. Tetrahedral sites (blue lines) and framework oxygen atoms (red lines) are included for clarity. b) Side view of 8MR with elongated potential around SIII' site. c) Localization of the 3 extra framework cations as obtained from the PEDT refinement.

Regarding the occupancy of the SIII' site, out of different tested models for the occupancy of this site, the best one contains only Cs atoms on the SIII' site with an occupancy of about 75%. The atomic displacement parameters (ADPs) of the Cs atoms have a noteworthy, highly anisotropic aspect with an elongation in a direction perpendicular to the 8MR. Not reported so far, this finding indicates that, even at low temperature, the door keeping cation is prone to large oscillations around its average position at the center of the 8MR in a movement compatible with is assumed as the Trapdoor effect. The mean atomic displacement parameter perpendicular to the 8MR door is about $U_{\perp}$= 0.354 Å² (Figure 47c) to be compared with $U_{\parallel}$ between 0.023 and 0.031 Å². The refinement revealed that the SII site is a split site and the observed bond lengths allowed to determine the Na and K position (see Figure 47c).

Once the extra-framework cations were identified and refined correctly, the Fourier difference map revealed the position of the guest molecules (see yellow isosurfaces in Figure 48a). Despite very large ADPs parameters, it is possible to refine the position of the CO_2 molecules that actually go to positions slightly offset with respect to the density (Table 24, Figure 48b and c). The CO_2 molecules were found in the larger cavity of the CHA framework. The molecules are approximately parallel to the c-direction and coordinate the extra framework cations. The shortest CO_2-A^+ distances are 2.61 Å for K and about 3.08 Å for Cs (Table 25).

This result is consistent with first principle calculations performed for low Si/Al Cs-CHA (r3CsCHA)[129] which is a case close to our experimental study.

Table 23: Chemical composition of the hydrated form and the CO_2 loaded form of dispersed CHA nanocrystals

CHA	TG Masse gain	Estimated composition (from EDS + TG)
Hydrated	-13.0%	$Na_{2.4}K_{3.6}Cs_{6.74}Al_{12.74}Si_{23.26}O_{72}H_2O_{28}$
CO_2 loaded	+8.9%	$Na_{2.4}K_{3.6}Cs_{6.74}Al_{12.74}Si_{23.26}O_{72}(CO_2)_8$

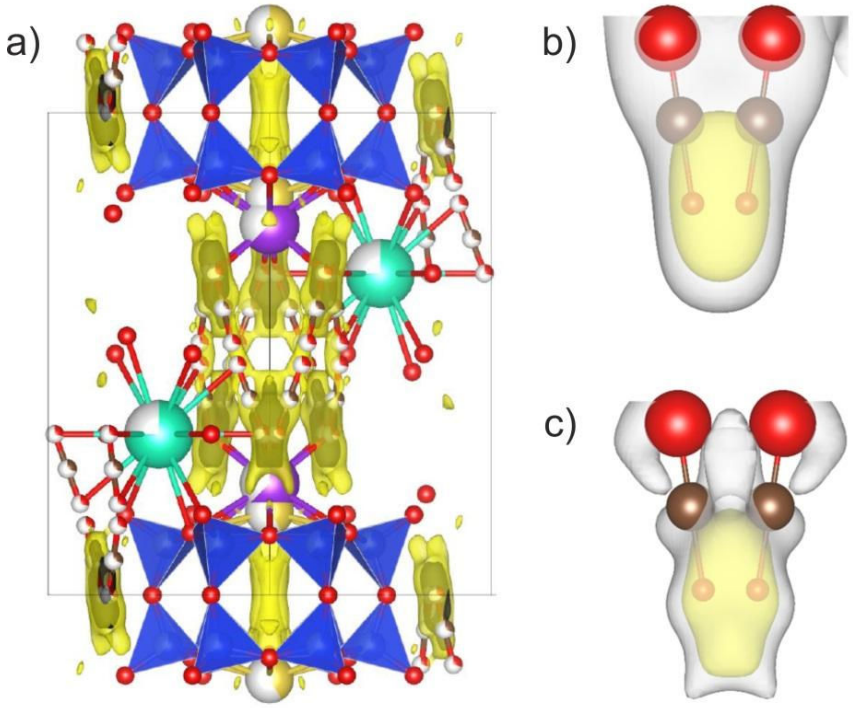

Figure 48: a) Difference potential map calculated without CO_2 once the extra framework cations are properly localized. (Yellow: 2σ isosurface. Black: 3σ isosurface, negative neglected). The CO_2 molecule obtained after refinement is superimposed as a guide to the eyes. b) Overlay of difference potential map (grey and yellow isosurface levels correspond to 2σ[ΔV(r)] and σ[ΔV(r)], respectively) and the refined position of the CO_2 molecule. The plotted atom size represents the 10% probability sphere of the freely refined displacement parameter. c) Expected potential map (same settings) based on calculated structure factors. The offset between the maximum density and the guest molecule is an artefact of the data set, most probably related to the limited completeness.

Table 24: Atomic positions and U_{iso} / U_{eq} parameters for the CO_2 absorbed CHA structure.

Atoms	Occ.	*x*	*y*	*z*	U_{iso} / U_{eq} (Å^2)
Na1	0.4	0	0	0.1746(15)	0.032(3)
K1	0.6	0	0	0.2346(5)	0.0318(13)
Cs1	0.750(3)	0.5	0	0	0.136(2)*
Si1	0.6458(7)	0.22992(7)	0.00113(8)	0.10591(9)	0.0028(2)
Al1	0.3542(7)	0.22992(7)	0.00113(8)	0.10591(9)	0.0028(2)
O1	1	0.26378(13)	0	0	0.0259(7)
O2	1	0.19732(15)	0.09866(7)	0.1241(2)	0.0109(5)
O3	1	0.11862(8)	-0.11862(8)	0.1326(3)	0.0230(7)
O4	1	0.3333	0.01497(14)	0.1667	0.0199(6)
CO_2	**Occ.**	**x**	**y**	**z**	**Uiso (Å^2)**
O100	1	0.1667	0.0833	0.3333	0.051(3)
C100	1	0.1667	0.0833	0.4104	0.227(14)
O101	1	0.1667	0.0833	0.4875	0.40(3)

***ADP harmonic parameters**

Cs1	0.0981(10)	0.297(3)	0.080(4)	0.1484(14)	-0.0613(14)	-0.123(3)

Table 25: Inter-atomic distances (Å) for the CO_2 absorbed CHA structure.

Framework		Mult.	Extra-framework		Mult.	CO_2 molecule		Mult.
Si1-Si1	3.195(2)	1	Na1-Si1	3.335(7)	6	Si1-C100	3.43(2)	1
Si1-Si1	3.0811(15)	1	Na1-O2	2.481(7)	3	Cs1-O100	3.078(9)	4
Si1-Si1	3.1900(11)	1	Na1-O3	2.908(5)	3	Cs1-C100	3.144(18)	4
Si1-Si1	3.145(2)	1	K1-O2	2.888(5)	3	Cs1-O101	3.46(2)	4
Si1-O1	1.6667(15)	1	K1-O3	3.227(4)	3	K1-O100	2.606(13)	6
Si1-O2	1.643(2)	1	Cs1-O1	3.2644(18)	2	K1-C100	3.396(18)	6
Si1-O3	1.6477(15)	1	Cs1-O3	3.242(4)	2	Na1-O100	3.22(2)	6
Si1-O4	1.6270(13)	1	Cs1-O4	3.4845(8)	4			

Table 26 : Crystallographic details of data reduction and dynamical refinement.

Chemical formula	$Na_{2.4}K_{3.6}Cs_{6.74(3)}Al_{12.74}Si_{23.26}O_{72}(CO_2)_8$
Temperature	100 K
Crystal system, space group	Trigonal, *R*-3*m*
Twin law	$\begin{pmatrix} -1 & 0 & 0 \\ 0 & -1 & 0 \\ 0 & 0 & 1 \end{pmatrix}$
a, *b*, *c* (Å)	13.7696, 13.7696, 15.039
V (Å³)	2469.4
Z	1
Electron wavelength λ (Å)	0.0335
Number of frames	190 (from 7 data sets)
Tilt step (°)	1.0
Precession angle (°)	1.0
$\sin(\theta_{max})/\lambda$	0.70
Completeness (%)	83.6
No. of measured, observed[$I>3\sigma(I)$] reflections	6661, 32547
No. of refined parameters, restraints, constraints	289, 0, 12
Min./Max. residual electrostatic potential (e/Å³)	0.31, -0.45
R(obs), *wR*(obs), *R*(all), *wR*(all)	0.110, 0.099, 0.381, 0.124

III. Conclusion

In this section various topics have been treated: from the structural study of nanosized CHA, up to the localization of the CO_2 into the cages of the zeolite thanks to 3D electron diffraction. Finally, the CO_2 adsorption study in the ion exchanged samples by infrared spectrometry was performed.

The synthesis strategy outlined in chapter 3 is a new and a simple procedure to prepare CHA with a size of 30 to 80 nm. Nanosized CHA was characterized using *in-situ* FTIR analysis in the presence of CO_2. The CO_2 adsorption isotherms on the as-prepared samples gave comparable CO_2 adsorption capacity to the related materials already reported in the open literature. The ion exchange CHA samples were subjected to CO_2 adsorption studies too in order to evaluate the effect of extra-framework cations. At least 2 different adsorption sites of

CO_2 in the *CHA* cage were revealed in all adsorbents. High interaction of CO_2 with negative framework oxygens leads to the formation of carbonates in the case of as-synthesized sample r2.5-CHA and the Cs-CHA. The high formation of carbonates is due to the low acidity of the Cs^+. However, the as-prepared sample r2.5-CHA adsorbs higher amount of CO_2 than the Cs-CHA. The Na-CHA sample showed the highest adsorption capacity at 121kPa CO_2 and the highest amount of physisorbed CO_2. The evolution of FTIR spectroscopy in function of time gave information regarding the kinetics of the CO_2 adsorption on sample r2.5-CHA. This analysis indicated that the adsorption is very fast and needs a few minutes to reach the saturation.

The adsorption and desorption of CO_2 on nanosized CHA zeolite was repeated in 10 subsequent cycles; the process under CO_2 flow (40mL/min) was followed by TG. The regenerability of the material was demonstrated (Figure 49). The high stability and high capacity of the nanosized CHA zeolite for CO_2 were verified. After 10 cycles, the high crystallinity of the nanosized CHA zeolite and the capacity of the towards CO_2 adsorption were fully preserved.

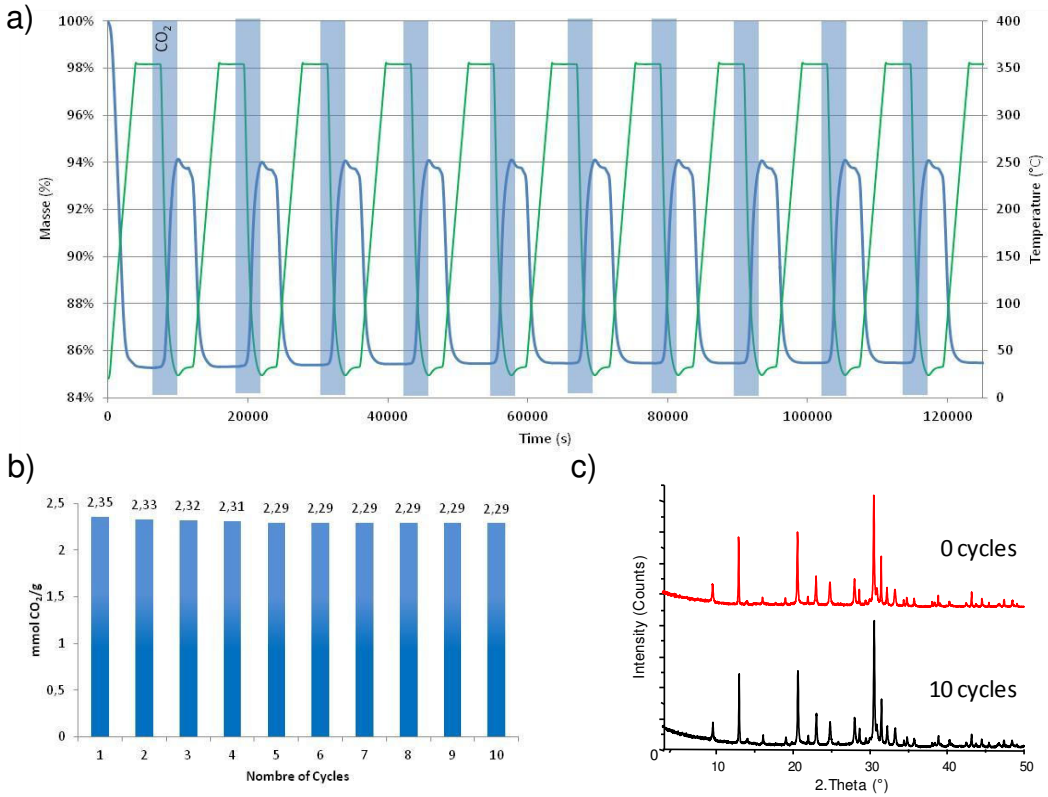

Figure 49: Multicycle adsorption of CO_2. (a) TG analysis of nanosized CHA zeolite subjected to 10 subsequent sorption cycles of CO_2: temperature variation (green line) and variation of CO_2 concentration (blue rectangles); (b) CO_2 capacity of CHA zeolite in 10 cycles; (c) PXRD patterns of CHA zeolite before and after 10 cycles of CO_2 adsorption.

Finally, we demonstrated that the nanosized CHA zeolites are:

- Selective toward CO_2/CH_4 and CO_2/N_2
- Comparable with current zeolites regarding the capacity of CO_2 adsorption
- Partially regenerable under vacuum (totally at 200 °C)
- Nanosized crystals with importance for further application (preparation of membranes)
- No use of organic templates (environmentally benign synthesis)
- Stable nanosized template free zeolite up to 800 °C

CHAPTER 5: TEMPLATE-FREE SYNTHESIS OF FLEXIBLE RHO-TYPE NANOZEOLITES

The RHO-type zeolite is one of the so-called flexible zeolites, it has 3-dimensional pore system combining LTA cages linked by 8-membered rings doors.[36] This zeolite has promising catalysis and gas separation applications[47] such as NOx removal,[130] MTO reactions,[131] and CO_2/CH_4 separation.[89,132] Its selectivity comes from the combination of their narrow pore sizes (3.6 Å) and the introduction of different extra-framework cations such as Na^+, Cs^+.[81] Depending on the nature of the molecule, the extra-framework cations can selectively block its access to pores and cages of the zeolite. This phenomenon, still under investigation, is named either "trap-door effect"[79] or "swing effect".[90] In addition, it induces a structural change of the RHO-zeolite framework upon gas adsorption, temperature or ion-exchange.[51,133–135]

Herein, we report on the synthesis of nanosized flexible RHO-type zeolites without the assistance of an expensive OSDA or seeding approach. Only alkali metal hydroxides, namely NaOH and CsOH, are needed to obtain pure nanocrystals of RHO having a size below 100 nm and a high content of cations. Their framework structure and counter cations positions have been determined by Rietveld refinement based on powder X-ray diffraction (PXRD) patterns. Interestingly, in-situ PXRD measurements upon dehydration permitted to follow and quantify the distortion of the D8R as well as the displacement of Na^+ and Cs^+ cations within the cages.

The synthesis of RHO is detailed in the Chapter 2. The resulting clear aqueous suspension had the following molar composition:

$$10\ SiO_2 : 0.8\ Al_2O_3 : 8\ Na_2O : 0.58\ Cs_2O : 100\ H_2O$$

The clear aqueous suspension was then aged for 14 hours at room temperature. Then, the hydrothermal crystallization was conducted at 90 °C for 1 h to obtain RHO nanozeolite. The solid was separated and recovered by high-speed centrifugation (20000 rpm, 10 min) and washed until the pH of the remaining water was about 7.5.

I. Characterisations

At first, a whole profile matching of the PXRD patterns was performed considering the *I*-43*m* space group with *a* = 14.8118(1) Å. The structure was then solved *using* the SUPERFLIP program in order to localize the Na^+ and Cs^+ cations in the structure. All the atomic positions and isotropic displacement parameters (*Uiso*) were refined. The oxygen atoms of the water molecules were localized from Fourier difference maps. The final reliability factors obtained after the last refinement cycle of the structures are: R_{obs} = 4.87% and Rwp = 4.80% (see Figure 50 for the corresponding PXRD fit).

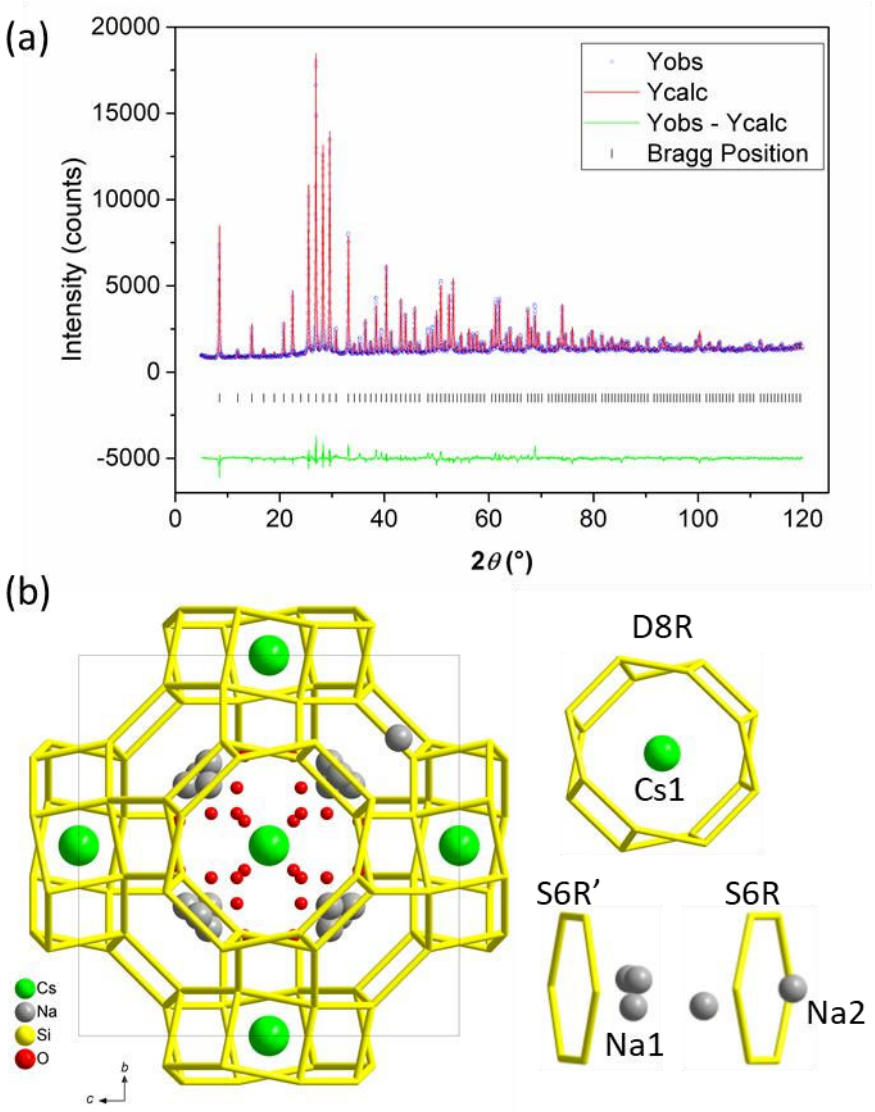

Figure 50: (a) Rietveld refinements of PXRD pattern of the nanosized Na,Cs-RHO(H_2O). (b) Views of the RHO framework with localized Cs^+, Na^+ cations and O atoms of the water molecules.

The average size of the crystallite calculated from the Rietveld refinements is 57(1) nm which is in a good agreement with the SEM analyses. Similarly, the composition of the RHO sample (assuming a O_{96} stoichiometry) determined by Rietveld refinement, ICP analysis or Energy dispersive X-ray Spectrocopy (EDS) are in the same range:

$$\text{EDS: } Na_{13.7}Cs_{6.5}Si_{27.6}Al_{20.4}O_{96}$$

$$\text{ICP: } Na_{13.4}Cs_{6.0}Si_{28.5}Al_{19.5}O_{96}$$

$$\text{DRX: } Na_{13.1}Cs_{5.2}Si_{29,7}Al_{18,3}O_{96}$$

The slight differences between those analyses may arise from the difference of sensitivity of the used technics and also a possible inhomogeneity of the chemical composition of crystallites in the sample.

The Rietveld refinement confirms that the preferential position for Cs^+ is the centre of the D8R while Na^+ and water molecules are located in the *lta* cages (outside the S6R). The RHO zeolites are well known for their framework flexibility with large rearrangements. In our case, the structure of the Na,Cs-RHO-1 was refined in the acentric *I*-43*m* cubic space group instead of the "ideal" centric *Im*-3*m* space group to take into account the elliptical distortion of the double 8-rings. According to Parise et al.[136], the distortion or ellipticity of the D8R can be evaluated by the parameter Δ. This parameter corresponds to the distance O1-O2 projected on the (001) plane, i.e. to the difference divided by two between the biggest and the smallest O-O distances in the D8R's cross-section (Figure 50). For our RHO material $Na_{13.1}Cs_{5.2}(Si_{29.7}Al_{18.3}O_{96})(H_2O)_{41}$, the obtained Δ value (1.87 Å) is slightly larger than the one reported for $Na_{6.2}Cs_{3.2}(Si_{36.4}Al_{11.6}O_{96})(H_2O)_{6.2}$ by Baur[137] with Δ = 1.57 Å. According to Corbin et al.[135] the degree of distortion is related to the charge density of the cation, located in the D8R. In our case the occupancy rate of Cs^+ at the centre of the D8R is larger than the one reported by Baur.[137] By lowering the Si/Al ratio, we increased the number of compensating cations which have a direct influence on the D8R distortion, like temperature, ion-exchange and/or adsorption. TD-PXRD experiments performed here indicate that the amount of water present in RHO do also affect strongly the flexibility of RHO structure. This influence is evidenced by the strong variation of the unit cell parameters under N_2 flow when going from RT to 350 °C (from 14.810 Å to 14.778 Å) resulting in a decrease of the cell volume from 3248.5 to 3227.2 $Å^3$.

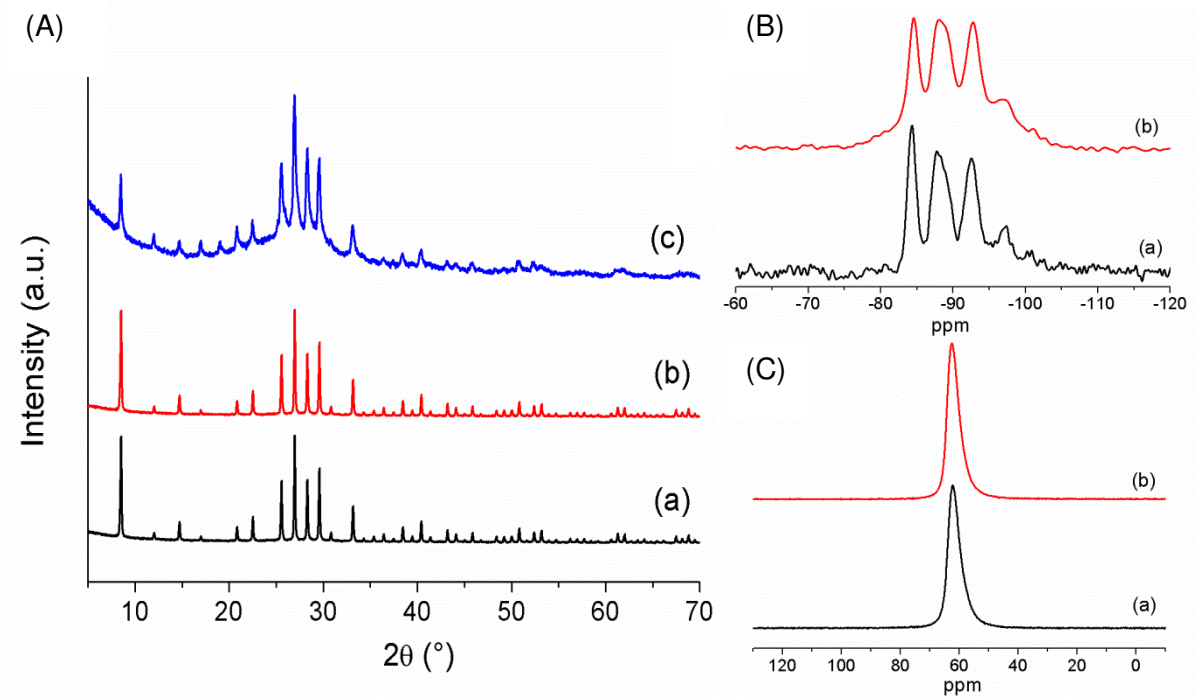

Figure 51: (A) Powder XRD patterns of RHO-type sample (a) as-prepared and after calcination at (b) 550 °C and (c) 650 °C in the range of 5-70 degrees; (B) ^{29}Si NMR and (C) ^{27}Al NMR of RHO-type zeolite of (a) as-prepared and (b) after calcination at 550 °C.

Having a zeolite with such a low Si/Al ratio of 1.5 brings questions on both thermal stability and presence of extra-framework alumina species. Only Bragg peaks corresponding to RHO are present in all patterns, as-prepared and after *ex-situ* calcination at 550 °C and 650 °C (Figure 51a). Amorphization of the sample is only observed after the 650 °C treatment (Figure 51c). The thermal stability of the RHO-type zeolite has been further confirmed up to 550 °C by NMR since no disturbance has been observed in ^{29}Si and ^{27}Al MAS NMR spectra (Figure 51c). Single peaks corresponding to aluminium in a tetrahedral position can be observed at around 60 ppm respectively. No peak corresponding to octahedral aluminium was observed at 0 ppm. Peaks corresponding to Q^0 (4Al), Q^1(3Al), Q^2(2Al), Q^3 (1Al) and Q^4 (0Al) types of silicon tetrahedrons can be observed at around -84 ppm, -88 ppm, -92 ppm, -98 ppm and -102 ppm respectively (Figure 51). After being normalized with the mass of material samples, those peaks have been deconvoluted and their respective areas allowed the calculation of molar Si/Al ratio of RHO-type zeolite materials: 1.50. The other analysis, EDS, ICP analysis and PXRD refinement, confirmed this molar Si/Al ratio with an average value of 1.47.

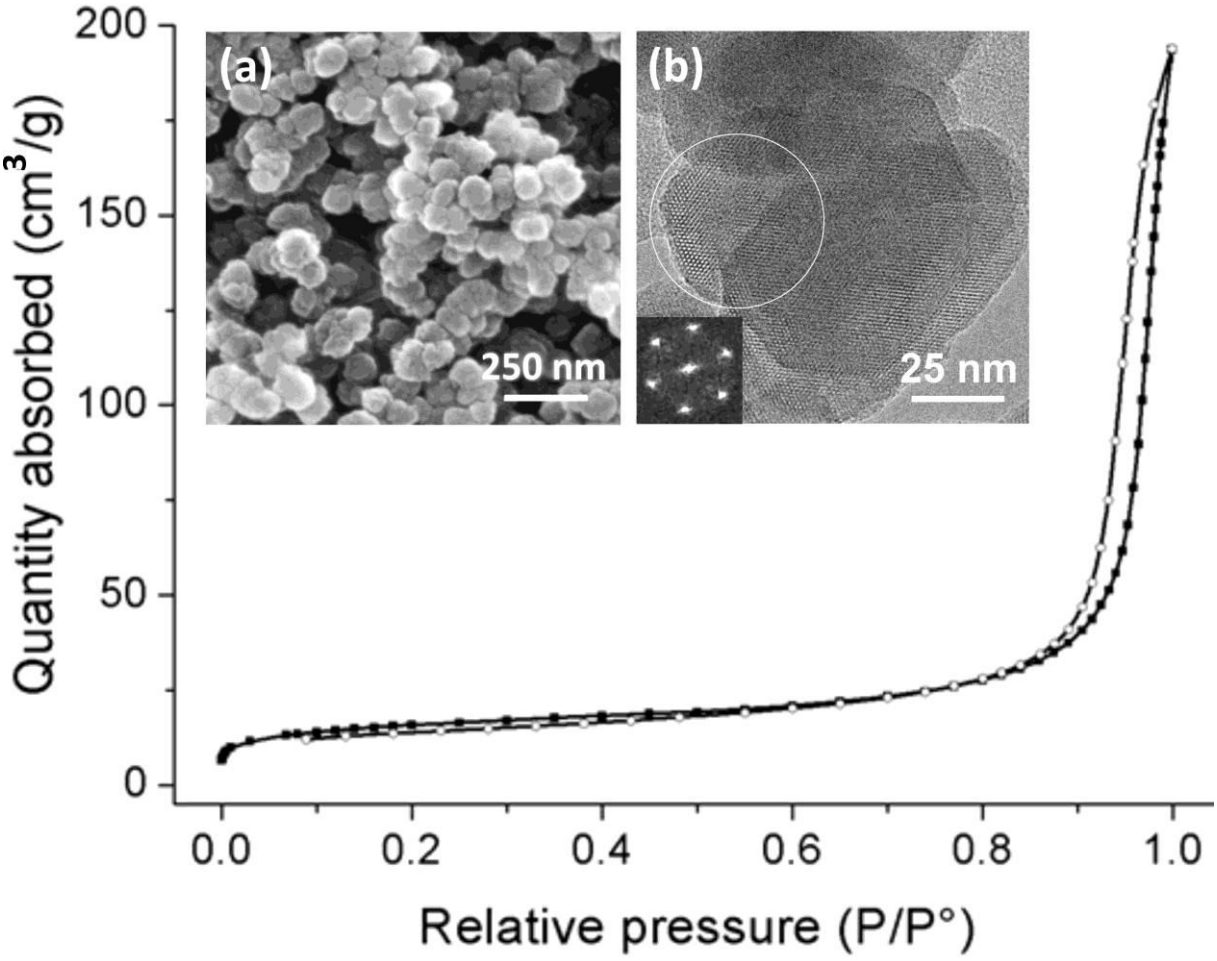

Figure 52: Nitrogen adsorption-desorption isotherm of nanosized RHO-type zeolite (closed symbols: adsorption and open symbols: desorption). Insert: Nanosized RHO-type zeolites images captured by (a) FE-SEM and (b) TEM. In (b), the Fourier transform from the area encircled in white corresponds to a [111] oriented crystal (SG: I-43m).

SEM and TEM images revealed the presence of nanocrystals having a size below 100 nm (Figure 52). As excepted very low microporosity is measured as a polar molecules such as N_2 are not able to enter the micropores being blocked by the extra framework cations (Na^+, Cs^+). Nevertheless, the substantially high total pore volume is explained by the high external surface area due to the nanometer size of the crystals, especially when compared to the nitrogen adsorption-desorption isotherms obtained with a micron-sized aggregated material.

II. Structural changes of RHO nanozeolite upon dehydration

The RHO-type nanocrystals were subjected to heat treatment in order to desorb water from the cages: a heating with a ramp from 30 °C to 300 °C and cooling back to 30 °C have been conducted and monitored by recording PXRD patterns every 30 °C (Figure 53) in air and under nitrogen.

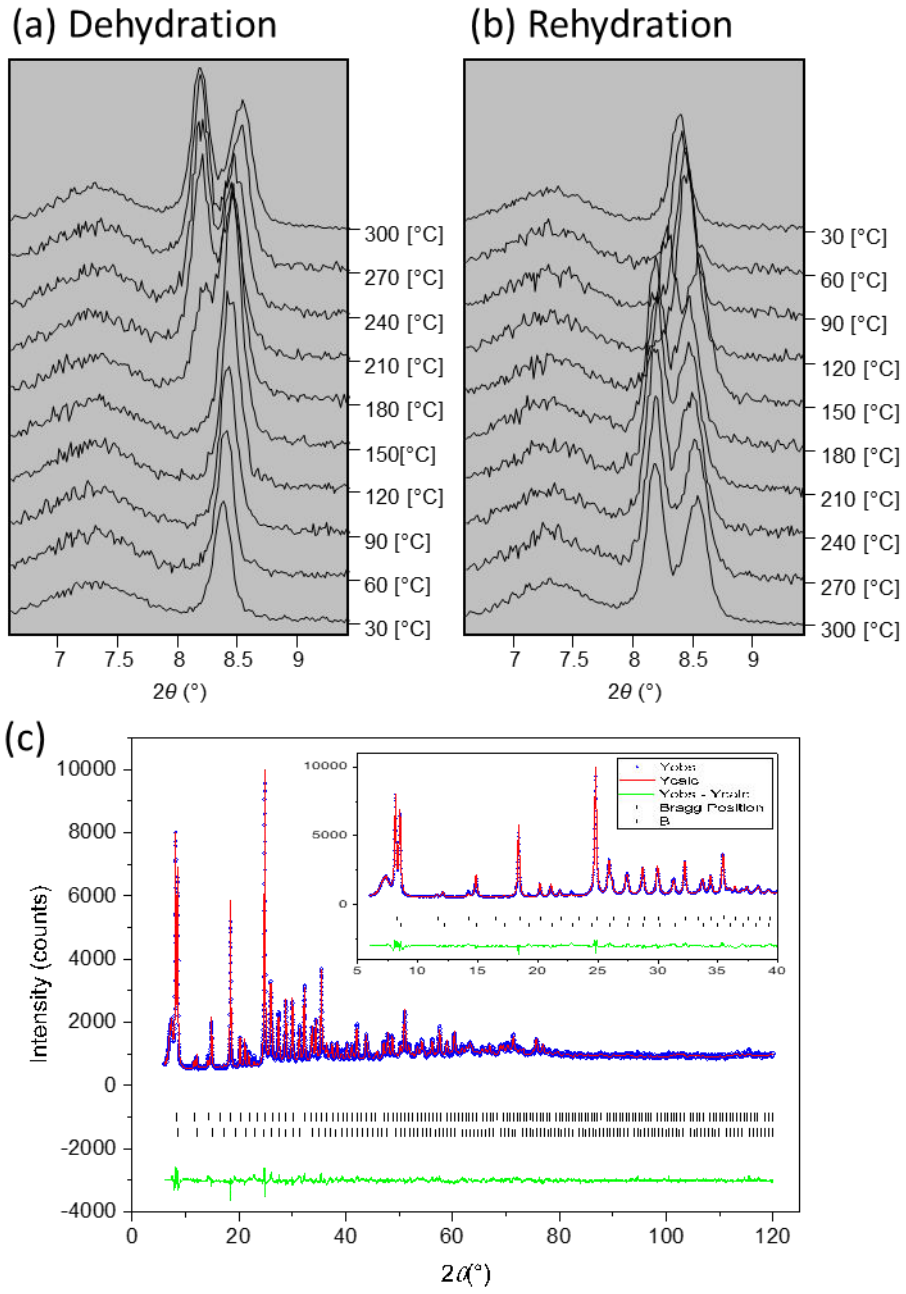

Figure 53: *In-situ* PXRD patterns of RHO-type nanozeolite recorded in air upon heat treatment (a) from 30 to 300 °C, and upon cooling (b) from 300 to 30°C; (c) Rietveld refinement of PXRD pattern collected at 350°C under N_2 atmosphere.

The most striking feature observed in our TD-PXRD experiments is the splitting of the high intensity peak at about 8° (2θ). Overall, a fully reversible dehydration has been observed as the splitting of the peak observed at 180 °C, disappears at 120 °C during cooling. For RHO type material, dehydration is usually accompanied by an enlargement of the cubic unit-cell related to a structural change from a distorted D8Rs (*I*-43*m* acentric space group) to a regular D8Rs (*Im*-3*m* centrosymmetric space group). This phenomenon was also observed during the study of RHO type materials under very high pressure[138] or during the adsorption

of CO_2.[81] This enlargement of the unit-cell can be easily observed on the PXRD patterns since it corresponds to the shift of the first main peak (101), around 8.5°(2θ), towards the high angles. In our case (Figure 53), the peak (101) splits in two above 120°C. These two peaks remain present up to 300°C. A complementary PXRD experiment performed until 440°C showed that there is no evolution of the positions and intensities between 270 and 440°C for the (101) peak. Initially, we assumed incomplete dehydration at 300°C. However, TGA analyses show complete dehydration above 200 °C. We also supposed that the splitting of the peaks could be due to a lowering of the symmetry. Nevertheless, the diffraction peaks above 120°C can only be indexed by two RHO cubic unit-cell with parameters a = 15.1603(3) Å and a = 14.5179(5) Å (for T = 350°C). It shows that two different dehydrated RHO structures are cohabiting at high temperatures instead of one after rehydration at low temperatures.

According to Parise et al.[136] the decreasing of the unit-cell parameter must correspond to an increasing of the elliptical distortion of the D8Rs and the structure stay in the acentric I-43m symmetry. Inversely, with the enlargement of the unit-cell, the D8Rs must become regular and the structure can be described in the centric space group Im-3m. From those considerations, we first solved and refined both structures considering the Im-3m space group for Na,Cs-RHO-1 with the largest unit-cell and the I-43m space group for Na,Cs-RHO-2 with the smallest unit-cell. We obtained the following figures of merit: Robs-1 = 6.38%; Robs-2 = 6.32 % and Rwp = 5.37%. This result was not satisfactory and an alternative choice was tested where both structures are treated using the I-43m space group. This actually leads to a better fit of the PXRD patterns with Robs-1 = 4.39%; Robs-2 = 4.31 % and Rwp = 4.39%. The different parts of both RHO frameworks are shown in Figure 54. The chemical composition for Na,Cs-RHO-1 and Na,Cs-RHO-2 determined from the Rietveld refinements are Na7.4Cs11.0(Si29.6Al18.4)O96 and Na13.5Cs2.6(Si31.9Al16.1)O96 with the following mass concentration 49(1) and 51(1)%, respectively. The crystallite sizes also determined from the Rietveld refinements are slightly larger than the one of Na,Cs-RHO(H_2O), with 71(2) nm for Na,Cs-RHO-1 and 68(2) nm for Na,Cs-RHO-2. As can be seen on Figure 54, there are big differences between both structures. An increase of the elliptical distortion of the D8Rs from Δ = 1.57 Å for Na,Cs-RHO(H_2O) to Δ = 2.16 Å for Na,Cs-RHO-2 was measured. This value is comparable to the one calculated for the pure Na-RHO reported by Lozinska et al.[81] with Δ = 2.10 Å for a unit-cell parameter a = 14.4139(2) Å. The structure Na,Cs-RHO-2 appears as similar to the hydrated structure Na,Cs-RHO(H_2O) obtained here and similar to dehydrated structure found in literature.[134] Indeed, both Cs+ and Na+ cations may fit in the same positions as in the hydrated form, inside the D8R and outside the S6R, respectively. Nevertheless, the amount of Cs+ in sample Na,Cs-RHO-2 is reduced compare

to the as synthesized material Na,Cs-RHO(H_2O). On the D8R the occupancy of Cs+ decreased from 0.863 to 0.323. A small but significant amount of Cs+ is also present in the Na1_2 S6R. On the other hand, the increasing of the unit-cell parameter for Na,Cs-RHO-1 to 15.1603(3) Å corresponds to a decreasing of the elliptical distortion with Δ = 0.94 Å. It's worth noting, that this is the larger unit-cell parameter ever reported for the RHO structure. We can also observe that in Na,Cs-RHO-1 the amount of Cs^+ cation increase compare to the as synthesized phase Na,Cs-RHO(H_2O) from 5.2 to 11.0 Cs^+ per unit cell. Such amount of Cs^+ cannot stay in the central D8R position. The Cs^+ cations could move out from the D8R. This ability of the Cs^+ cations in the RHO structure to displace in and out of the D8Rs is the foundation of the trapdoor effect that is the base of the selective adsorption capacity of the RHO zeolites. The opposite displacement was observed for the Na^+ cations, from outside to inside S6R. From the overall structure, it seems that all Cs^+ and Na^+ cations are inside the *lta* cages replacing water molecules and stabilized the overall framework.

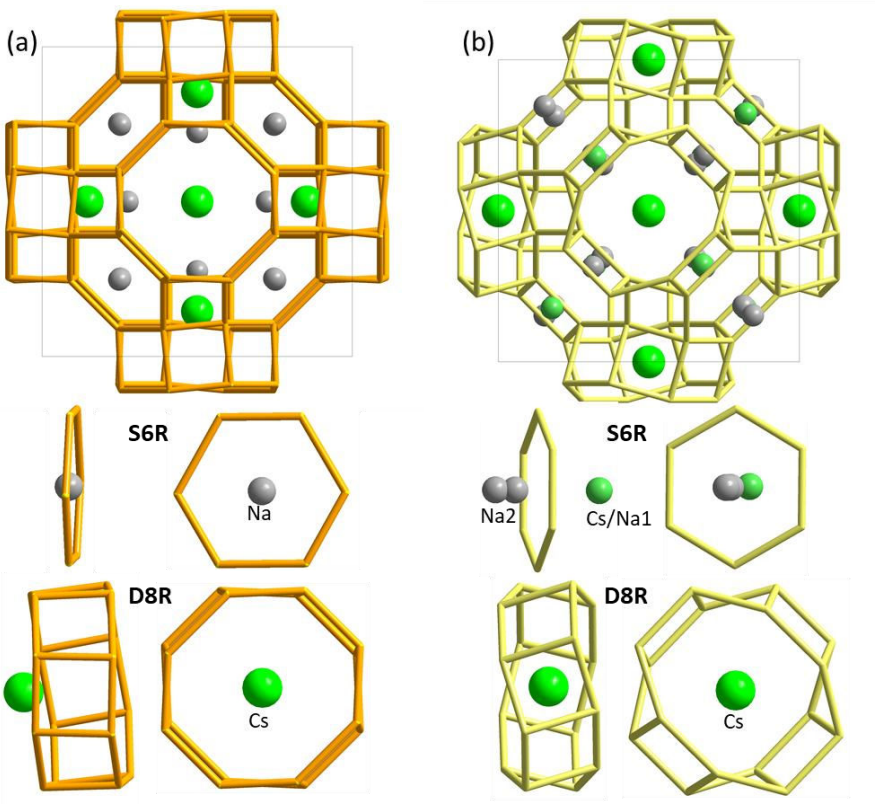

Figure 54: Views of the RHO framework structures Na,Cs-RHO-1 and Na,Cs-RHO-2 obtained after dehydration of the Na,Cs-RHO(H_2O) nanozeolite.

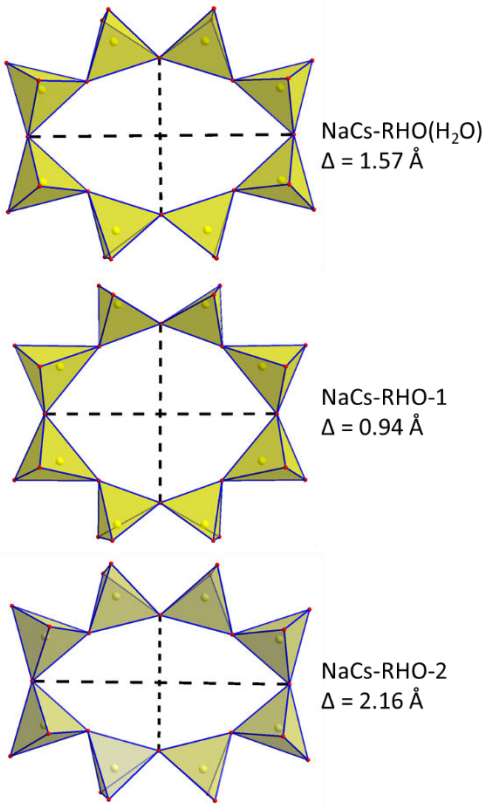

Figure 55: Evolution of 8-rings elliptical distortion, from the Na,Cs-RHO(H_2O) nanozeolite to the dehydrated Na,Cs-RHO-1 and Na,Cs-RHO-2 samples. The Δ parameter represents the difference between the two O-O distances presented by doted lines divided by 2.

After rehydration at room temperature, we obtained a PXRD pattern identical to the first one recorded for the as-synthesized hydrated Na,Cs-RHO(H_2O) sample. This means that the structural model we proposed for this latter corresponds to an average structure between two hydrated structures with identical unit-cell parameters, but with slightly different chemical compositions, and different Cs^+ / Na^+ distributions.

The agreement indices for the final least-squares cycles of the refinements and the refined cell constants are reported in Table 27. Furthermore, Table 28 reports the refined structural data of the framework and extra-framework content of Na,Cs-RHO-1, Na,Cs-RHO-2 and Na,Cs-RHO(H_2O).

Table 27: Details of PXRD data and Rietveld refinements for RHO zeolites.

Diffractometer	Bruker D8 advance vario1		
Radiation (Å)	Cu-Kα_1 radiation λ = 1.5406		
Compound	Na,Cs-RHO(H2O)	Na,Cs-RHO-1	Na,Cs-RHO-2
Formula	$Na_{13.1}Cs_{5.2}Si_{29.7}Al_{18.3}O_{96}(H_2O)_{41}$	$Na_{7.4}Cs_{11.0}Si_{29.7}Al_{18.3}O_{96}$	$Na_{13.2}Cs_{2.6}Si_{29.7}Al_{18.3}O_{96}$
2θ-range / step (°)	5 – 119.996 / ~0.014	10 – 126.181 / ~0.012	10 – 126.181 / ~0.012
Temperature (°C)	20	350	350
Space Group	$I\bar{4}3m$ (217)	$I\bar{4}3m$ (217)	$I\bar{4}3m$ (217)
Z	1	1	1
a /Å	14.8118(1)	15.1601(3)	14.5179(4)
V /Å^3	3249.57(7)	3484.24(11)	3059.91(15)
Molar mass (g.mol^{-1})	4525.6	4519.2	3506.2
Rietveld refinement			
Shape	Lorentzian	Lorentzian	
Background	10 Legendre polynoms	10 Legendre polynoms	
Asymmetry	Fundamental approach	Fundamental approach	
Rietveld agreement factors			
R_{Fobs}	0.0487	0.0429	0.0431
R_{Bobs}	0.0870	0.0601	0.0728
*Rw*p	0.0480	0.0439	
*cR*wp	0.1325	0.1381	
Gof	1.85	1.44	

Table 28: Atomic positions and U_{iso}-*eq* parameters for the different RHO structures

Phase / Atoms	Wyckoff	Occ	*x*	*y*	*z*	$U_{iso,eq}$ (Å^2)
Na,Cs-RHO(H_2O)						
Na1	24g	0.3333	0.1590(5)	0.2172(7)	0.1590(5)	0.038
Na2	8c	0.638(10)	0.1850(5)	0.1850(5)	0.8150(5)	0.038
Cs1	6b	0.863(3)	0.5	0	0	0.045214
Si1	48h	1	0.61976(11)	0.22924(11)	0.07959(11)	0.0109(4)
O1	24g	1	0.6283(3)	0.1282(3)	0.1282(3)	0.0188(13)
O2	24g	1	0.1038(5)	0.2826(3)	0.7174(3)	0.038(2)
O3	48h	1	0.6178(3)	0.2094(3)	-0.0299(3)	0.0187(13)
O4 (water)	24g	1	0.2366(4)	0.0646(3)	0.0646(3)	0.038
O5 (water)	24g	0.7021	0.1521(5)	0.0845(4)	-0.0845(4)	0.038
Na,Cs-RHO-1						
Na1	8c	0.847(18)	0.2479(15)	0.2479(15)	0.2479(15)	0.036866
Na2	12e	0.054(12)	0.2243	0	0	0.037995
Cs1	12e	0.918(6)	0.3543(2)	0	0	0.144(2)
Si1	48h	1	0.3906(3)	0.2456(4)	0.0893(3)	0.0312(16)
O1	48h	1	0.4909(4)	0.2871(4)	0.1201(5)	0.0195(19)
O2	24g	1	0.6293(7)	0.1481(6)	0.1481(6)	0.0195(19)
O3	24g	1	0.3924(9)	0.1921(6)	0.1921(6)	0.0195(19)
Na,Cs-RHO-2						
Na1	8c	0.920(5)	0.1777(6)	0.1777(6)	0.1777(6)	0.122
Cs1	8c	0.080(5)	0.1777(6)	0.1777(6)	0.1777(6)	0.122
Na2	8c	0.22(3)	0.154(4)	0.154(4)	0.846(4)	0.051
Cs3	6b	0.323(4)	0	0	0.5	0.072
Na4	8c	0.50(4)	0.1857	0.1857	0.8143	0.037995
Si1	48h	0.6	0.2770(3)	0.1256(3)	0.4293(3)	0.0176(11)
Al1	48h	0.4	0.2770(3)	0.1256(3)	0.4293(3)	0.0176(11)
O1	48h	1	0.0397(3)	0.2071(3)	0.3897(6)	0.016(2)
O2	24g	1	0.2211(5)	0.2211(5)	0.4051(8)	0.016(2)
O3	24g	1	0.1158(5)	0.1158(5)	0.6273(9)	0.016(2)

III. Use of the nanosized RHO zeolite for CO_2 adsorption

The adsorption of CO_2 in Na,Cs-RHO zeolite was studied. The sorption isotherms were recorded at different concentrations of CO_2 (up to 121 kPa) which corresponds to relative pressure of 0.35 P/P° due to instrument limitations. All sorption isotherms are described with a Langmuir shape until P/P° = 0.01 followed by a nearly linear trend up to P/P° = 0.03. It has been calculated that at the highest pressure reached and RT, the material absorbed about 1.56 mmol/g CO_2 (Figure 56).

The TG analysis confirmed that 8.70% CO_2 was absorbed in the Na,Cs-RHO(H_2O) zeolite at 1 bar and RT, which corresponds to 2.01 mmol of CO_2 per gram of zeolite.

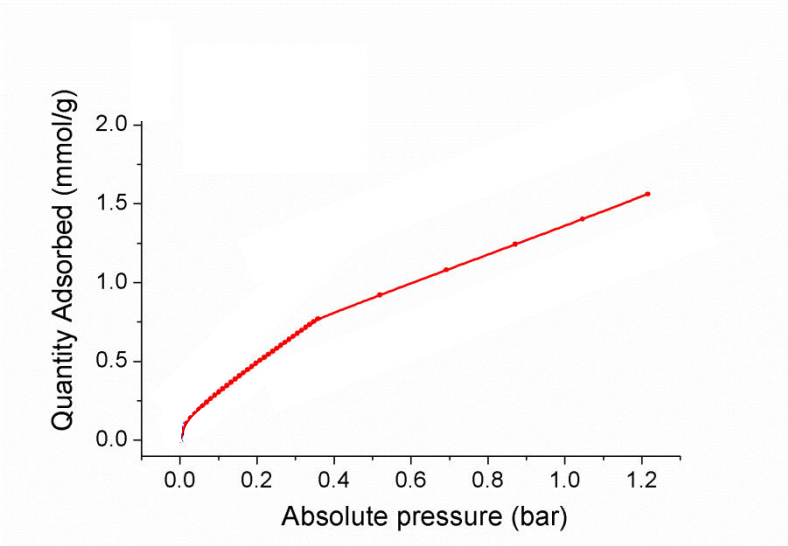

Figure 56: CO_2 sorption isotherm on RHO nanosized zeolite.

In Figure 57a, 10 consecutive cycles of CO_2 adsorption at 1 atm followed by desorption at 350 °C has been performed and monitored by the FTIR (the area of the bands attributed to physisorbed and chemisorbed CO_2 were measured). The adsorption capacity of nanosized Na,Cs-RHO is not perturbed even after 10 cycles as the band areas (red color) reached the same level (around 6) in all cycles. In addition, this adsorption appeared fully reversible as the band area after 350 °C desorption (blue color) always reached back the initial reference point (blue triangle point). The Figure 57b confirms that the adsorption capacity of RHO zeolite material is preserved during the 10 cycles of CO_2 adsorption at 1 bar followed by desorption at 350 °C monitored by TGA. Finally, no crystalline loss was observed by PXRD after the consecutives cycles either monitored by FTIR (Figure 57c) or TGA (Figure 57d), meaning that the nanosized Na,Cs-RHO zeolite is stable under CO_2 sorption cycles.

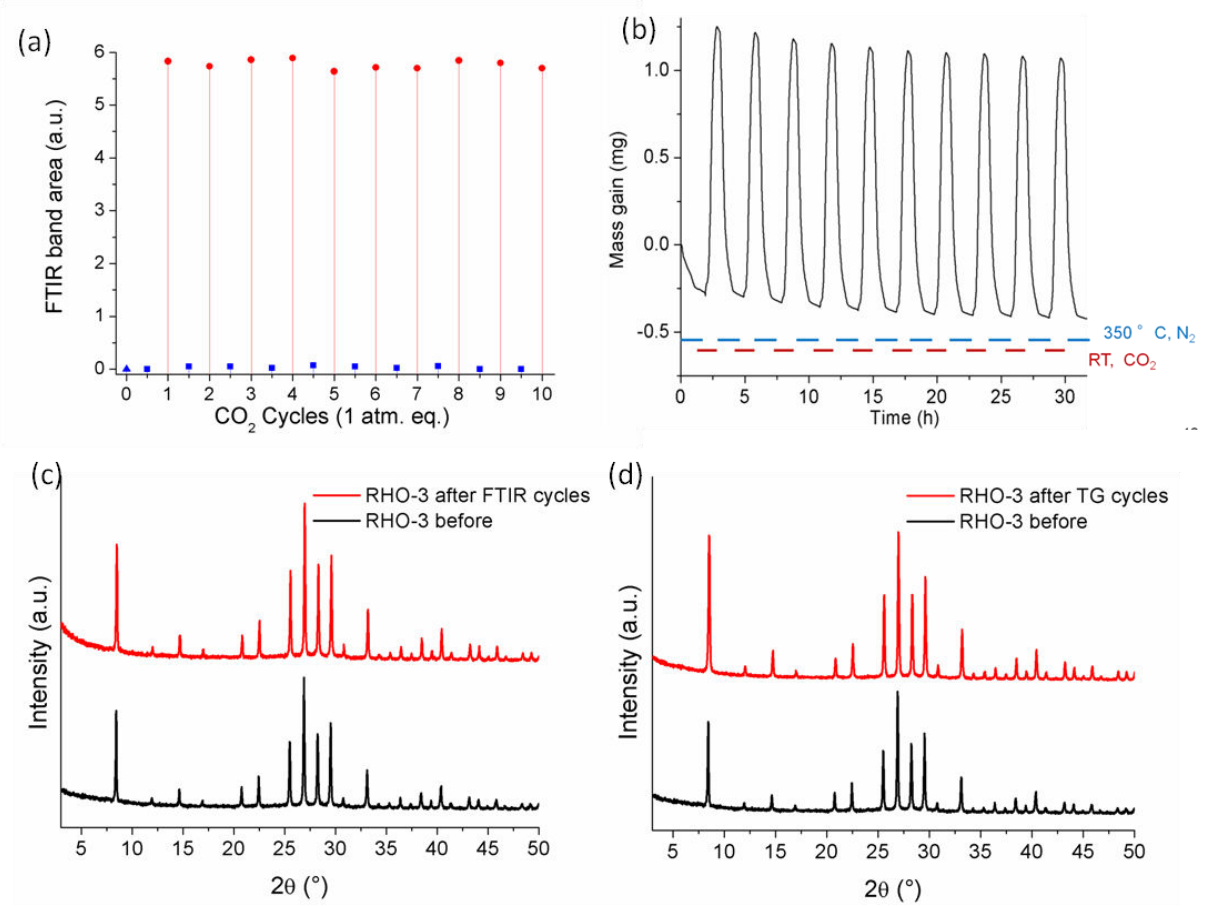

Figure 57: Sorption of CO_2 adsorption (red color) and desorption at 350 °C (blue color) on nanosized RHO zeolite recorded by FTIR (a) and TGA (b). The stability of the nanosized RHO zeolite after 10 sorption cycles (red color) was determined by PXRD (c) and TGA (d) analyses.

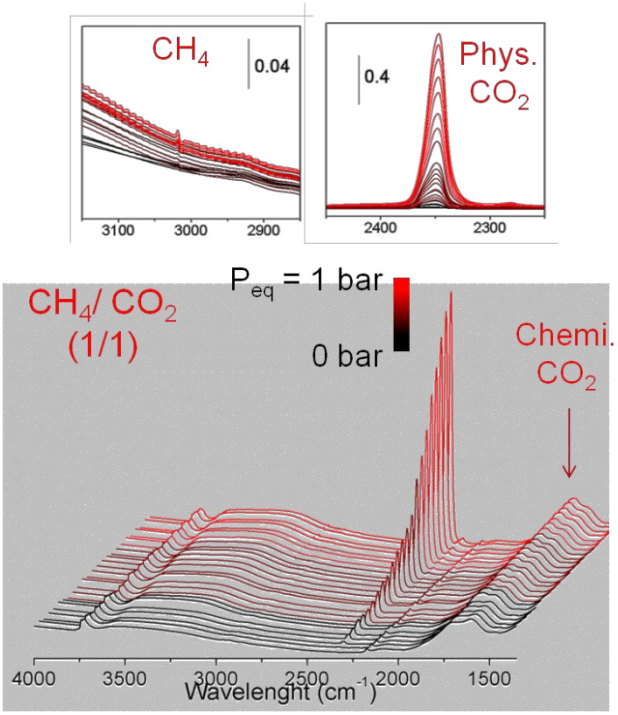

Figure 58: IR spectra of CO_2 and CH_4 adsorbed on RHO nanozeolite.

The detection of a mixture of CO_2 and CH_4 (1/1 in volume) gases up to 1 bar with the nanosized RHO zeolite was studied. The nanosized RHO zeolite was prepared as a self-supported pellet and the detection was followed by in situ FTIR spectroscopy (Figure 58).

The CO_2 physisorbed (band at around 2650 cm^{-1}) and chemisorbed (bands at around 1650 cm^{-1} due to the formation of carbonates) were clearly measured. This CO_2 adsorption is fully reversible and the CO_2 is desorbed at 150°C under vacuum. At the same time, no CH_4 adsorption was observed (the band at 3050 cm^{-1} was not measured).[139]

IV. Conclusion

Flexible small pore RHO-type nanosized zeolite has been prepared without any expensive organic structure directing agent; the size of the nanocrystals is below 100 nm. The cross-determined Si/Al atomic ratio (NMR, ICP, EDS, PXRD) is 1.50. The high content of Cs cations stabilized the RHO structure; the material is thermally stable up to 550 °C. *In situ* PXRD study proved the reversible window cage flexibility upon dehydration. Two different phases have been refined showing different behaviour upon dehydration according to their diverse chemical composition and different Cs^+/Na^+ cationic distributions over the RHO framework. The comparison of the two structures also shows the ability of the Cs^+ cation to displace in and out from the D8Rs. This displacement is the base of the trap door effect which is explaining the selective adsorption capacity of the RHO zeolites. The CO_2 capacity and selectivity for CH_4 in the RHO-type nanozeolites was studied.

CHAPTER 6: GENERAL CONCLUSIONS AND OUTLOOK

In this thesis, a range of different types of potential CO_2 adsorbents have been synthesized and tested. In order to find a good potential adsorbent for CO_2 separation, different structures have been examined. The CHA and RHO type zeolites have shown comparable potential for gas separation application. Both zeolites were synthesized with nanosized crystals from organic template free precursor suspensions. CHA zeolite nanocrystals were prepared by direct synthesis approach as well as by transformation from FAU micronsized crystals under post-synthesis treatment.

The use of inorganic cations as structural directing agents (Cs^+, Na^+, K^+) was explored in this work. Nanosized CHA zeolites with a particle dimensions of 30-300 nm as single crystals and as agglomerates were prepared by changing the alkalinity of the final precursor suspensions and the sequence of mixing of the precursor sources. By stabilizing clear precursor suspensions, discrete CHA nanoparticles were prepared, while the condensed aluminosilicate precursor suspensions resulted in the formation of agglomerated nanoparticles.

In situ PXRD study of the nanosized CHA zeolites synthesized by inorganic cations revealed the flexibility of the structure upon dehydration; the reversible structure upon cycled hydration/dehydration was observed.

In addition, nanosized RHO zeolite was prepared from a clear precursor suspension containing only inorganic cations (Cs^+, Na^+). Two different crystalline phases were refined upon dehydration of the nanosized RHO zeolite. These two structures showed different chemical composition and different Cs^+/Na^+ distributions over the RHO nanocrystals. The comparison of the two structures also shows the ability of the Cs^+ cation to be displaced in and out from the D8Rs. This movement determines the selective adsorption of the RHO zeolite towards CO_2 in the presence of CH_4. More work will be carried out in the future to understand clearly the cause of these cation displacements.

The important role of zeolite extra framework cations for gas adsorption applications was highlighted. This thesis reports on the selective sorption behaviour of as-prepared and the ion exchanged nanosized CHA type zeolites toward CO_2. Here, *in-situ* FTIR spectroscopy of CO_2 and CH_4 at room temperature was very helpful to see the interactions between the

gases and different zeolites with various cations. For example, the evidence for the high formation of carbonates in Cs-CHA could explain that the Cs-CHA adsorbed 2.3mmol/g (0 °C and 121kPa) while r2.5-CHA, K-CHA and Na-CHA adsorb 3.7, 3.7 and 4.1 mmol/g, respectively. The FTIR and the TG results demonstrated the high potential of CHA and RHO for CO_2/CH_4 separation.

The CO_2 adsorption mechanism in the CHA nanosized zeolite was further studied by *in situ* XRPD diffraction. We demonstrated that the atomic displacement parameters (ADPs) of the Cs atoms have a highly anisotropic aspect with an elongation in a direction perpendicular to the 8MR. This finding indicates that the cation is largely oscillating around its average position in the center of the 8MR of the CHA crystals. The mean atomic displacement parameter perpendicular to the 8MR door is about (perpendicular) $U_{\perp}$= 0.354 Å² while the (parallel) $U_{\parallel}$ is between 0.023 and 0.031 Å². The large oscillation of the door keeping cation around its average position in the centre of the 8MR was predicted before by not experimentally demonstrated.

In this work BPH type nanosized zeolite was also synthesized at room temperature. By modifying the preparation conditions, BPH crystals with various morphologies were synthesized, i.e., plate-like, spheroidal and nanosheets. The as-prepared BPH has shown a good CO_2 adsorption capacity, demonstrating the ability of the material for an application for the CO_2 capture and storage. However, this zeolite has 12MR channels giving the accessibility to different molecules (annex 2). Thus in comparison to the CHA and RHO nanosized zeolites, the BPH zeolite does not show any selectivity towards CO_2 and N_2.

Regardless to our research output, there are still fields within this work that demand further investigation. Additional experiments are required to obtain a clear understanding of the gas diffusion into the microporous materials: especially, a clear experimental evidence of the impact of the downsizing of crystals. Moreover, the selectivity was demonstrated but it hasn't been quantified for CO_2/CH_4 separation using breakthrough curves.

The selectivity for CO_2 is due to the adsorption on two different sites as described adequately by dual-site Langmuir (DSL) model. Quantification of adsorbed CH_4 in the zeolite could not be determined as for CO_2. The determination of the selectivity with isothermal analyzes or breakthrough curve will be carried out later, but today an approximate quantification is given for N_2 adsorption at 0 °C. Then, the materials could be shaped in pellets or membranes to be tested in real conditions.

The incorporation of metals of interest in the starting gel seems to have an impact on the final properties, especially Tungsten, Molybdenum and Vanadium oxides. These materials

were made with idea to limit the formation of defect[140], and potentially, prevent the interaction with H_2S[141] (molecule present in biogas).

There are still a lot of possibilities to optimize the CHA materials to find the most efficient one for particular gas adsorption. The further investigations have to be carried out to have a better understanding of the gas adsorption, especially the N_2 and CH_4. Another breakthrough in the field of zeolites consists to increase the Si/Al ratio of this type de CHA or RHO to 3. This improvement would allow using the CHA material as catalyst of SCR or MTO reaction[69]. Today, direct synthesis of nanosized CHA for SCR or MTO catalyst doesn't exist to my knowledge.[47]

Bibliography

1. Petersson, A. & Wellinger, A. Biogas upgrading technologies – developments and innovations. 20 (2009).
2. Faramawy, S., Zaki, T. & Sakr, A. A.-E. Natural gas origin, composition, and processing: A review. *Journal of Natural Gas Science and Engineering* **34**, 34–54 (2016).
3. Kermani, M. B. & Morshed, A. Carbon Dioxide Corrosion in Oil and Gas Production—A Compendium. *CORROSION* **59**, 659–683 (2003).
4. BP Statistical Review of World Energy 2016. 48
5. Aaron, D. & Tsouris, C. Separation of CO_2 from Flue Gas: A Review. *Separation Science and Technology* **40**, 321–348 (2005).
6. Patterson, T., Esteves, S., Dinsdale, R. & Guwy, A. An evaluation of the policy and techno-economic factors affecting the potential for biogas upgrading for transport fuel use in the UK. *Energy Policy* **39**, 1806–1816 (2011).
7. Ho, M. T., Allinson, G. W. & Wiley, D. E. Reducing the Cost of CO2 Capture from Flue Gases Using Pressure Swing Adsorption. *Ind. Eng. Chem. Res.* **47**, 4883–4890 (2008).
8. Sanz-Pérez, E. S., Murdock, C. R., Didas, S. A. & Jones, C. W. Direct Capture of CO_2 from Ambient Air. *Chemical Reviews* **116**, 11840–11876 (2016).
9. Yu, C.-H. A Review of CO2 Capture by Absorption and Adsorption. *Aerosol and Air Quality Research* (2012). doi:10.4209/aaqr.2012.05.0132
10. Krishna, R. & van Baten, J. M. A molecular dynamics investigation of the diffusion characteristics of cavity-type zeolites with 8-ring windows. *Microporous and Mesoporous Materials* **137**, 83–91 (2011).
11. Guisnet, M. & Pinard, L. Zéolithes - De la synthèse aux applications. 23 (2018).
12. Cejka, J. *Introduction to Zeolite science and practice, Volume 168, Third Edition (Studies in Surface Science and Catalysis)*. (Elsevier Science, 2007).
13. Vermeiren, W. & Gilson, J.-P. Impact of Zeolites on the Petroleum and Petrochemical Industry. *Top Catal* **52**, 1131–1161 (2009).
14. Perego, C. & Bosetti, A. Biomass to fuels: The role of zeolite and mesoporous materials. *Microporous and Mesoporous Materials* **144**, 28–39 (2011).
15. Thiele, E. W. Relation between Catalytic Activity and Size of Particle. *Ind. Eng. Chem.* **31**, 916–920 (1939).
16. Mintova, S., Gilson, J.-P. & Valtchev, V. Advances in nanosized zeolites. *Nanoscale* **5**, 6693 (2013).
17. Tosheva, L. & Valtchev, V. P. Nanozeolites: Synthesis, Crystallization Mechanism, and Applications. *Chemistry of Materials* **17**, 2494–2513 (2005).
18. Imai, H., Hayashida, N., Yokoi, T. & Tatsumi, T. Direct crystallization of CHA-type zeolite from amorphous aluminosilicate gel by seed-assisted method in the absence of organic-structure-directing agents. *Microporous and Mesoporous Materials* **196**, 341–348 (2014).
19. Majano, G., Darwiche, A., Mintova, S. & Valtchev, V. Seed-Induced Crystallization of Nanosized Na-ZSM-5 Crystals. *Ind. Eng. Chem. Res.* **48**, 7084–7091 (2009).
20. Honda, K., Yashiki, A., Sadakane, M. & Sano, T. Hydrothermal conversion of FAU and ∗BEA-type zeolites into MAZ-type zeolites in the presence of non-calcined seed crystals. *Microporous and Mesoporous Materials* **196**, 254–260 (2014).
21. Zhang, H. *et al.* Organic template-free synthesis of zeolite mordenite nanocrystals through exotic seed-assisted conversion. *RSC Advances* **6**, 47623–47631 (2016).
22. Itabashi, K., Kamimura, Y., Iyoki, K., Shimojima, A. & Okubo, T. A Working Hypothesis for Broadening Framework Types of Zeolites in Seed-Assisted Synthesis without Organic Structure-Directing Agent. *J. Am. Chem. Soc.* **134**, 11542–11549 (2012).

23. Wu, Z., Song, J., Ji, Y., Ren, L. & Xiao, F.-S. Organic Template-Free Synthesis of ZSM-34 Zeolite from an Assistance of Zeolite L Seeds Solution. *Chem. Mater.* **20**, 357–359 (2008).
24. Kamimura, Y., Chaikittisilp, W., Itabashi, K., Shimojima, A. & Okubo, T. Critical Factors in the Seed-Assisted Synthesis of Zeolite Beta and "Green Beta" from OSDA-Free Na+–Aluminosilicate Gels. *Chemistry – An Asian Journal* **5**, 2182–2191 (2010).
25. Xie, B. *et al.* Organotemplate-Free and Fast Route for Synthesizing Beta Zeolite. *Chem. Mater.* **20**, 4533–4535 (2008).
26. Ng, E.-P., Chateigner, D., Bein, T., Valtchev, V. & Mintova, S. Capturing Ultrasmall EMT Zeolite from Template-Free Systems. *Science* **335**, 70–73 (2012).
27. Ng, E.-P. *et al.* EMT-type zeolite nanocrystals synthesized from rice husk. *Microporous and Mesoporous Materials* **204**, 204–209 (2015).
28. Awala, H. *et al.* Template-free nanosized faujasite-type zeolites. *Nature Materials* **14**, 447–451 (2015).
29. Rajagopalan, K., Peters, A. W. & Edwards, G. C. Influence of zeolite particle size on selectivity during fluid catalytic cracking. *Applied Catalysis* **23**, 69–80 (1986).
30. Anfray, C., Dong, B., Komaty, S., Mintova, S. & Valable, S. Acute Toxicity of Silver Free and Encapsulated in Nanosized Zeolite for Eukaryotic Cells. *ACS Appl. Mater. Interfaces* **9**, 13849–13854 (2017).
31. Maldonado, M., Oleksiak, M. D., Chinta, S. & Rimer, J. D. Controlling Crystal Polymorphism in Organic-Free Synthesis of Na-Zeolites. *Journal of the American Chemical Society* **135**, 2641–2652 (2013).
32. Navrotsky, A., Trofymluk, O. & Levchenko, A. A. Thermochemistry of Microporous and Mesoporous Materials. *Chemical Reviews* **109**, 3885–3902 (2009).
33. Oleksiak, M. D. & Rimer, J. D. Synthesis of zeolites in the absence of organic structure-directing agents: factors governing crystal selection and polymorphism. *Reviews in Chemical Engineering* **30**, 1–49 (2014).
34. Sig Ko, Y. & Seung Ahn, W. Crystallization of zeolite L from Na2O–K2O–Al2O3–SiO2–H2O system. *Powder Technology* **145**, 10–19 (2004).
35. Rakoczy, R. A., Breuninger, M., Hunger, M., Traa, Y. & Weitkamp, J. Template-Free Synthesis of Zeolite Ferrierite and Characterization of its Acid Sites. *Chemical Engineering & Technology* **25**, 273–275 (2002).
36. Robson, H. E., Shoemaker, D. P., Ogilvie, R. A. & Manor, P. C. Synthesis and Crystal Structure of Zeolite Rho—A New Zeolite Related to Linde Type A. in *Molecular Sieves* (eds. Meier, W. M. & Uytterhoeven, J. B.) **121**, 106–115 (Journal of american chemical society, 1973).
37. E. Robson, H. ZEOLITE RHO. *United States Patent* **3,904,738**, 5 (1975).
38. Valtchev, V. P. & Bozhilov, K. N. Evidences for Zeolite Nucleation at the Solid−Liquid Interface of Gel Cavities. *Journal of the American Chemical Society* **127**, 16171–16177 (2005).
39. Valtchev, V. P., Tosheva, L. & Bozhilov, K. N. Synthesis of Zeolite Nanocrystals at Room Temperature. *Langmuir* **21**, 10724–10729 (2005).
40. Idris, A. *et al.* Fabrication zone of OSDA-free and seed-free mordenite crystals. *Powder Technology* **342**, 992–997 (2019).
41. Kharchenko, A., Lebedev, O. I., Zholobenko, V., de Waele, V. & Mintova, S. Formation of Copper Nanoparticles in LTL Nanosized Zeolite: Kinetics Study. *The Journal of Physical Chemistry C* **120**, 26300–26308 (2016).
42. Wong, S.-F. *et al.* K-F zeolite nanocrystals synthesized from organic-template-free precursor mixture. *Microporous and Mesoporous Materials* **249**, 105–110 (2017).
43. Ng, E.-P. *et al.* Synthesis of colloidal stable Linde Type J (LTJ) zeolite nanocrystals from rice husk silica and their catalytic performance in Knoevenagel reaction. *Materials Chemistry and Physics* **155**, 30–35 (2015).
44. Ali Ghrear, T. M. *et al.* Synthesis of Cs-ABW nanozeolite in organotemplate-free system. *Microporous and Mesoporous Materials* **277**, 78–83 (2019).

45. Ahmad, N. H., Goldyn, K., Mintova, S., Ling, T. C. & Ng, E.-P. Nanosized Cs-pollucite zeolite synthesized under mild condition and its catalytic behavior. *Materials Research Express* **6**, 025026 (2018).
46. Iwama, M. *et al.* Location of Alkali Ions and their Relevance to Crystallization of Low Silica X Zeolite. *Crystal Growth & Design* **10**, 3471–3479 (2010).
47. Dusselier, M. & Davis, M. E. Small-Pore Zeolites: Synthesis and Catalysis. *Chem. Rev.* **118**, 5265–5329 (2018).
48. Nearchou, A. & Sartbaeva, A. Influence of alkali metal cations on the formation of zeolites under hydrothermal conditions with no organic structure directing agents. *CrystEngComm* **17**, 2496–2503 (2015).
49. Chatelain, T. *et al.* Synthesis and characterization of high-silica zeolite RHO prepared in the presence of 18-crown-6 ether as organic template. *Microporous Materials* **4**, 231–238 (1995).
50. Palomino, M., Corma, A., Rey, F. & Valencia, S. New Insights on CO2−Methane Separation Using LTA Zeolites with Different Si/Al Ratios and a First Comparison with MOFs. *Langmuir* **26**, 1910–1917 (2010).
51. Guo, X., Corbin, D. R. & Navrotsky, A. Thermodynamics of H2O and CO2 Absorption and Guest-Induced Phase Transitions in Zeolite RHO. *J. Phys. Chem. C* **122**, 20366–20376 (2018).
52. Calligaris, M., Nardin, G. & Randaccio, L. Cation site location in hydrated chabazites. Crystal structure of potassium- and silver- exchanged chabazites. *Zeolites* **3**, 205–208 (1983).
53. Dent, L. S. & Smith, J. V. Crystal Structure of Chabazite, a Molecular Sieve. *Nature* **181**, 1794–1796 (1958).
54. Zones, S. I. & Zones, S. I. Zeolite SSZ-13 and its method of preparation. (1985).
55. Cao, G. *et al.* Synthesis of chabazite-containing molecular sieves and their use in the conversion of oxygenates to olefins. (2007).
56. Martín, N., Moliner, M. & Corma, A. High yield synthesis of high-silica chabazite by combining the role of zeolite precursors and tetraethylammonium: SCR of NOx. *Chem. Commun.* **51**, 9965–9968 (2015).
57. Ren, L. *et al.* Designed copper–amine complex as an efficient template for one-pot synthesis of Cu-SSZ-13 zeolite with excellent activity for selective catalytic reduction of NOx by NH3. *Chem. Commun.* **47**, 9789–9791 (2011).
58. Xie, L. *et al.* Excellent Performance of One-Pot Synthesized Cu-SSZ-13 Catalyst for the Selective Catalytic Reduction of NO_x with NH_3. *Environmental Science & Technology* **48**, 566–572 (2014).
59. Bourgogue, M. PROCESS FOR THE PREPARATION OF SYNTHETIC ZEOLITES, AND ZEOLITES OBTANED BY SAEED PROCESS. *US Patent 4,503,024* 10 (1985).
60. Davis, T. M. METHOD FOR PREPARING HIGH-SILICA LEV-TYPE ZEOLITES. 6 (2014).
61. Van Tendeloo, L., Gobechiya, E., Breynaert, E., Martens, J. A. & Kirschhock, C. E. A. Alkaline cations directing the transformation of FAU zeolites into five different framework types. *Chemical Communications* **49**, 11737 (2013).
62. Anand, C. *et al.* Downsizing the K-CHA zeolite by a postmilling-recrystallization method for enhanced base-catalytic performance. *New Journal of Chemistry* **40**, 492–496 (2016).
63. Li, Z., Navarro, M. T., Martínez-Triguero, J., Yu, J. & Corma, A. Synthesis of nano-SSZ-13 and its application in the reaction of methanol to olefins. *Catalysis Science & Technology* **6**, 5856–5863 (2016).
64. Wakihara, T. *et al.* Fabrication of Fine Zeolite with Improved Catalytic Properties by Bead Milling and Alkali Treatment. *ACS Appl. Mater. Interfaces* **2**, 2715–2718 (2010).
65. Wakihara, T. *et al.* Bead-Milling and Postmilling Recrystallization: An Organic Template-free Methodology for the Production of Nano-zeolites. *Crystal Growth & Design* **11**, 955–958 (2011).
66. Zhou, M. & Hedlund, J. Facile Preparation of Hydrophobic Colloidal MFI and CHA Crystals and Oriented Ultrathin Films. *Angewandte Chemie International Edition* **57**, 10966–10970 (2018).
67. Takata, T., Tsunoji, N., Takamitsu, Y., Sadakane, M. & Sano, T. Nanosized CHA zeolites with high thermal and hydrothermal stability derived from the hydrothermal conversion of FAU zeolite. *Microporous and Mesoporous Materials* **225**, 524–533 (2016).

68. Liu, B. *et al.* Synthesis of low-silica CHA zeolite chabazite in fluoride media without organic structural directing agents and zeolites. *Microporous and Mesoporous Materials* **196**, 270–276 (2014).
69. Ji, Y., Deimund, M. A., Bhawe, Y. & Davis, M. E. Organic-Free Synthesis of CHA-Type Zeolite Catalysts for the Methanol-to-Olefins Reaction. *ACS Catalysis* **5**, 4456–4465 (2015).
70. Zones, S. I. & Van Nordstrand, R. A. Novel zeolite transformations: The template-mediated conversion of Cubic P zeolite to SSZ-13. *Zeolites* **8**, 166–174 (1988).
71. Goto, I. *et al.* Transformation of LEV-type zeolite into less dense CHA-type zeolite. *Microporous and Mesoporous Materials* **158**, 117–122 (2012).
72. Du, T. *et al.* Synthesis of Nanocontainer Chabazites from Fly Ash with a Template- and Fluoride-Free Process for Cesium Ion Adsorption. *Energy Fuels* **31**, 4301–4307 (2017).
73. Poling, B. E., Prausnitz, J. M. & O'Connell, J. P. *The properties of gases and liquids*. (2001).
74. Rzepka, P. *et al.* CO_2 -Induced Displacement of Na^+ and K^+ in Zeolite |NaK|-A. *The Journal of Physical Chemistry C* **122**, 17211–17220 (2018).
75. Liu, Q. *et al.* NaKA sorbents with high CO2-over-N2 selectivity and high capacity to adsorb CO2. *Chem. Commun.* **46**, 4502–4504 (2010).
76. Shang, J. *et al.* Discriminative Separation of Gases by a "Molecular Trapdoor" Mechanism in Chabazite Zeolites. *Journal of the American Chemical Society* **134**, 19246–19253 (2012).
77. Shang, J. *et al.* Determination of Composition Range for "Molecular Trapdoor" Effect in Chabazite Zeolite. *The Journal of Physical Chemistry C* **117**, 12841–12847 (2013).
78. Du, T. *et al.* An optimal trapdoor zeolite for exclusive admission of CO2 at industrial carbon capture operating temperatures. *Chem. Commun.* **54**, 3134–3137 (2018).
79. De Baerdemaeker, T. & De Vos, D. Trapdoors in zeolites: Gas separation. *Nature Chemistry* **5**, 89–90 (2013).
80. Shang, J. *et al.* Determination of Composition Range for "Molecular Trapdoor" Effect in Chabazite Zeolite. (2013). Available at: http://pubs.acs.org/doi/suppl/10.1021/jp4015146. (Accessed: 25th January 2017)
81. Lozinska, M. M. *et al.* Cation Gating and Relocation during the Highly Selective "Trapdoor" Adsorption of CO2 on Univalent Cation Forms of Zeolite Rho. *Chem. Mater.* **26**, 2052–2061 (2014).
82. Kong, M., Liu, Z., Vogt, T. & Lee, Y. Chabazite structures with Li+, Na+, Ag+, K+, NH4+, Rb+ and Cs+ as extra-framework cations. *Microporous and Mesoporous Materials* **221**, 253–263 (2016).
83. Pham, T. D., Hudson, M. R., Brown, C. M. & Lobo, R. F. Molecular Basis for the High CO_2 Adsorption Capacity of Chabazite Zeolites. *ChemSusChem* **7**, 3031–3038 (2014).
84. Hong, S.-H., Jang, M.-S., Cho, S. J. & Ahn, W.-S. Chabazite and zeolite 13X for CO2 capture under high pressure moderate temperature conditions. 55
85. Prodinger, S. *et al.* Impact of chabazite SSZ-13 textural properties and chemical composition on CO2 adsorption applications. *New J. Chem.* **40**, 4375–4385 (2016).
86. Hudson, M. R. *et al.* Unconventional, Highly Selective CO_2 Adsorption in Zeolite SSZ-13. *Journal of the American Chemical Society* **134**, 1970–1973 (2012).
87. Alberti, A., Galli, E., Vezzalini, G., Passaglia, E. & Zanazzi, P. F. Position of cations and water molecules in hydrated chabazite. Natural and Na-, Ca-, Sr- and K-exchanged chabazites. *Zeolites* **2**, 303–309 (1982).
88. Li, G. *et al.* Temperature-regulated guest admission and release in microporous materials. *Nature Communications* **8**, (2017).
89. Palomino, M., Corma, A., Jordá, J. L., Rey, F. & Valencia, S. Zeolite Rho: a highly selective adsorbent for CO_2 /CH_4 separation induced by a structural phase modification. *Chem. Commun.* **48**, 215–217 (2012).
90. Coudert, F.-X. & Kohen, D. Molecular Insight into CO2 "Trapdoor" Adsorption in Zeolite Na-RHO. *Chemistry of Materials* **29**, 2724–2730 (2017).
91. Lozinska, M. M. *et al.* Cation Control of Molecular Sieving by Flexible Li-Containing Zeolite Rho. *J. Phys. Chem. C* **120**, 19652–19662 (2016).

92. Bail, A. L. Whole powder pattern decomposition methods and applications: A retrospection. *Powder Diffraction* **20**, 316–326 (2005).
93. Paufler, P. R. A. Young (ed.). The Rietveld Method. International Union of Crystallography. Oxford University Press 1993. 298 p. Price £ 45.00. ISBN 0–19–855577–6. *Crystal Research and Technology* **30**, 494–494 (1995).
94. Thommes, M. *et al.* Physisorption of gases, with special reference to the evaluation of surface area and pore size distribution (IUPAC Technical Report). *Pure and Applied Chemistry* **87**, 1051–1069 (2015).
95. Mason, J. A., Sumida, K., Herm, Z. R., Krishna, R. & Long, J. R. Evaluating metal–organic frameworks for post-combustion carbon dioxide capture via temperature swing adsorption. *Energy Environ. Sci.* **4**, 3030–3040 (2011).
96. Nguyen, C. & Do, D. D. Dual Langmuir Kinetic Model for Adsorption in Carbon Molecular Sieve Materials. *Langmuir* **16**, 1868–1873 (2000).
97. Gemmi, M. *et al.* 3D Electron Diffraction: The Nanocrystallography Revolution. *ACS Cent. Sci.* **5**, 1315–1329 (2019).
98. Palatinus, L. *et al.* Structure refinement using precession electron diffraction tomography and dynamical diffraction: tests on experimental data. *Acta Cryst B* **71**, 740–751 (2015).
99. Palatinus, L., Petříček, V. & Corrêa, C. A. Structure refinement using precession electron diffraction tomography and dynamical diffraction: theory and implementation. *Acta Cryst A* **71**, 235–244 (2015).
100. Hydrogen positions in single nanocrystals revealed by electron diffraction | Science. Available at: https://science.sciencemag.org/content/355/6321/166/tab-figures-data. (Accessed: 13th June 2019)
101. Vincent, R. & Midgley, P. A. Double conical beam-rocking system for measurement of integrated electron diffraction intensities. *Ultramicroscopy* **53**, 271–282 (1994).
102. Mugnaioli, E., Gorelik, T. & Kolb, U. “Ab initio” structure solution from electron diffraction data obtained by a combination of automated diffraction tomography and precession technique. *Ultramicroscopy* **109**, 758–765 (2009).
103. Boullay, P., Palatinus, L. & Barrier, N. Precession Electron Diffraction Tomography for Solving Complex Modulated Structures: the Case of $Bi_5Nb_3O_{15}$. *Inorganic Chemistry* **52**, 6127–6135 (2013).
104. (IUCr) Specifics of the data processing of precession electron diffraction tomography data and their implementation in the program PETS2.0. Available at: https://onlinelibrary.wiley.com/iucr/doi/10.1107/S2052520619007534. (Accessed: 6th September 2019)
105. Palatinus, L. & Chapuis, G. SUPERFLIP – a computer program for the solution of crystal structures by charge flipping in arbitrary dimensions. *J Appl Cryst* **40**, 786–790 (2007).
106. Petříček, V., Dušek, M. & Plášil, J. Crystallographic computing system Jana2006: solution and refinement of twinned structures. *Zeitschrift für Kristallographie - Crystalline Materials* **231**, (2016).
107. McCusker, L. B. & Baerlocher, C. Using electron microscopy to complement X-ray powder diffraction data to solve complex crystal structures. *Chem. Commun.* 1439–1451 (2009). doi:10.1039/B821716E
108. In Situ Fourier Transform Infrared (FTIR) Investigation of CO2 Adsorption onto Zeolite Materials. *ResearchGate* Available at: https://www.researchgate.net/publication/231273555_In_Situ_Fourier_Transform_Infrared_FTIR_Investigation_of_CO2_Adsorption_onto_Zeolite_Materials. (Accessed: 30th May 2017)
109. Mintova, S., Gilson, J.-P. & Valtchev, V. Advances in nanosized zeolites. *Nanoscale* **5**, 6693 (2013).
110. Mintova, S., Grand, J. & Valtchev, V. Nanosized zeolites: Quo Vadis? *Comptes Rendus Chimie* **19**, 183–191 (2016).

111. Kunitake, Y. *et al.* Synthesis of titanated chabazite with enhanced thermal stability by hydrothermal conversion of titanated faujasite. *Microporous and Mesoporous Materials* **215**, 58–66 (2015).
112. Conato, M. T., Oleksiak, M. D., McGrail, B. P., Motkuri, R. K. & Rimer, J. D. Framework stabilization of Si-rich LTA zeolite prepared in organic-free media. *Chem. Commun.* **51**, 269–272 (2014).
113. Taguchi, G., Chowdhury, S. & Yuin, W. Taguchi's Quality Engineering Handbook. in (2005).
114. Borel, M. *et al.* SDA-Free Hydrothermal Synthesis of High-Silica Ultra-nanosized Zeolite Y. *Crystal Growth & Design* **17**, 1173–1179 (2017).
115. Shang, J. *et al.* Discriminative Separation of Gases by a "Molecular Trapdoor" Mechanism in Chabazite Zeolites. (2012). Available at: http://pubs.acs.org/doi/suppl/10.1021/ja309274y. (Accessed: 25th January 2017)
116. Shang, J. *et al.* Potassium Chabazite: A Potential Nanocontainer for Gas Encapsulation. *The Journal of Physical Chemistry C* **114**, 22025–22031 (2010).
117. Zones, S. I. Conversion of faujasites to high-silica chabazite SSZ-13 in the presence of N,N,N-trimethyl-1-adamantammonium iodide. *J. Chem. Soc., Faraday Trans.* **87**, 3709–3716 (1991).
118. Peng, C. *et al.* Preparation of nanosized SSZ-13 zeolite with enhanced hydrothermal stability by a two-stage synthetic method. *Microporous and Mesoporous Materials* **255**, 192–199 (2018).
119. Georgieva, V. M. *et al.* Triggered Gate Opening and Breathing Effects during Selective CO_2 Adsorption by Merlinoite Zeolite. *Journal of the American Chemical Society* **141**, 12744–12759 (2019).
120. Bacsik, Z., Cheung, O., Vasiliev, P. & Hedin, N. Selective separation of CO 2 and CH 4 for biogas upgrading on zeolite NaKA and SAPO-56. *Applied Energy* **162**, 613–621 (2016).
121. Remy, T. *et al.* Biogas upgrading through kinetic separation of carbon dioxide and methane over Rb- and Cs-ZK-5 zeolites. *RSC Adv.* **4**, 62511–62524 (2014).
122. Polisi, M. *et al.* CO_2 Adsorption/Desorption in FAU Zeolite Nanocrystals: In Situ Synchrotron X-ray Powder Diffraction and in Situ Fourier Transform Infrared Spectroscopic Study. *The Journal of Physical Chemistry C* **123**, 2361–2369 (2019).
123. Bae, T.-H. *et al.* Evaluation of cation-exchanged zeolite adsorbents for post-combustion carbon dioxide capture. *Energy Environ. Sci.* **6**, 128–138 (2013).
124. Cheung, O., Bacsik, Z., Liu, Q., Mace, A. & Hedin, N. Adsorption kinetics for CO2 on highly selective zeolites NaKA and nano-NaKA. *Applied Energy* **112**, 1326–1336 (2013).
125. Lee, L.-K. & Ruthven, D. M. Analysis of thermal effects in adsorption rate measurements. *Journal of the Chemical Society, Faraday Transactions 1: Physical Chemistry in Condensed Phases* **75**, 2406 (1979).
126. Atlas zeolites.
127. Smith, J. V., Rinaldi, F. & Glasser, L. S. D. Crystal structures with a chabazite framework. II. Hydrated Ca-chabazite at room temperature. *Acta Cryst* **16**, 45–53 (1963).
128. Yakubovich, O. V., Massa, W., Gavrilenko, P. G. & Pekov, I. V. Crystal structure of chabazite K. *Crystallogr. Rep.* **50**, 544–553 (2005).
129. Shang, J., Li, G., Webley, P. A. & Liu, J. Z. A density functional theory study for the adsorption of various gases on a caesium-exchanged trapdoor chabazite. *Computational Materials Science* **122**, 307–313 (2016).
130. Ke, Q. *et al.* Targeted Synthesis of Ultrastable High-Silica RHO Zeolite Through Alkali Metal-Crown Ether Interaction. *Chem Asian J* **12**, 1043–1047 (2017).
131. Ji, Y., Birmingham, J., Deimund, M. A., Brand, S. K. & Davis, M. E. Steam-dealuminated, OSDA-free RHO and KFI-type zeolites as catalysts for the methanol-to-olefins reaction. *Microporous and Mesoporous Materials* **232**, 126–137 (2016).
132. Lozinska, M. M. *et al.* Understanding Carbon Dioxide Adsorption on Univalent Cation Forms of the Flexible Zeolite Rho at Conditions Relevant to Carbon Capture from Flue Gases. *J. Am. Chem. Soc.* **134**, 17628–17642 (2012).
133. Balestra, S. R. G. *et al.* Understanding Nanopore Window Distortions in the Reversible Molecular Valve Zeolite RHO. *Chem. Mater.* **27**, 5657–5667 (2015).

134. Pera-Titus, M., Palomino, M., Valencia, S. & Rey, F. Thermodynamic analysis of framework deformation in Na,Cs-RHO zeolite upon CO2 adsorption. *Phys. Chem. Chem. Phys.* **16**, 24391–24400 (2014).
135. Corbin, D. R. *et al.* Flexibility of the zeolite RHO framework: in situ x-ray and neutron powder structural characterization of divalent cation-exchanged zeolite RHO. *J. Am. Chem. Soc.* **112**, 4821–4830 (1990).
136. Parise, J. B. & Prince, E. The structure of cesium-exchanged zeolite-RhO at 293K and 493K determined from high resolution neutron powder data. *Materials Research Bulletin* **18**, 841–852 (1983).
137. Neutron powder diffraction study of a Na,Cs-Rho zeolite. *Zeitschrift für Kristallographie* **187**, 253–266 (2010).
138. Lee, Y. *et al.* Phase Transition of Zeolite RHO at High-Pressure. *J. Am. Chem. Soc.* **123**, 8418–8419 (2001).
139. Ohlin, L., Bazin, P., Thibault-Starzyk, F., Hedlund, J. & Grahn, M. Adsorption of CO_2, CH_4, and H_2O in Zeolite ZSM-5 Studied Using In Situ ATR-FTIR Spectroscopy. *The Journal of Physical Chemistry C* **117**, 16972–16982 (2013).
140. Grand, J. *et al.* One-pot synthesis of silanol-free nanosized MFI zeolite. *Nature Materials* **16**, 1010–1015 (2017).
141. Ozekmekci, M., Salkic, G. & Fellah, M. F. Use of zeolites for the removal of H2S: A mini-review. *Fuel Processing Technology* **139**, 49–60 (2015).

ANNEXE 1

Synthesis of BPH-type nanosized zeolite at room temperature

Generally, the zeolite synthesis is performed at elevated temperatures. LTA zeolite was obtained after 30 days at room temperature in high alkaline media. Valtchev and co-workers[1] proposed the synthesis of LTA and SOD zeolites at room temperature after 4 and 3 days in oil bath respectively.

The BPH type zeolite has intersected 12MR (1D) and 8MR (2D) (Figure S1). The BPH is more well-known in the form of Beryllophosphate-H. This structure has been discovered in 1988 and it can be identified as zeolite Q (zeolite with Si/Al=1.1), UZM-4 (low Si/Al around 2.5), STA-5, PST-12 or ZnAPO- 59[2].

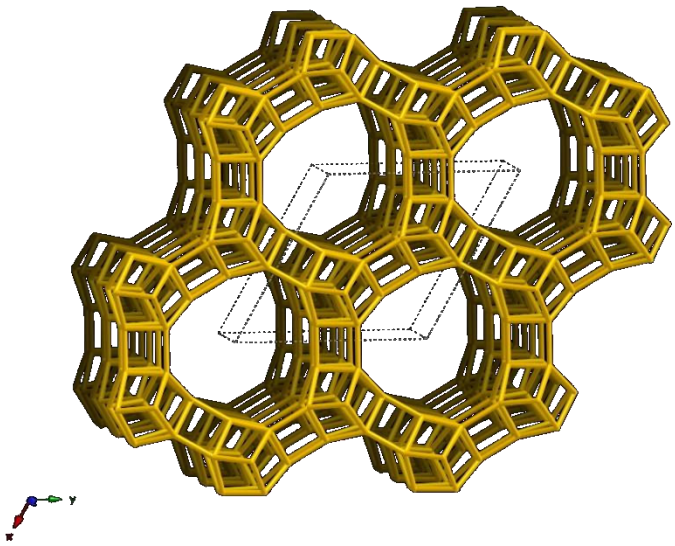

Figure S1: Framework structure of BPH along the [001] direction.

UOP has developed the charge density mismatch (CDM) approach to prepare zeolites as commercially method. One of the zeolite prepared with this method is the UZM-4 (BPH), using a choline−Li−Sr templated precursor mixture. Park and co-workers reported on the use of bi-templates TMACl-TEAOH for the synthesis of low silica BPH structure (UZM-4).[2] The synthesis was carried out at 120 °C for 6 days. While the seed approach allowed

[1] Valtchev, V. P.; Tosheva, L.; Bozhilov, K. N. Langmuir 2005, 21, 10724.
[2] Robert W. Broach, Nanette Greenlay, Paulina Jakubczak, Lisa M. Knight, Gregory J. Lewis Microporous and Mesoporous Materials 189 (2014) 49–63

increasing the Si/Al ratio to 8; the previous methods resulted into crystals with not higher Si/Al than 2.5[3].

To my knowledge, no synthesis of nanosized BPH zeolite has been proposed without organic template and especially at low temperature synthesis providing nanosized crystallites. The synthesis conditions used for preparation of aluminosilicate BPH are summarized in Table S1.

Table S1: Starting material and hydrothermal conditions for synthesis of aluminosilicate BPH zeolite. (The OSDA are written in red).

Name	Chemical compositions	Hydrothermal conditions	Crystal shape	Crystal Dimension	Si/Al (ICP)
PST-12[4]	1.0TEA_2O 5.3TMACl 0.7Li_2O 1.3Sr_2O 9.9H_2O	160°C – 21d	Flakes	150 nm	2.5
UZM-4[5]	0.1TEA_2O 3.3TMA 6.1Li 10.0Al 18.0Si 56O	125 °C – 72h	-	-	1.8
UZM-4[3]	4.0Ch 0.25LiCl 0.25NaCl 0.5Al_2O_3 5.0SiO_2 150H_2O	120 °C – 6d	-	-	3.0
Linde Q[6]	SiO_2 $3Al_2O_3$ 15K_2O 980H_20	60 °C– 2 months	-	-	1.1
UZM-4[2]	2TEA_2O 2.5SiO_2 0.5Al_2O_3 TMACl 0.5LiCl 100H_2O	120 °C –24 h	Flakes	100 nm	-
	2.5SiO_2 0.25Al_2O_3 2.5TMA_2O 0.5LiCl 150H_2O + seeds (5w%)	120 °C – 24 h	Flakes	500 nm	8.0

In chapter 3, the synthesis of BPH was presented. The BPH was synthesised by mixing the starting gel for 12 days (BPH(25), run 10) and with hydrothermal treatment 90 °C for 8 h (BPH(90), run 18). The LeBail refinement obtained for sample BPH(90) is shown in Figure S2. The samples have a good crystallinity with a broadening of the peak revelling nanosized samples with high anisotropy. The crystallites size calculated from the LeBail fitting using the Scherrer equation was between 70-80 nm in the (1 0 0) plan and 9-18 nm in the (0 0 1) plan.

[3] T. Moteki, T. Okubo, Chem. Mater. 2013, 25, 2603.
[4] Min Bum Park, Sang Hyun Ahn, Nak Ho Ahn and Suk Bong Hong ; Chem. Commun., 2015, 51, 3671
[5] C. S. Blackwell, R. W. Broach, M. G. Gatter, J. S. Holmgren, D.-Y. Jan, G. J. Lewis, B. J. Mezza, T. M. Mezza, M. A. Miller, J. G. Moscoso, R. L. Patton, L. M. Rohde, M. W. Schoonover, W. Sinkler, B. A. Wilson and S. T. Wilson, Angew. Chem., Int. Ed., 2003, 42, 1737.
[6] K.J. Andries, H.J. Bosmans and PJ. Grobet ; ZEOLITES, 1991, Vol 11, February 125

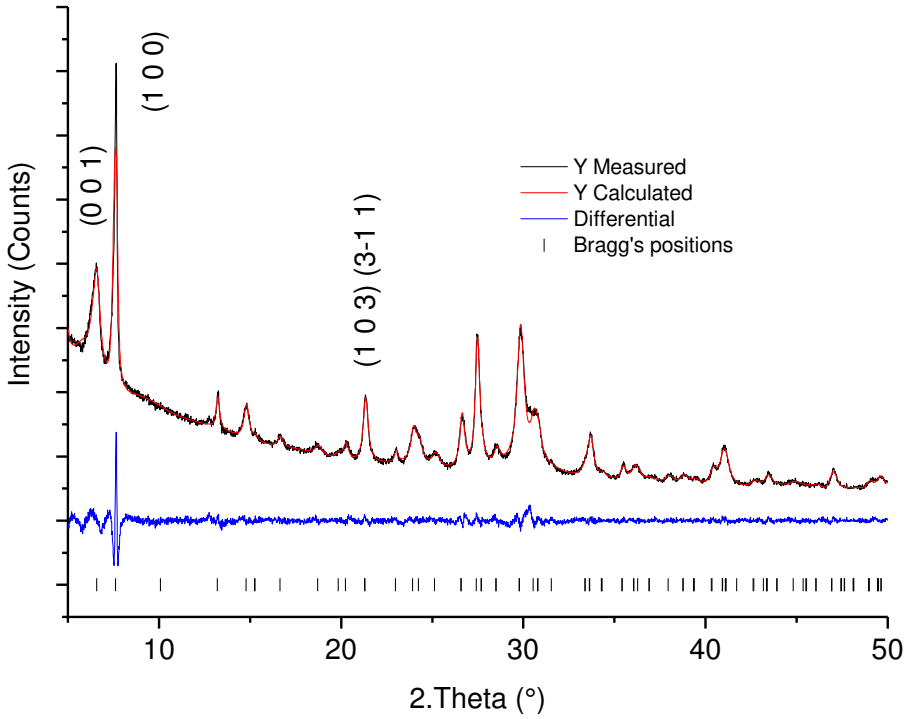

Figure S2 : LeBail refinement of BPH-90.

Le Bail refinement was carried out on samples BPH(25) and BPH(90) (Figure S2). The crystal structure of hydrated BPH (25) described with a hexagonal unit cell (*a* = b = 13.392(2) Å and c = 13.403(2) Å; GOF = 1.18 Rp = 3.24 wRp = 4.23) and space group P-62m. Similarly, hydrated BPH (90) described with a hexagonal unit cell (*a* = b = 13.3722(9) Å and c = 13.540(3) Å GOF = 1.96 Rp = 2.77 wRp = 3.97).

Table S1 : Chemical composition of BPH samples determinated by ICP analysis.

Run	Chemical composition	Si/Al (w/w)
BPH(25)	$(Cs_{4.1}\ K_{3.5}\ Na_{7.0})\ Si_{21.4}\ Al_{14.6}\ O_{72}$	1.52
BPH (90)	$(Cs_{4.7}\ K_{3.1}\ Na_{7.4})\ Si_{20.8}\ Al_{15.2}\ O_{72}$	1.42

The hydrothermal treatment has an effect on the Si/Al ratio of the final product (Table S1). The effect of the treatment seems to decrease the Si/Al but it can be attributed to small amount of amorphous silica visible on the PXRD pattern.

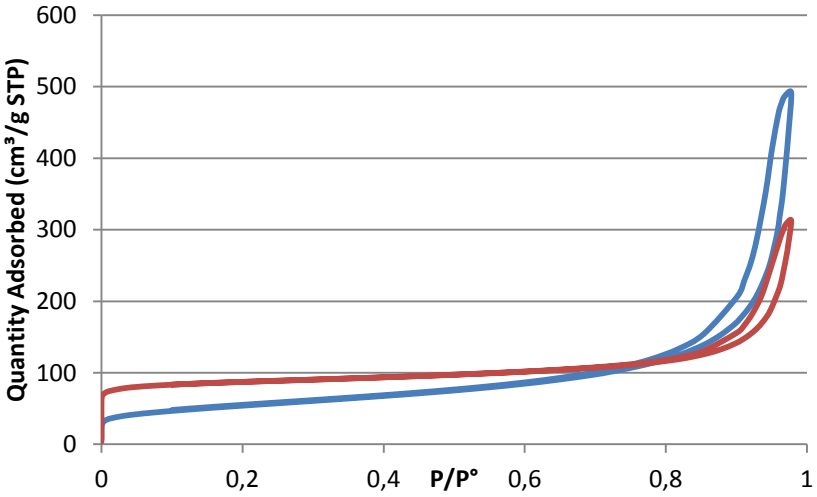

Figure S3 : Nitrogen adsorption isotherm at -196 °C of samples BPH(25) in blue and BPH(90) in red.

Table S2 : Specific surface area, BET surface area, pore volume of BPH zeolite samples.

Run	$S_{microporous}$ (t-plot)	S_{BET}	Pore vol. (t-plot)	Pore vol. (Dubinin-Astakhov)
BPH(25)	30 m^2/g	188 m^2/g	0.014 cm^3/g	0.100 cm^3/g
BPH(90)	199 m^2/g	275 m^2/g	0.102 cm^3/g	0.159 cm^3/g

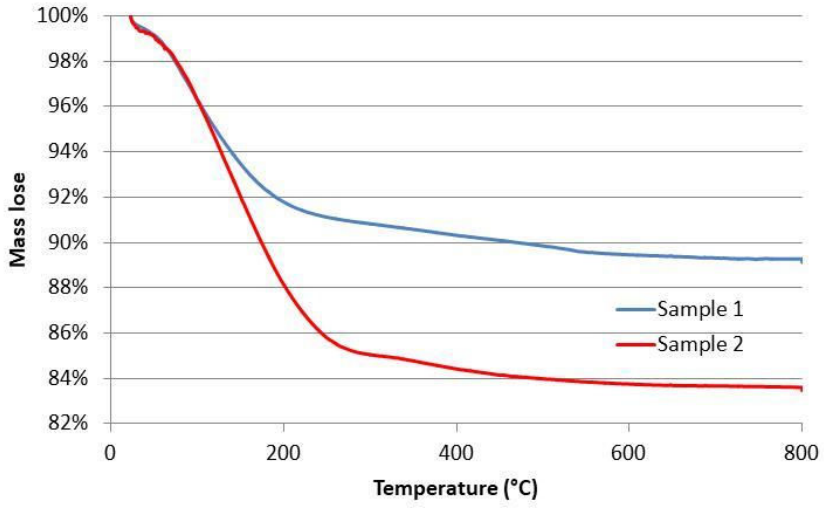

Figure S4: TG curves of samples 1 BPH(25) and sample 2 BPH(90)

The micropores volume of the zeolite BPH was evaluated by nitrogen adsorption (Figure S3). A substantial increase of the microporosity was observed for the sample obtained under hydrothermal treatment. The hysteresis at high partial pressure highlights the nanosized dimension of the zeolite crystals and the high external surface area. The thermogravimetric curves for both samples are presented in Figure S4. The BPH(90) seems to be stable until 350°C when the BPH(25) sample has a lower thermal stability. This observation explains

why the BPH(25) sample has a lower N_2 adsorption capacity at low partial pressure (Figure S3).

TEM images reveal that the primary crystallites have nanoflakes morphology typical of zeolite BPH (Figure S5). While the crystals synthesized without hydrothermal treatment were smaller than 150nm. The BPH crystals obtained under hydrothermal treatment appear as nano-sheets. Two different orientation of the crystals were identified: The orientation A corresponds to the flakes observed from the top, and the orientation B corresponds to the flakes observed from the side. The thickness of the particle is smaller than 10nm. No amorphous particles have been observed. Further analysis has to be performed to identify the orientation of the 12 MR channels in the BPH nanocrystals. At first sight, the 12MR channels should be oriented in the largest direction of the crystallites.

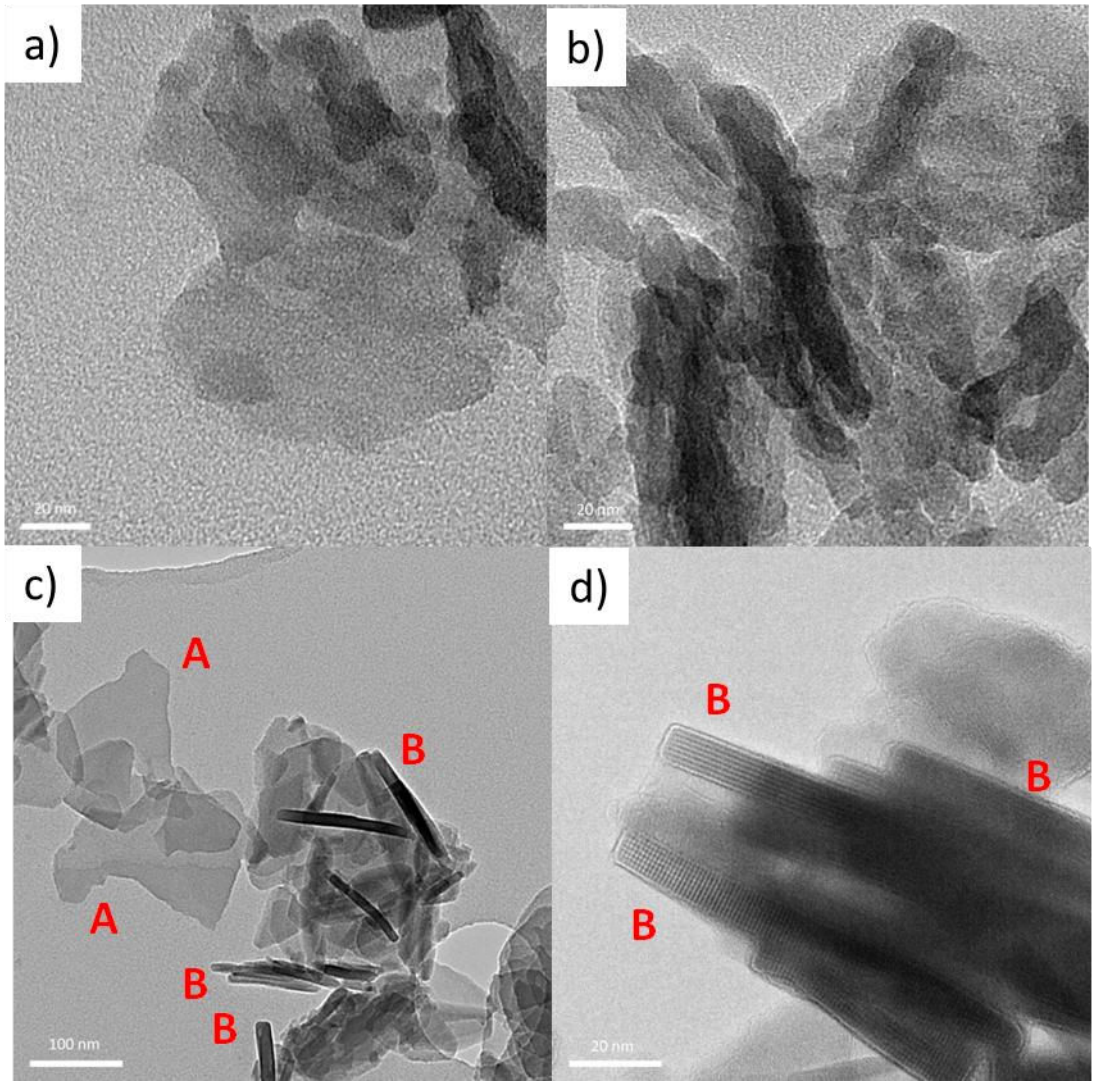

Figure S4: TEM images of as-synthesised (a and b) BPH(25) and (c and d) BPH(90) crystals. The sign A corresponds to top view and the sign B correspond side view.

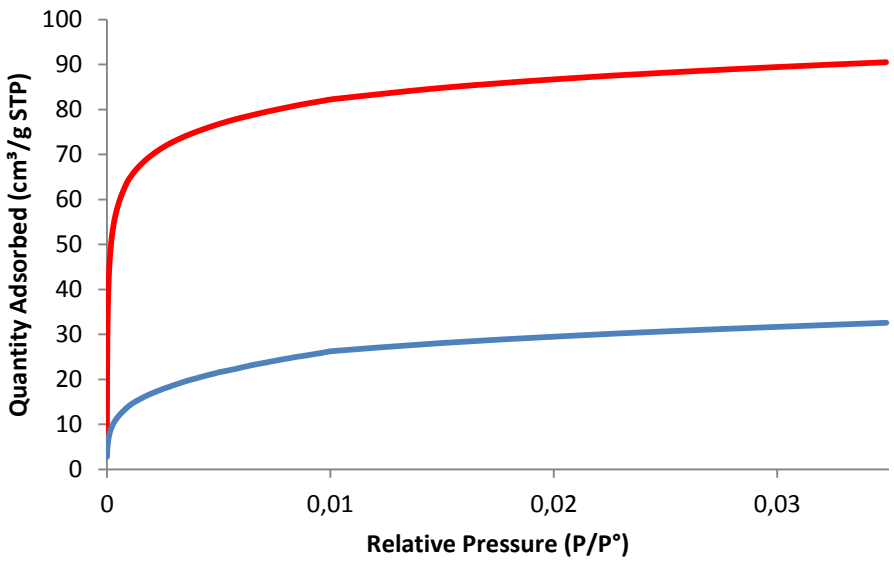

Figure S5: CO_2 adsorption isotherm recorded at 0 °C of samples BPH(25) in blue and BPH(90) in red.

In Figure S5, the CO_2 adsorption isotherms show a high CO_2 adsorption capacity at low pressure comparable to the best CHA sample synthesised in this work. The adsorption of CO_2 is almost complete at 10% of P_{atm}. The fitting of the dual site Langmuir model shows the adsorption of CO_2 by 2 different sites (physorption and chemisorption), as expected considering the low Si/Al ratio of the structure. The BPH(25) sample shows a lower adsorption capacity. This can be explained by the lower crystallinity of the material.

It is important to notice that the crystallinity of the BPH(90) sample after CO_2 adsorption experiment is fully preserved.

In conclusion, zeolite BPH can be synthesized without an organic template at room temperature. The high CO_2 adsorption capacity of the BPH nanosized zeolite has been shown; an application for CO_2 capture and storage will be considered in the future. This material is not appropriate for gas separation (CO_2/N_2 or CO_2/CH_4 for example).

ANNEX 2

Table S1: Screening of cations composition and stirring time of the precursor mixtures toward obtaining of dispersed CHA nanocrystals

Entry	Cations composition			Stirring	Results		
	Na_2O	K_2O	Cs_2O	Stirring time (days)	Phase	Si/Al (ICP) (w/w)	Particle size (nm)
1''	9	0.85	0.40	7	RHO/CHA	-	-
2''	**9.5**	**0.85**	**0.40**	7	**CHA**	**2.1**	**170**
3''	11	0.85	0.40	7	EDI	1.4	< 100
4''	9.5	0.75	0.40	7	RHO/CHA	-	-
5''	9.5	1.0	0.40	7	EDI	1.4	< 100
6''	9.5	0.85	0.30	7	RHO/CHA	-	-
7''	9.5	0.85	0.60	7	ANA	2.0	200
8''	9.5	0.85	0.40	1	CHA	2.0	>1000
9''	9.5	0.85	0.40	4	CHA	2.0	900

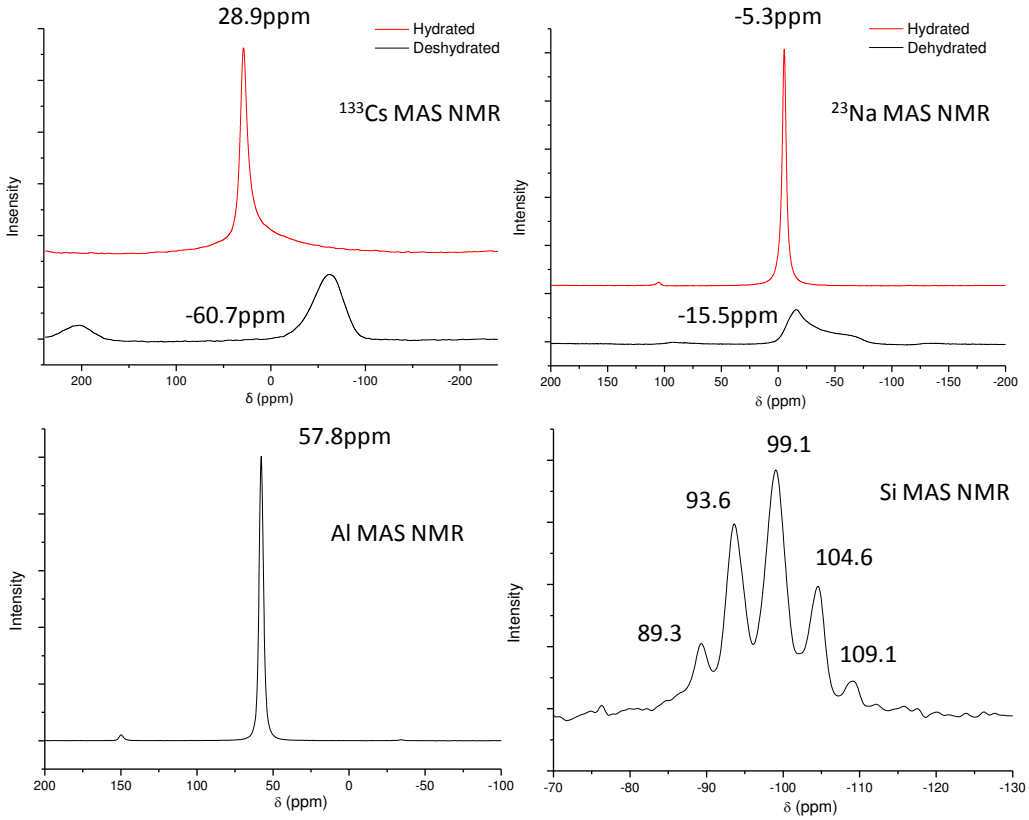

Figure S1: ^{133}Cs NMR, ^{23}Na NMR, ^{27}Al NMR and ^{29}Si NMR spectra of nanosized CHA zeolite (sample r2.0-CHA).

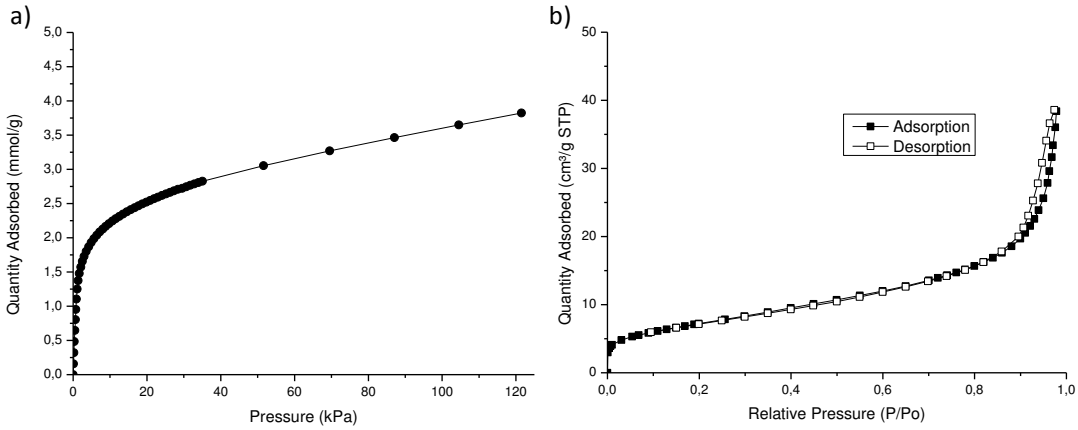

Figure S2: (a) Carbon dioxide sorption isotherm at 0 °C and (b) Nitrogen sorption isotherm at 77 K of nanosized CHA zeolite (sample r2.0-CHA).

a)

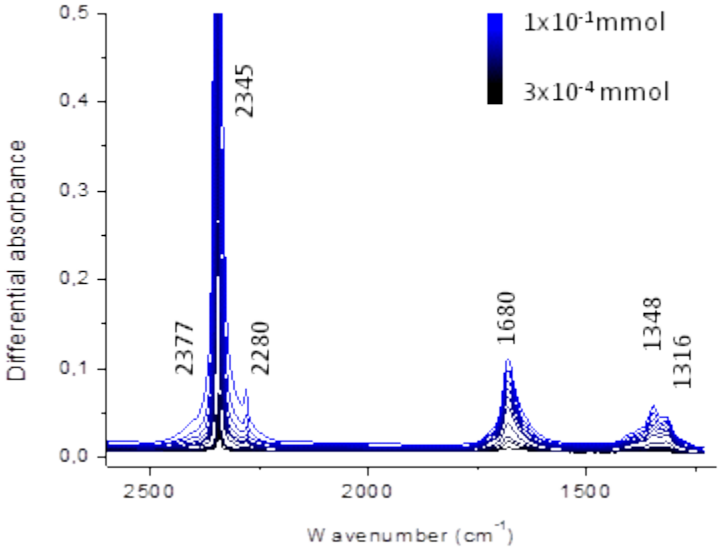

b)

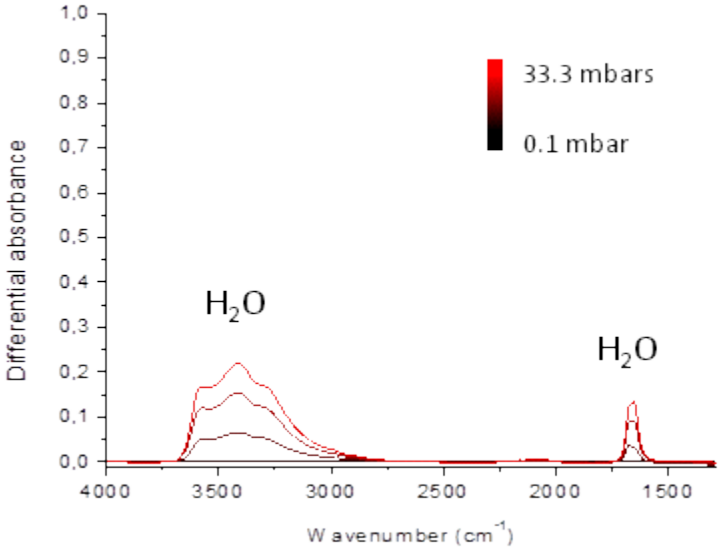

Figure S3: FTIR spectra recorded from nanosized CHA zeolite (sample r2.0-CHA) under delivery of small dose of (a) CO_2: $3x10^{-4}$ mmol to $1x10^{-1}$ mmol (black to blue) and (B) CH_4 at partial pressure of 0.1-20-28-33mbars (black to red) at room temperature.

ABSTRACT

Mots-clés: Chabazite, CO_2 adsorption, CO_2 In-situ PXRD, PEDT, Nanozéolithes, Chimie verte.

L'objectif de ce travail consiste à préparer des zéolithes à petits micropores en utilisant une voie de synthèse « verte ». Pour cela, il a été choisi de synthétiser directement des nanocristaux de zéolithe CHA et RHO sans agent organique structurant, avec un rapport Si/Al le plus adéquat pour la séparation du CO_2 du CH_4. La réduction de la taille des cristaux leur confère une meilleure stabilité et augmente la surface d'échange entre le matériau et les gaz. La première partie concerne l'élaboration d'une nouvelle voie de synthèse. Des nanocristaux compris entre 30 et 200 nm avec un rapport Si/Al variant de 1,4 à 2,6 ont été obtenus. Dans la seconde partie, l'analyse cristallographique des zéolithes RHO et CHA sous les formes hydratées et déshydratées est présentée. Des méthodes d'analyses utilisant la diffraction par précession des électrons en mode tomographie (PEDT) et *in-situ* DRX sur poudre ont été utilisées pour caractériser les zéolithes CHA et RHO après l'adsorption du CO_2. Les nanozéolithes de CHA et RHO ont ensuite démontrées leur efficacité pour l'adsorption sélective de CO_2 du CH_4.

Keywords: Chabazite, CO_2 adsorption, CO_2 In-situ PXRD, PEDT, Nanozeolites, OSDA-free.

The goal of this work is to prepare template-free small pore nanosized zeolites. The direct synthesis of nanosized CHA and RHO type zeolites without organic structure directing agents provided materials with a Si/Al ratio suitable for the separation of CO_2 from CH_4. The first part of this study concerns the development of a new synthetic route towards preparation of small pore nanozeolites from water clear precursor suspensions. The nanocrystals have a diameter of 30 - 200 nm and a Si/Al ratio of 1.4 to 2.6. The second part is dedicated on the crystallographic analysis of the RHO and CHA nanosized zeolites in hydrated and dehydrated forms. Precession electron diffraction tomography (PEDT) and in-situ powder XRD methods were used to characterize the structure of the newly synthesized materials with nanosized dimensions. The third part of the thesis includes the adsorption studies of CO_2 and CH_4 in the CHA and RHO nanosized zeolites. The high selectivity of the zeolite nanocrystals synthesized with different cations (Cs, Na, K) towards CO_2 in the presence of CH_4 is demonstrated.